Flood, R.D., Piper, D.J.W., Klaus, A., et al., 1995
*Proceedings of the Ocean Drilling Program, Initial Reports,* Vol. 155

# 12. SITE 936[1]

Shipboard Scientific Party[2]

## HOLE 936A

**Date occupied:** 22 April 1994

**Date departed:** 27 April 1994

**Time on hole:** 4 days, 11 hr, 30 min

**Position:** 5°37.936′N, 47°44.134′W

**Bottom felt (drill pipe measurement from rig floor, m):** 3586.0

**Distance between rig floor and sea level (m):** 11.05

**Water depth (drill pipe measurement from sea level, m):** 3575.0

**Penetration (m):** 433.80

**Number of cores (including cores having no recovery):** 46

**Total length of cored section (m):** 433.80

**Total core recovered (m):** 274.42

**Core recovery (%):** 63

**Oldest sediment cored:**
Depth (mbsf): 433.80
Nature: Silty clay
Earliest age: Pleistocene

**Principal results:** Site 936 (near proposed Site AF-1) is located on the western levee of Amazon Channel. It was one of a series of sites designed to characterize the development of the most recently active channel-levee system. It also was planned to sample and date Unit R, the Middle Levee Complex, and the Gold levee of the Lower Levee Complex. The site was moved about 3 km east of proposed Site AF-1 and positioned over the flank of the Gold levee to avoid the levee crest, which may have been eroded. The revised site was selected from a *Conrad* seismic profile (C2514; 1132UTC on 3 Dec. 1984).

Hole 936A was cored by APC to 92.0 mbsf, then by XCB to 433.8 mbsf, with total hole recovery of 274.42 m (63.3%). Temperature measurements were made at 51 and 73 mbsf (ADARA) and at 135 mbsf (WSTP), yielding a geothermal gradient of 29°C/km. There was gas expansion in many cores. Methane was found throughout the hole, with highest concentrations at the base of the hole; no higher molecular-weight hydrocarbons were detected. The Quad-combo, FMS, and geochemical logging tools were run at this site, but hole conditions prevented logging below 310 mbsf.

Six lithologic units are recognized:

Unit I (0–0.96 mbsf) is an intensely bioturbated Holocene nannofossil-foraminifer clay, with about 42% carbonate at the top of the unit decreasing to 6% near the base. One rust-colored diagenetic crust is present at 0.46 mbsf.

Unit II (0.96–72.10 mbsf) consists of mud with interbedded laminae and beds of silt and very fine sand. Carbonate content is uniformly low (1.2%–2.3%). The unit is correlated with the levee flanks of the Amazon-Brown Channel-levee System. Subunit IIA (0.96–6.97 mbsf) comprises intensely bioturbated mud. Subunit IIB (6.97–72.10 mbsf) consists of mud with thin beds of silt and fine sand. Although the unit shows an overall fining-upward trend, several intervals with abundant laminae and thin beds of silt and sand alternate with 1- to 3-m-thick intervals of moderately bioturbated mud with few silt laminae. A small slump occurs at 56 mbsf. Silt beds in Unit II have a higher mica content than those deeper in the hole.

Unit III (72.10–154.50 mbsf) corresponds to an interval of poor core recovery (33.6%) that is correlated with a high-amplitude reflection packet (HARP) in the seismic reflection profile. Subunit IIIA (72.1 to 106.30 mbsf) recovered medium to coarse sand, some in graded beds and others in massive beds with mud clasts. Some interbedded mud is also present. One pebble of siltstone was recovered. Log data suggest that the subunit corresponds to a sequence of sand beds, with the base at 100 mbsf. This subunit correlates to the Brown HARP interval. Subunit IIIB (106.30–117.00 mbsf), corresponding to the flank of the Aqua levee, consists of color-banded mud with laminae and thin beds of silt and sand. The top of the subunit is bioturbated. Subunit IIIC (117.00–154.50 mbsf) recovered mud with silt laminae and a few 15- to 25-cm-thick fine sand beds. Log data suggest a sequence of sand beds, typically 1–2 m thick and possibly thickening and coarsening upward, from the base of the subunit to about 122 mbsf. The sand sequence is capped by muddier sediment that forms the base of a fining-upward sequence continuing into Subunit IIIB. The sandy interval of Subunit IIIC correlates with the HARP intervals associated with the Aqua and earlier systems.

Unit IV (154.50–294.16 mbsf) consists of dark gray mud, much of which appears deformed. The unit is correlated with the seismically defined "Unit R" and is similar to Unit IV at Site 935. The top 15 m of the unit contains various mud clasts, wood, shell fragments, and fine pebbles (0.5 cm). One clast contains Miocene nannofossils. Between 190 and 260 mbsf, natural gamma logs show six cycles with a gradual downward decrease in counts, followed by an abrupt increase at the top of the next cycle. In the upper part of the unit, at least three 10- to 15-m-thick intervals show a gradual upward decrease in water content (ranging from 22% to 30%) and resistivity (lab and log data), interpreted as resulting either from pore-water escape of successive debris flows or from cyclic variation in grain size (as suggested by the natural gamma log). Below 225 mbsf, sediment strength is much higher, water content is more uniform at 19%–23%, and resistivity anisotropy shows a large scatter. This part of the unit consists principally of uniform dark mud, but also contains rare deformed sand beds, mud clasts of various shades of gray, and rare rock granules. An anomalously low concentration of pore-water chloride (547 mM) was found at 267 mbsf.

Unit V (294.16–405.69 mbsf) is correlated seismically with the Red Channel-levee System (Middle Levee Complex). Subunit VA (294.16–307.35 mbsf) consists of mud with laminae and thin beds of silt and fine sand. Some sand beds are up to 25 cm thick. Log data suggest that the subunit forms a fining-upward sequence. Logging also shows that this subunit has low resistivity, which may be related to undercompaction immediately beneath the mass-transport unit, as was observed at Sites 931, 933, and 935. Subunit VB (307.35–377.40 mbsf) corresponds to an interval of poor core recovery (4.5%) of fine- and medium-grained sand. This part of the

[1]Flood, R.D., Piper, D.J.W., Klaus, A., et al., 1995. *Proc. ODP, Init. Repts.,* 155: College Station, TX (Ocean Drilling Program).

[2]Shipboard Scientific Party is as given in the list of participants in the contents.

hole was severely washed out and only the top could be logged: these data suggest a predominance of sand. Seismic profiles of the Red system here also suggest that the flank of the levee is more reflective (?coarser) than other levee units. Subunit VC (377.40–387.52) consists of mud with laminae and thin beds of silt and fine sand, interpreted as distal levee deposits. The base of the subunit is color banded, with 11% carbonate, and contains a microfossil assemblage of calcareous nannofossils, interglacial planktonic foraminifers, and abyssal benthic foraminifers. It is possible that this lithology is a clast in the underlying debris-flow deposit. Subunit VD (387.52–405.69 mbsf) is mud-clast conglomerate interpreted as debris-flow deposits. It contains some carbonate-rich clasts (22%–32% carbonate) with microfossils similar to those in the base of Subunit VC.

Unit VI (405.69–433.80 mbsf) corresponds to the top of the Gold levee of the Lower Levee Complex. Subunit VIA (405.69–415.35 mbsf) comprises moderately bioturbated carbonate-bearing clay (at least 7% carbonate), with a high total sulfur content, similar to that seen in Holocene Unit I, and a rich microfossil assemblage similar to Subunit VC. The subunit passes gradually downcore into Subunit VIB (415.35–433.8 mbsf), comprising mud with laminae and thin beds of silt and rare fine sand.

In general, organic-carbon content decreases from 1.2% near the top of the hole to 0.8% near the base. As at Site 935, bitumen analyses from glacial-age sediment showed *n*-alkanes with mainly odd numbers of carbon atoms and *n*-$C_{29}H_{60}$ as the major *n*-alkane. One analysis of Holocene sediment showed a noticeably lower predominance of odd-numbered alkanes.

Oscillations in paleomagnetic declination, inclination, and/or intensity, interpreted as secular-variation cycles, occur at 7–15, 26–30, and 64–66 mbsf.

Microfossil assemblages are similar to those at Site 935. The base of the Holocene is at about 1 mbsf. The 40-ka *P. obliquiloculata* datum cannot be identified because of barren intervals in the core. The first downcore reappearance of *P. obliquiloculata* at 150 mbsf is associated with a CN15b nannofossil assemblage, placing its age between 40 and 85 ka. Subunit VC, beneath turbidites of the Middle Levee Complex, has an interglacial foraminifer assemblage and CN15a Zone nannofossils. As at Site 935, bioturbated sediment (Subunit VIA) at the top of the Lower Levee Complex has a warm-interglacial microfossil assemblage, nannofossils from Zone CN14b, and foraminifers including high proportions of *G. tumida flexuosa* and *G. hexagonus*. As in the Holocene section, pollen is rare. This site confirmed the observation at Site 935 that interglacial sediment directly overlies the Lower Levee Complex, implying an overall sea-level control of the growth of major channel-levee complexes.

## SETTING AND OBJECTIVES

### Introduction

Site 936 (proposed Site AF-1) was one of a series of sites designed to characterize the development of the most recently active channel of the Amazon Fan (the Amazon Channel). It is also the deepest hole planned for Leg 155, penetrating high-amplitude reflection packets (HARPs) beneath the Brown/Amazon Channel, the Unit R Debris Flow, the Middle Levee Complex, and terminating in the Gold levee of the Lower Levee Complex (nomenclature from Manley and Flood, 1988).

### Setting

Site 936 is located on the western (left) levee of the Amazon Channel, about 3 km from the channel axis (Fig. 1). The site was moved about 3 km east of proposed Site AF-1 to avoid a deep levee crest and to meet some of the shallower objectives of proposed Site AF-2. The revised site was selected from a *Conrad* seismic profile (C2514; 1137UTC on 3 Dec. 1984). We located Site 936 at a similar position on our *JOIDES Resolution* profile (1623UTC on 22 April 1994; Fig. 2).

Site 936 is up-fan from the Amazon-Brown avulsion point, so the shallow levee sequence represents deposition during the time that the Brown and Amazon channels were active. Site 936 is also down-fan from the Brown-Aqua avulsion point, so this channel formed as the Aqua Channel, sampled at Site 935, was being abandoned. A 3.5-kHz profile at the site (Fig. 3) shows that Site 936 is located on a portion of the levee where sediment waves are not well developed. Sediment waves are observed starting about 1 km west of Site 936. The upper 45 ms of the levee at Site 936 is acoustically layered. Some smaller-scale topography is indicated by lateral changes in layer reflection strength. The seismic-reflection data show that the levee-crest strata

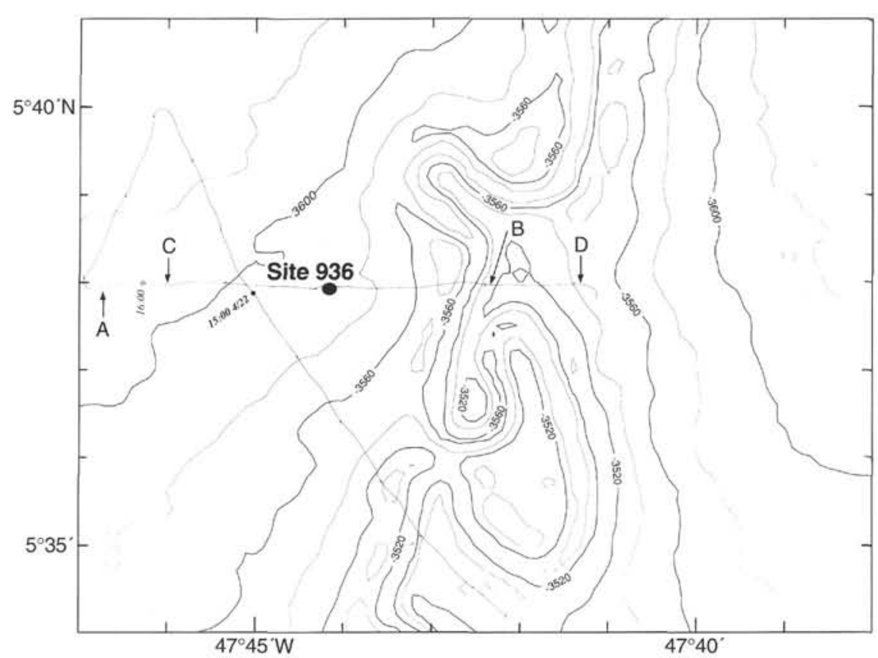


Figure 1. Location of Site 936 showing *JOIDES Resolution* tracks. Bathymetry from Flood et al. (1991). A–B is seismic profile in Figure 2. C–D is 3.5-kHz profile in Figure 3.

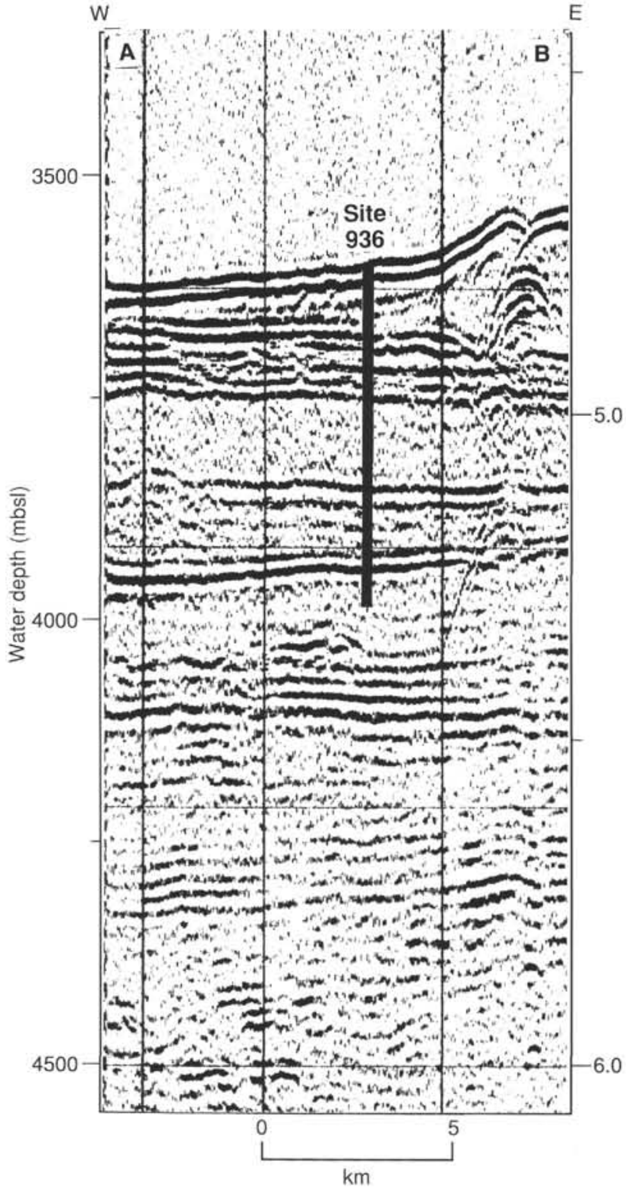


Figure 2. Seismic section through Site 936. (*JOIDES Resolution* profile, 1555–1640 UTC on 22 April 1994).

associated with the Amazon/Brown System are about 70 ms (53 m) thick (Figs. 2 and 3). They overlie one or more HARP units, 100 ms thick (80 m), that may represent sandier deposits formed in the early stages of channel avulsion. The HARP units overlie a 140-ms-thick (117 m) acoustically incoherent unit with surface hyperbolic diffractions (interpreted as a debris-flow deposit). The interpreted debris-flow deposit overlies a possible 60-ms-thick (53 m) turbidite unit overlying the levee flank of the Red Channel-levee System. The Red Channel-levee System is part of the Middle Levee Complex (Manley and Flood, 1988). The 60-ms-thick (56 m) Red levee overlies the flank of the Gold levee, part of the Lower Levee Complex. We planned to penetrate a few tens of meters into the Gold levee.

## Objectives

The principal objectives at Site 936 were to:

1. Sample the combined Brown and Amazon levee deposits upslope from the Amazon-Brown avulsion point and characterize facies in the levee flank that should be correlative to levee deposits sampled at Site 940 (AF-6) upslope.
2. Sample the multiple HARP units that underlie the Amazon Channel.
3. Characterize the downslope evolution of Unit R.
4. Obtain a deep biostratigraphic section through the Middle and much of the Lower Levee Complex.

The logging objectives were to characterize the HARP, levee, and debris-flow acoustic facies by their log response, particularly to establish thickness and patterns of sand beds that are poorly recovered by coring. A secondary objective was to geochemically characterize sediment variability in the turbidite and bioturbated intervals.

## OPERATIONS

### Transit: Site 935 to Site 936 (Relocated AF-1)

The transit from Site 935 to Site 936 covered 12 nmi in about 1.1 hr. We conducted a 16-nmi seismic survey over Site 936 in 2.8 hr at about 5.8 kt. We returned to 5°39.941′N, 47°44.131′W and deployed a beacon at 1401 hr 22 April. A BHA similar to that used at Site 935 was assembled and run to the seafloor.

### Hole 936A

We positioned the bit at 3583.0 mbrf and spudded Hole 936A at 2050 hr 22 April. The distance from sea level to rig floor, which depends on the ship's draft, was approximately 11.05 m for Hole 936A. Core 1H recovered 6.54 m, and the mud line was defined to be at 3586.0 mbrf (Table 1). Cores 1H through 10H were taken from 3586.0 to 3678.0 mbrf (0–92.0 mbsf) recovering 88.52 m (96.2%). Cores 3H through 10H were oriented using the Tensor tool. ADARA heat-flow measurements were taken during Cores 6H and 8H. The core barrel only partially stroked while taking Cores 9H and 10H (Core 10H was in sand with 90,000-lb overpull).

XCB Cores 11X through 46X were taken from 3678.0 to 4019.8 mbrf (92.0–433.8 mbsf), coring 341.8 m and recovering 185.51 m (54.3% recovery). A WSTP temperature measurement was taken at 3711.5 mbrf (135.2 mbsf).

The formation from 308 to 376 mbsf was unstable, and the hole fill increased to 12 m with very heavy flow back while adding new stands of drill pipe. Numerous mud sweeps were required to keep the hole moderately clean, although hole conditions remained good. The combined APC/XCB recovery was 63.1%. The hole angle was 1.75° at 70.0 mbsf and 1.4° at 89.0 mbsf. Core disturbance due to gas expansion was minimized by drilling small holes in nearly all of the core liners. Parts of Cores 6H, 7H, 8H, 16X, 24X, 27X, 43X, 45X, and 46X were disturbed due to gas-induced extrusion of core from the liner or collapsed liners.

The hole was circulated clean with two sweeps of sepiolite mud (20 and 30 barrels), and we pulled the pipe up to 65 mbsf with 10,000-lb overpull. While running the pipe back to the bottom of the hole (TD), we had to ream out a 7-m bridge at 382 mbsf (52 m above the bottom of the hole) and encountered 25 m of soft fill. We circulated 35 barrels of sepiolite mud, pumped the go-devil to open the lockable flapper valve (to enable logging), and pulled the pipe back up to 3669.5 mbrf (83.5 mbsf) for logging. At the end of each logging run, we pulled the bit up to 65 mbsf to log the upper part of the hole. However, each time we did this the soft sediment formed a bridge at the end of the pipe that hindered passage of the logging tools. Logs were run as follows: (1) the Quad-combo tool was run to 3915 mbrf (329 mbsf) in 4.6 hr; (2) the FMS tool was run to 3894 mbrf (308 mbsf) in 4.3 hr; and (3) the geochemical log was run to 3680 mbrf (94 mbsf) in 7.4 hr. We pulled the bit above the seafloor at 1925 hr 26 April. The bit cleared the rig floor at 0135 hr 27 April, and the beacon was recovered.

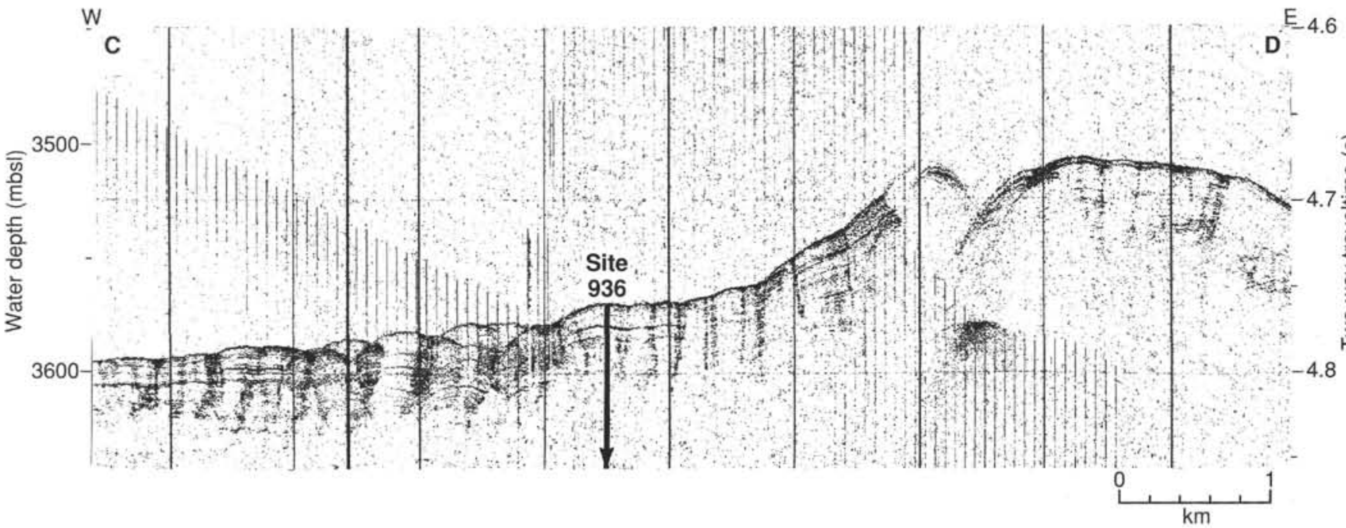


Figure 3. *JOIDES Resolution* 3.5-kHz profile through Site 936.

**Table 1. Site 936 coring summary.**

| Core | Date (1994) | Time (UTC) | Depth (mbsf) | Length cored (m) | Length recovered (m) | Recovery (%) |
|---|---|---|---|---|---|---|
| 155-936A- | | | | | | |
| 1H | April 23 | 0110 | 0.0–6.5 | 6.5 | 6.54 | 100.0 |
| 2H | April 23 | 0200 | 6.5–16.0 | 9.5 | 9.89 | 104.0 |
| 3H | April 23 | 0250 | 16.0–25.5 | 9.5 | 10.36 | 109.0 |
| 4H | April 23 | 0340 | 25.5–35.0 | 9.5 | 10.37 | 109.1 |
| 5H | April 23 | 0445 | 35.0–44.5 | 9.5 | 10.39 | 109.3 |
| 6H | April 23 | 0605 | 44.5–54.0 | 9.5 | 10.39 | 109.3 |
| 7H | April 23 | 0705 | 54.0–63.5 | 9.5 | 9.52 | 100.0 |
| 8H | April 23 | 0840 | 63.5–73.0 | 9.5 | 10.12 | 106.5 |
| 9H | April 23 | 0940 | 73.0–82.5 | 9.5 | 2.37 | 24.9 |
| 10H | April 23 | 1045 | 82.5–92.0 | 9.5 | 8.57 | 90.2 |
| 11X | April 23 | 1250 | 92.0–96.7 | 4.7 | 1.26 | 26.8 |
| 12X | April 23 | 1400 | 96.7–106.3 | 9.6 | 0.03 | 0.3 |
| 13X | April 23 | 1515 | 106.3–115.9 | 9.6 | 6.01 | 62.6 |
| 14X | April 23 | 1620 | 115.9–125.5 | 9.6 | 1.61 | 16.8 |
| 15X | April 23 | 1725 | 125.5–135.2 | 9.7 | 0.42 | 4.3 |
| 16X | April 23 | 1945 | 135.2–144.8 | 9.6 | 0.70 | 7.3 |
| 17X | April 23 | 2045 | 144.8–154.5 | 9.7 | 6.10 | 62.9 |
| 18X | April 23 | 2205 | 154.5–164.1 | 9.6 | 9.53 | 99.3 |
| 19X | April 23 | 2320 | 164.1–173.8 | 9.7 | 8.25 | 85.0 |
| 20X | April 24 | 0005 | 173.8–183.4 | 9.6 | 7.75 | 80.7 |
| 21X | April 24 | 0135 | 183.4–193.1 | 9.7 | 7.90 | 81.4 |
| 22X | April 24 | 0250 | 193.1–202.8 | 9.7 | 6.69 | 68.9 |
| 23X | April 24 | 0405 | 202.8–212.5 | 9.7 | 7.35 | 75.8 |
| 24X | April 24 | 0545 | 212.5–222.1 | 9.6 | 8.27 | 86.1 |
| 25X | April 24 | 0710 | 222.1–231.7 | 9.6 | 7.68 | 80.0 |
| 26X | April 24 | 0840 | 231.7–241.4 | 9.7 | 9.82 | 101.0 |
| 27X | April 24 | 1005 | 241.4–251.1 | 9.7 | 10.19 | 105.0 |
| 28X | April 24 | 1215 | 251.1–260.7 | 9.6 | 8.50 | 88.5 |
| 29X | April 24 | 1410 | 260.7–270.4 | 9.7 | 7.77 | 80.1 |
| 30X | April 24 | 1605 | 270.4–279.9 | 9.5 | 8.72 | 91.8 |
| 31X | April 24 | 1805 | 279.9–289.4 | 9.5 | 6.83 | 71.9 |
| 32X | April 24 | 2010 | 289.4–299.0 | 9.6 | 9.72 | 101.0 |
| 33X | April 24 | 2145 | 299.0–308.6 | 9.6 | 8.65 | 90.1 |
| 34X | April 24 | 2300 | 308.6–318.2 | 9.6 | 0.00 | 0.0 |
| 35X | April 25 | 0025 | 318.2–327.9 | 9.7 | 1.53 | 15.8 |
| 36X | April 25 | 0150 | 327.9–337.5 | 9.6 | 0.03 | 0.3 |
| 37X | April 25 | 0330 | 337.5–347.2 | 9.7 | 0.00 | 0.0 |
| 38X | April 25 | 0530 | 347.2–356.8 | 9.6 | 0.01 | 0.1 |
| 39X | April 25 | 0700 | 356.8–366.4 | 9.6 | 1.03 | 10.7 |
| 40X | April 25 | 0910 | 366.4–376.0 | 9.6 | 0.00 | 0.0 |
| 41X | April 25 | 1115 | 376.0–385.7 | 9.7 | 6.19 | 63.8 |
| 42X | April 25 | 1355 | 385.7–395.3 | 9.6 | 3.10 | 32.3 |
| 43X | April 25 | 1630 | 395.3–405.0 | 9.7 | 10.19 | 105.0 |
| 44X | April 25 | 1830 | 405.0–414.6 | 9.6 | 3.68 | 38.3 |
| 45X | April 25 | 2010 | 414.6–424.2 | 9.6 | 8.36 | 87.1 |
| 46X | April 25 | 2230 | 424.2–433.8 | 9.6 | 2.00 | 20.8 |
| Coring totals | | | | 433.8 | 274.4 | 63.30 |

Note: An expanded version of this coring summary table that includes lengths and depths of sections, location of whole-round samples, and comments on sampling disturbance is included on the CD-ROM in the back pocket of this volume.

# LITHOSTRATIGRAPHY

## Introduction

A total of 433.80 m was cored in one hole at Site 936 with an overall recovery of 63.3% (Fig. 4). Recovery was especially poor from 95 to 145 mbsf (Cores 936A-11X through -16X) and 310 to 375 mbsf (Cores 936-34X through -40X). Gas was present throughout much of the sediment, and gas expansion and escape disrupted the sedimentary structures of a large proportion of the thicker silt and sand beds. In addition, drilling disturbance formed drilling "biscuits" in some of the XCB cores, causing deformation and rotation of beds (see "Lithostratigraphy" section in "Explanatory Notes" chapter, this volume). The coring disturbance tends to accentuate zones of disturbed bedding produced by syn- and post-depositional processes (e.g., slumps, debris flows, etc.); however, this can complicate distinguishing in-situ structures from drilling disturbance. The sedimentary section is divided into six major lithologic units: Units I to VI. Units II, III, V, and VI are further subdivided into subunits (Figs. 4 and 5).

## Description of Lithostratigraphic Units

### *Unit I*

Interval: 155-936A-1H-1, 0–96 cm
Age: Holocene
Depth: 0.00 to 0.96 mbsf

Unit I consists of brown calcareous clay (10YR 5/3) with abundant foraminifers and nannofossils. The sediment is moderately bioturbated and slightly color mottled. The carbonate content is 42% at 0.27 mbsf in the upper part of the unit, but sharply decreases downward to ~6% at 0.75 mbsf (see "Organic Geochemistry" section, this chapter). This unit contains a distinctive rust-colored (dark reddish brown, 5YR 4/3) crust (interval 936A-1H-1, 46–47 cm; 0.46–0.47 mbsf). This diagenetic, iron-rich crust was analyzed previously and correlated throughout the Amazon Fan and adjacent Guiana Basin (e.g., Damuth, 1977; see "Introduction" chapter, this volume). Below this crust, Unit I is marked by a gradational color change to dark grayish brown (2.5Y 4/2) at the top of Subunit IIA. The character of Unit I is similar to that of the uppermost sediment at most of the other drill sites.

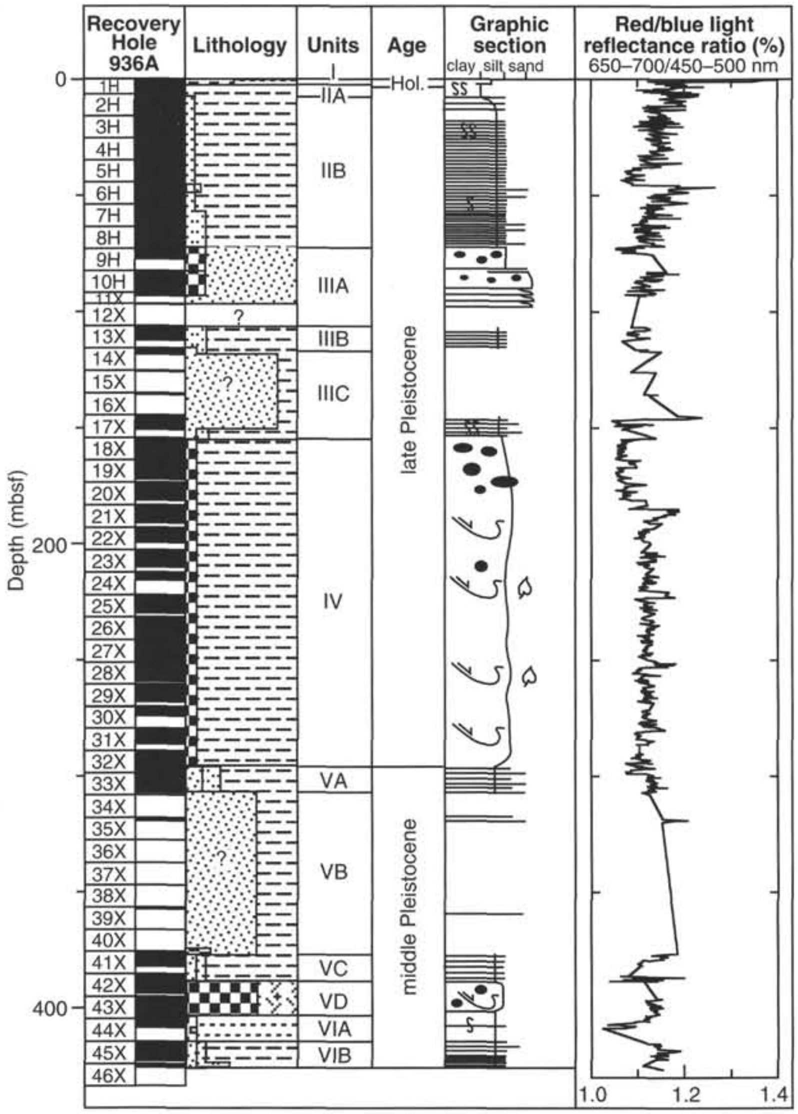


Figure 4. Composite stratigraphic section for Site 936 showing core recovery, a simplified summary of lithology, depth of unit boundaries, age, a graphic section with generalized grain-size and bedding characteristics, and downhole variations in the light-reflectance values. The lithologic symbols are explained in Figure 1 of the "Explanatory Notes" chapter, this volume.

### *Unit II*

Interval: 155-936A-1H-1, 96 cm, through -8H-6, 110 cm
Age: Holocene to late Pleistocene
Depth: 0.96 to 72.10 mbsf

Unit II consists mainly of terrigenous dark olive gray (5Y 3/2) to very dark gray (5Y 3/1) silty clay. Most of the sediment in this unit is stained to varying degrees by diagenetic hydrotroilite, which imparts an ephemeral black color to the sediment as irregular patches and/or color bands and laminae (see "Introduction" chapter, this volume). Grains of silt and fine sand in laminae and beds, as well as in burrow fills, are also commonly stained black. The carbonate content is uniformly low (1.2%–2.3%) throughout the unit. Unit II can be subdivided into two subunits based on the occurrence of silt and sand laminae and beds.

#### *Subunit IIA*

Subunit IIA extends from 936A-1H-1, 96 cm (0.96 mbsf), through -2H-1, 47 cm (6.97 mbsf), and consists predominantly of dark olive gray clay (5Y 3/2) at the top that grades down to silty clay by 5 mbsf (Fig. 5). Black color mottling is extensive near the top, then decreases downhole. In contrast, black color banding is rare to absent in this subunit. Bioturbation is extensive to moderate.

#### *Subunit IIB*

Subunit IIB extends from 6.97 to 72.1 mbsf (interval 936A-2H-1, 47 cm, through -8H-6, 110 cm). The sediment of this subunit consists of dark gray silty clay (5Y 4/1) at the top grading downhole into very dark gray (5Y 3/1) and dark olive gray (5Y 3/2) silty clay. This subunit is characterized by the occurrence of numerous discrete laminae and beds of silt and, below 41 mbsf, by beds of silt to fine sand in some intervals (Figs. 5 and 6). Many of the clay intervals between silt and sand laminae and beds show black, hydrotroilite-rich, horizontal color bands or laminae, whereas other intervals show black irregular mottling. Some of the mottled zones appear to be moderately to extensively bioturbated. The boundary between Subunits IIA and IIB is placed at the shallowest occurrence of silt laminae (6.47 mbsf; Figs. 4 and 5).

The numerous laminae and beds of silt and fine sand generally increase in frequency and thickness downhole (Figs. 5 and 6). Silt laminae increase from a minimum of three per meter in Core 936A-3H to approximately 23 per meter in Core 936A-8H. Beds of silt and fine sand range from a minimum of 0.5 per meter in Core 936A-3H to seven per meter in Core 936A-6H. The total number of laminae and beds of silt and fine sand increases from 2.7 per meter in Core 936A-3H to 25.8 per meter in Core 936A-8H. Silt laminae are commonly <1–5 mm thick with most less than 3 mm thick. Beds of silt and fine sand

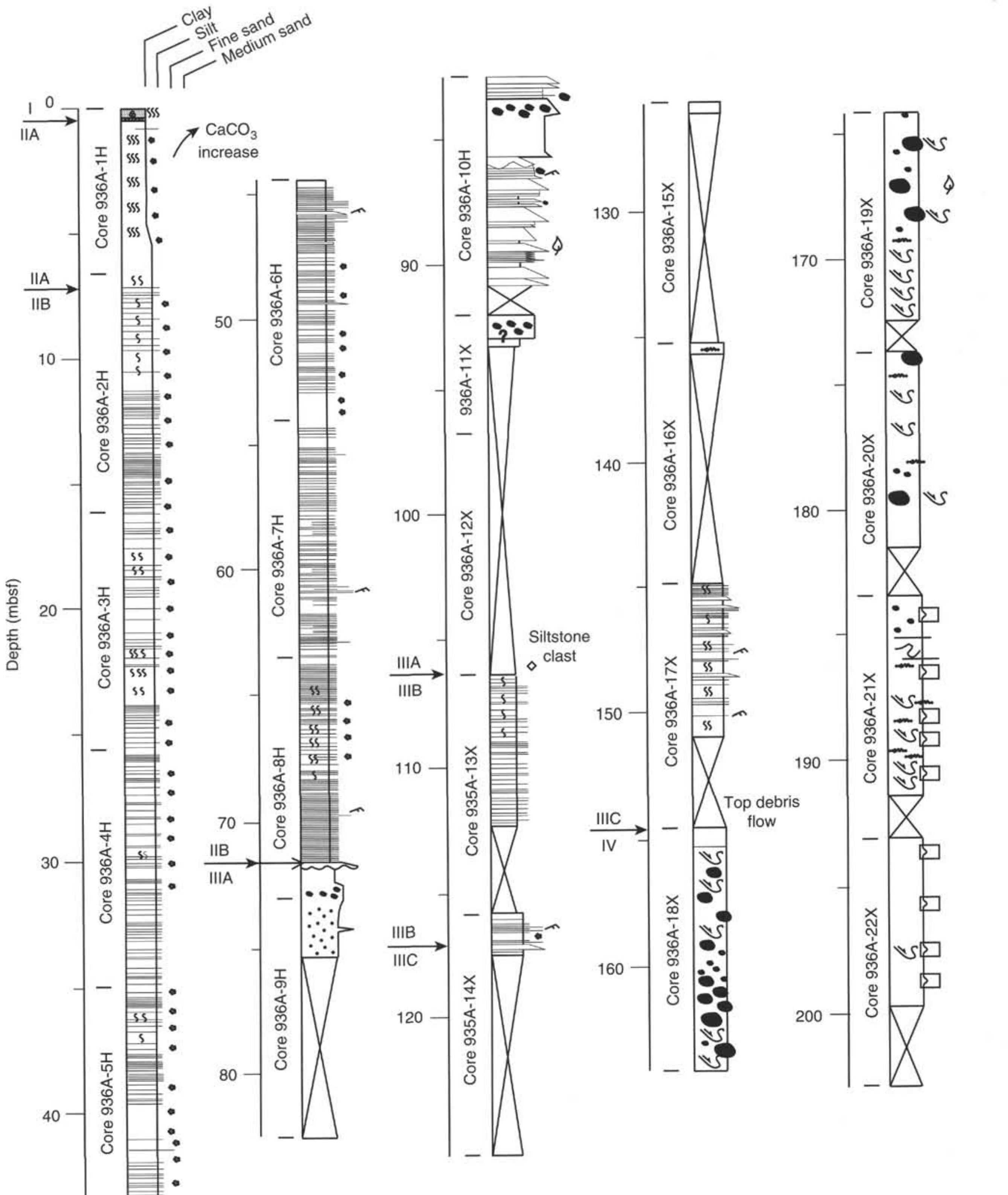


Figure 5. Graphic sedimentological columns for Site 936 showing grain-size variation (width of columns), bed thickness, and sedimentary structures; symbols and preparation of these columns are explained in the "Lithostratigraphy" section of the "Explanatory Notes" chapter, this volume. Arrows indicate the positions of unit and subunit boundaries. The upper part of the column is shown in strike section of the foldout (back pocket, this volume) for comparison of levee sequences on the middle and upper fan, and in the longitudinal profile of the foldout to show the down-fan changes in levee deposits.

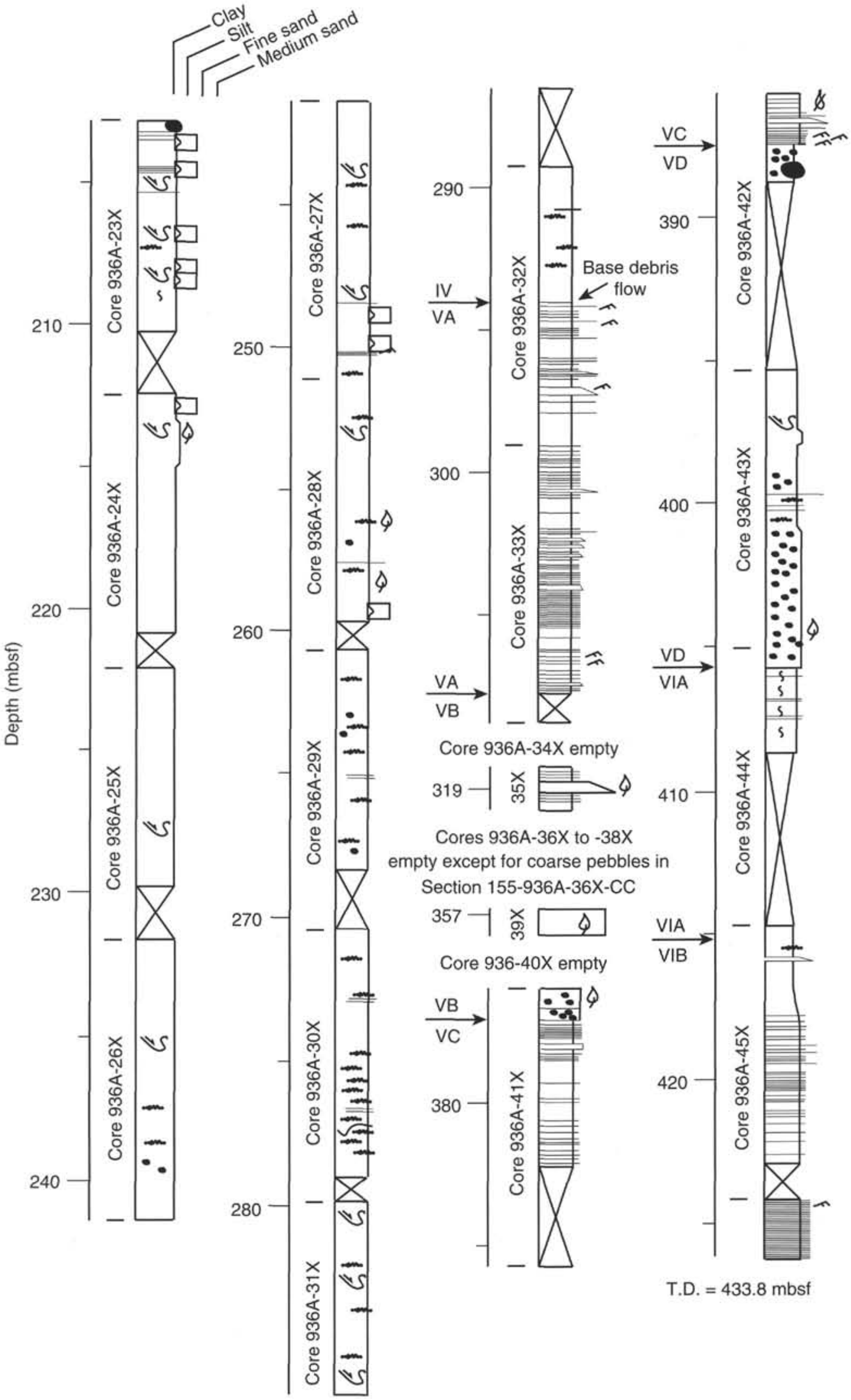


Figure 5 (continued).

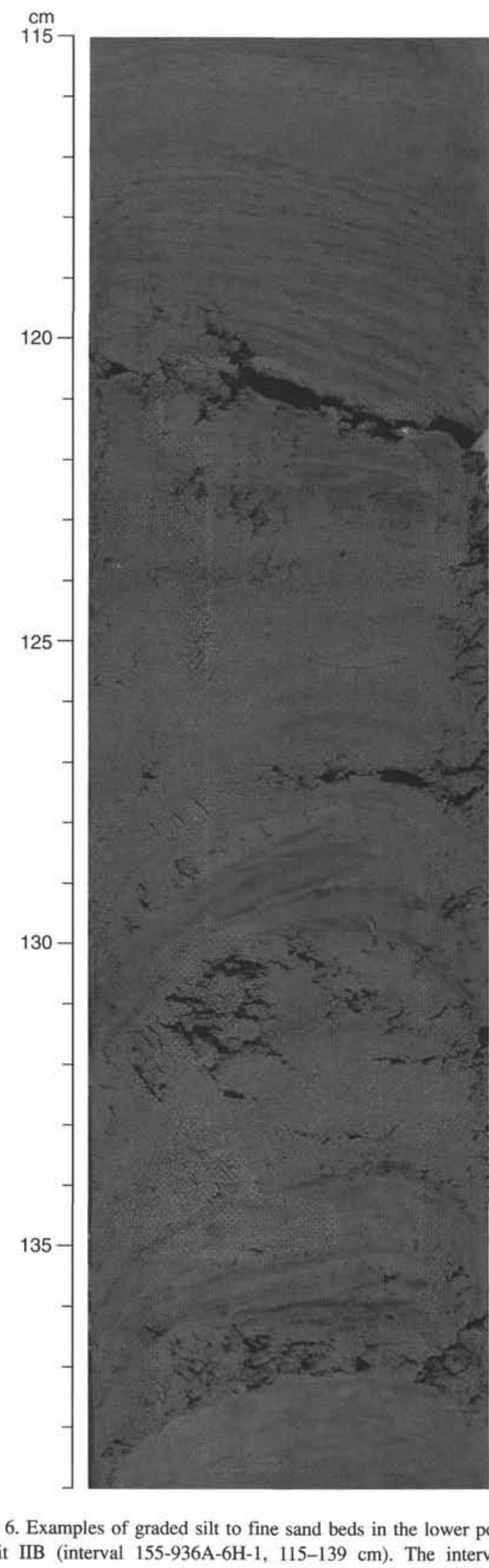


Figure 6. Examples of graded silt to fine sand beds in the lower portion of Subunit IIB (interval 155-936A-6H-1, 115–139 cm). The interval from approximately 116 cm to 127.5 cm is a graded bed that grades upward from fine sand through silt, then interbedded clay and silt laminae to clay. This and other coarse beds in this subunit have sharp bases and gradational tops. Beds are partially disturbed by coring.

average 1–3 cm in thickness with a maximum thickness of 10 cm (Fig. 6).

Although gas expansion appears to have disrupted the primary structures of many silt and fine sand beds, many beds do exhibit parallel lamination, and less commonly, cross-lamination (Fig. 6). Many of the silt and fine sand beds, as well as some of the silt laminae, appear normally graded with sharp, irregular bases and gradational tops. Some grade upward from fine sand through silt into alternating laminae (~1 mm thick) of silt and mud, and finally into mud (Fig. 6). A thin interval of disturbed sedimentary structures occurs in Subunit IIB (interval 936A-7H-2, 33–112 cm (55.83–56.62 mbsf)). In this interval, the laminae and beds of silt and fine sand dip at various steep angles and suggest sediment failure by slumping or related processes. Subunit IIB apparently represents a fining- and thinning-upward sequence of turbidites deposited on a channel levee. The absence of silt laminae in overlying Subunit IIA suggests that overbank deposition stopped and hemipelagic deposition ensued.

### *Unit III*

Interval: 155-936A-8H-6, 110 cm, through -18X-1, 0 cm
Age: late Pleistocene
Depth: 72.10 to 154.50 mbsf

In contrast to Unit II, Unit III consists of predominantly thick, coarse-grained deposits of variable lithology and depositional origin. Core recovery was poor throughout the unit (36% overall; Fig. 4), probably because of the thick coarse-grained beds encountered. Thus, wireline logs were used to help constrain the three subunit boundaries. The carbonate content is uniformly low (0% to 3.2%) throughout the unit.

#### *Subunit IIIA*

Subunit IIIA extends from 72.10 to 106.30 mbsf (intervals 936A-8H-6, 110 cm, through -13X-1, 0 cm) and consists of interbeds of black sandy clay; thin to thick, normally graded sand beds; and thick beds of sand and muddy sand with rare to abundant mud clasts. The top of the subunit is marked by a 24-cm-thick normally graded bed of fine sand to silty clay with an irregular, dipping basal contact (interval 936A-8H-6, 110–134 cm). The sand contains a zone of black (N2) organic detritus. This graded bed overlies a bed of silty, sandy, black (N2) clay (interval 936A-8H-6, 134 cm, through -8H-7, 40 cm). This bed is underlain by a bed of dark gray (5Y 3/1) fine sand of variegated shades, which contains mud clasts of various sizes and shapes (interval 936A-8H-7, 40 cm, through -8H-CC, 17 cm).

Interval 936A-9H-1, 0 cm, to -2, 87 cm, consists of black (5Y 2.5/1) massive sandy mud. Coarse granules and pebbles of quartz and rock fragments up to 1 cm in diameter, plus wood fragments, are scattered throughout this deposit (Fig. 7). Interval 936A-10H-1, 0–57 cm, contains two normally graded beds of medium to very coarse sand with irregular, dipping basal contacts (Fig. 8). Interval 936A-10H-1, 57–150 cm, is composed of one or more beds of poorly sorted, medium to coarse sand with mud clasts of various shapes (angular to rounded), sizes (up to 10 cm diameter), and orientations (Fig. 9). Some zones of sand in this interval show slight normal grading, which, together with various angular contacts, suggest that this interval may be a series of separate deposits.

The remainder of this core (interval 936A-10H-2, 0 cm, through -6, 97 cm) consists mainly of a series of sand beds that are composed of fine to medium, and rarely coarse, sand, and that are commonly graded. Minor beds of fine to medium sand with mud clasts of various shapes, sizes, and orientations are interbedded with these sand beds. Organic detritus is abundant in some zones and includes wood fragments up to 1 cm long. Individual bed contacts and thicknesses commonly cannot be determined with certainty because of core disturbance; however, many beds are tens of centimeters thick and have irregular, dipping contacts. Core 936A-11X also consists entirely of

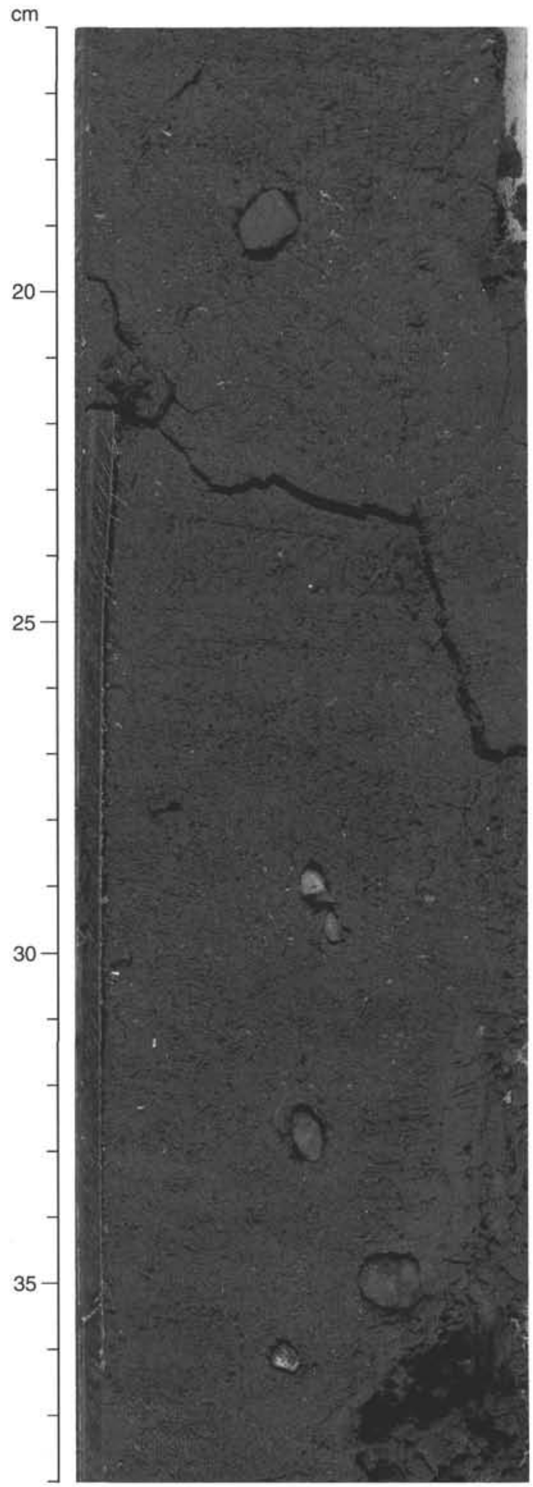


Figure 7. Quartz and rock granules and pebbles scattered through black sandy mud of Subunit IIIA (interval 155-936A-9H-2, 16–38 cm). This bed is interpreted as a debris-flow deposit.

deformed fine sand with mud clasts of various sizes and shapes. Core 936A-12X had no recovery except for a dark gray-brown (2.5Y 4/2) siltstone pebble (3 × 2 × 1 cm).

The sediment of Subunit IIIA plus the wireline logs from this interval (see "Downhole Logging" section, this chapter) indicate that this subunit consists of a series of thick beds of sand and gravel. The

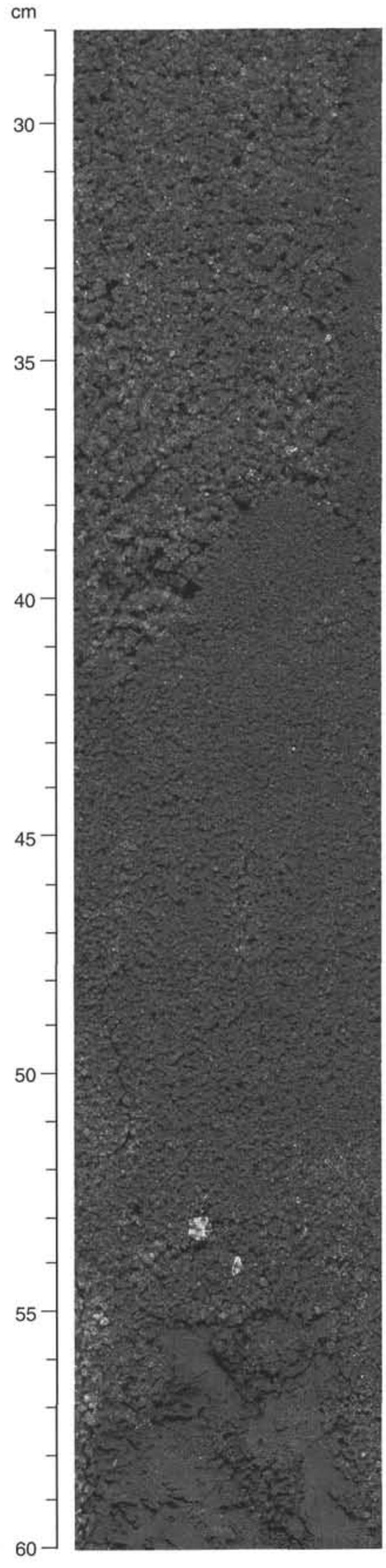


Figure 8. Normally graded medium to very coarse sand beds with very irregular bases from Subunit IIIA (interval 155-936A-10H-1, 28–60 cm).

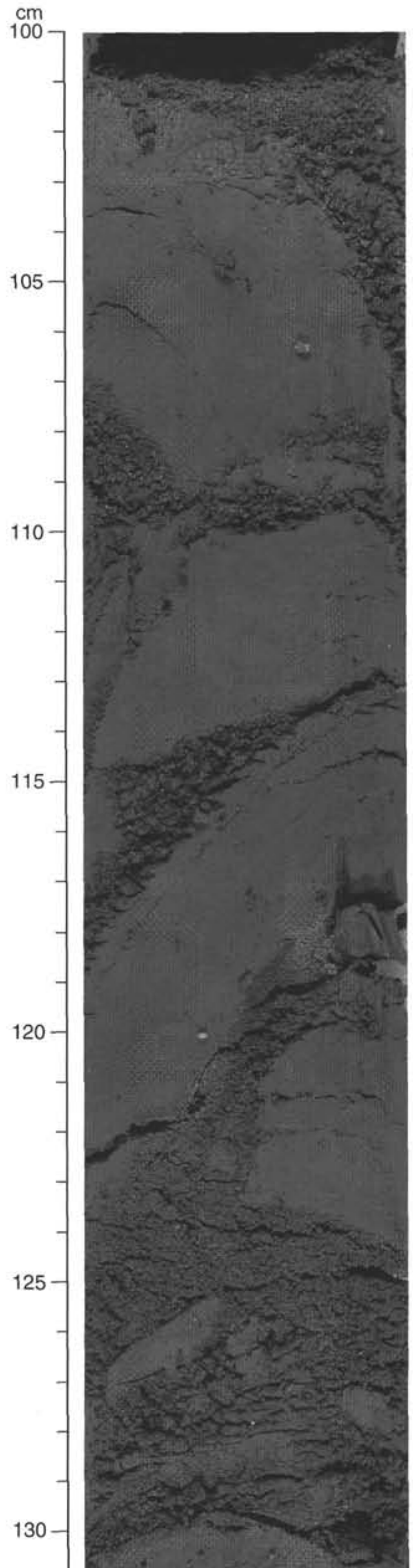


Figure 9. Mud clasts of various sizes in a fine- to coarse-sand matrix in Subunit IIIA (interval 155-936A-10H-1, 100–131 cm).

cores suggest that some beds were deposited by turbidity currents, whereas others were probably emplaced by sandy mass flows such as debris flows. The base of Subunit IIIA corresponds approximately to the base of coarse deposits on the wireline logs as well as a sharp change in lithology downhole to beds of finer sediment (Fig. 5).

*Subunit IIIB*

Subunit IIIB extends from 106.30 to 117.0 mbsf (interval 936A-13X-1, 0 cm, through -14X-1, 110 cm) and is a short interval of very dark gray (5Y3/1) clay with silt laminae and thin beds of silt to fine sand. The upper part of the section is slightly bioturbated. The clays are color banded throughout because of alternating, discontinuous hydrotroilite-stained bands and zones of no stain. Color bands are spaced at about 1- to 2-cm intervals (Fig. 10). On average, this subunit has about five silt laminae and silt to fine sand beds per meter. Laminae are most common; however, beds up to 4 cm thick occur that commonly show parallel laminations and, less commonly, cross-laminations and normal grading (Fig. 10). The wireline logs show that this subunit has much finer sediment than that in Subunits IIIA and IIIC. Subunit IIIB apparently represents an interval of overbank turbidite deposits on a channel levee, similar to the deposits of Subunit IIB.

*Subunit IIIC*

Subunit IIIC extends from 117.0 to 154.5 mbsf (interval 936A-14X-1, 110 cm, through -18X-1, 0 cm) and, based on recovered sediment, represents an interval of silty clay with graded silt and sand beds. Although recovery was very poor (~23%; Figs. 4 and 5), the wireline logs clearly show that this subunit is much sandier than Subunit IIIB; thus, we have designated this interval as a separate subunit. Interval 936A-14X-1, 112 cm, through -CC, 23 cm, contains two silt and fine sand beds, which are 15 cm and 20 cm thick; the 20-cm-thick bed is graded and contains a few small mud clasts. Core 936A-15X had little recovery (41 cm total) and consists of very dark gray (5Y 3/1) silty clay with two 2-cm-thick silt to fine sand beds. The 70 cm of sediment recovered in Core 936A-16X includes a thick bed (>25 cm) of fine sand in which mud clasts are common. Both cores suffered severe coring disturbance. Core 936A-17X had better recovery (63%) and consists of dark gray (5Y 4/1) silty clay with numerous silt to fine sand beds up to 15 cm thick that commonly have parallel lamination or cross-lamination. Based on the recovered core, Subunit IIIC apparently is a series of thin to medium turbidite beds of silt to fine sand interbedded with silty clay. The recovered sediment is similar to that of Subunit IIIB, except the silt to sand beds of IIIC appear to be somewhat thicker.

***Unit IV***

Interval: 155-936A-18X-1, 0 cm, through -32X-4, 26 cm
Age: late Pleistocene
Depth: 154.50 to 294.16 mbsf

Unit IV is a thick sequence of predominantly silty, commonly sandy, clay that ranges in color from dark olive gray (5Y 3/2) through very dark gray (5Y 3/1) to black (5Y 2.5/1 to N2). The carbonate content is uniformly low (~1.5% to 3%) throughout the unit. In contrast to the units above and below, core recovery within Unit IV was very good (86%; Figs. 4 and 5). Although many of the cores in this unit appear to be undisturbed clay, other cores show evidence of soft-sediment failure; this includes deformation and redeposition in the form of changes in lithology, color, folding, and flowage; occurrence of mud clasts; and abrupt, dipping, commonly irregular, lithologic contacts (e.g., Fig. 11). Closer inspection of many of the apparently undisturbed cores shows more subtle changes in lithology, sharp contacts, and deformation structures that indicate that this sediment is also disturbed by soft-sediment deformation. The wireline logs show that this entire unit is consistently clay. Therefore, the unit has

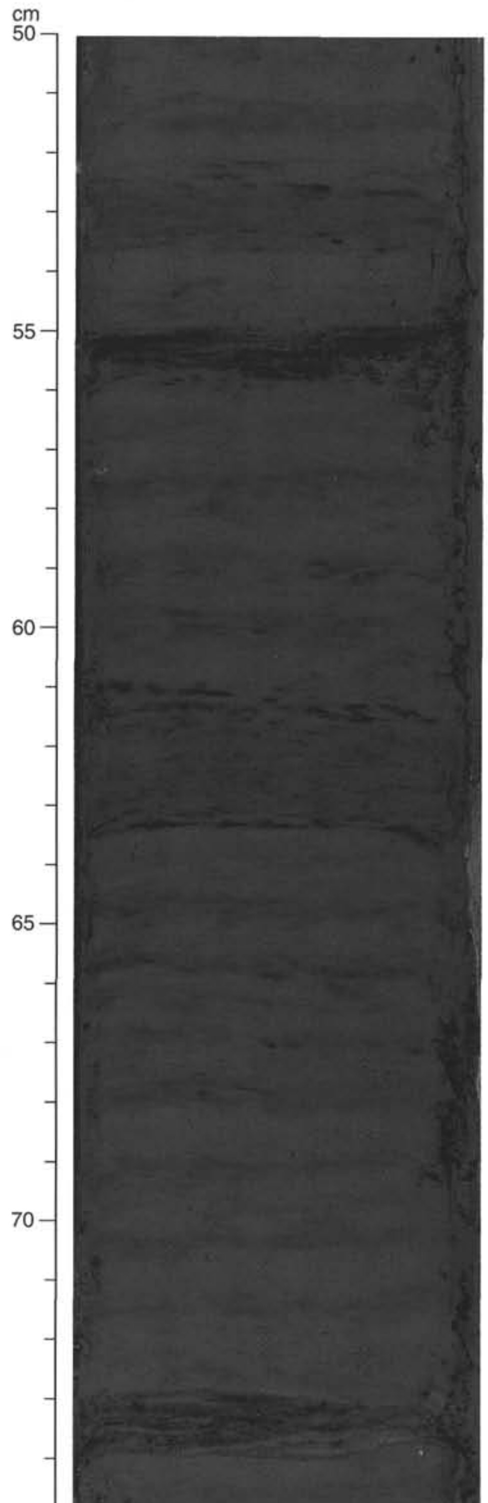

Figure 10. Color-banded silty clay with silt laminae from Subunit IIIB (interval 155-936A-13X-3, 50–75 cm). The silt laminae at 55 cm and 73 cm show cross-lamination.

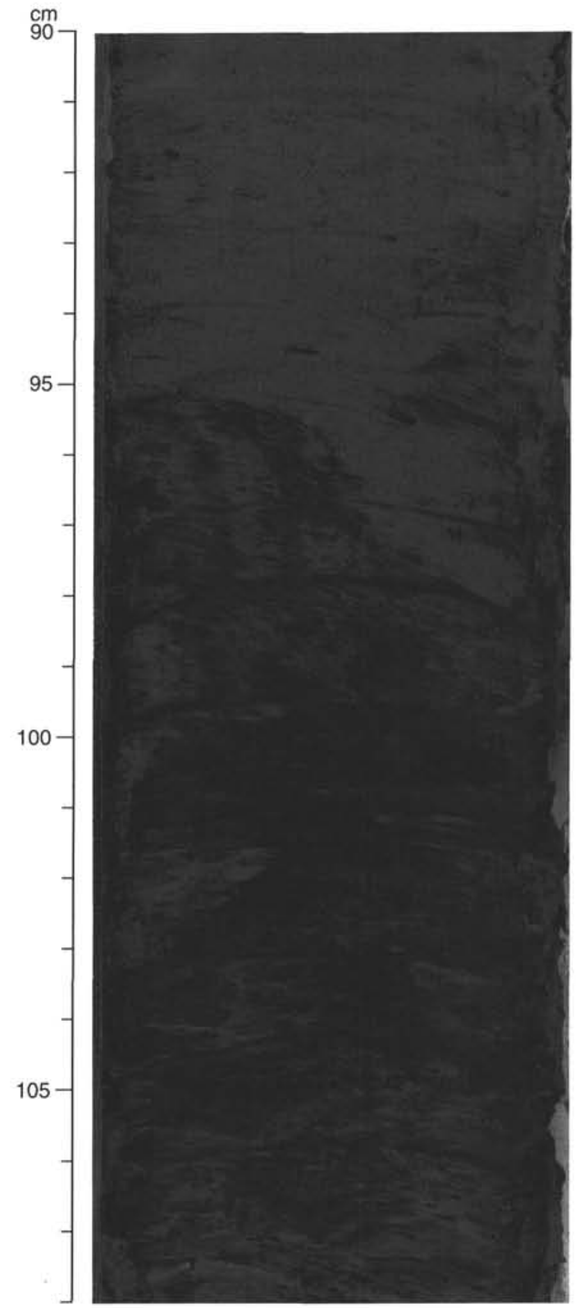

Figure 11. Irregular dipping contact at 95–98 cm between contrasting lithologies in Unit IV (interval 155-936A-18X-2, 90–108 cm).

not been subdivided. The following is a description of some of the representative lithologies and features observed in this thick unit.

The interval 936A-18X-1, 0 cm, through -CC, 38 cm, provides examples of changes in lithology bounded by abrupt, irregular contacts (Fig. 11). In addition, some intervals in this core contain mud clasts of various shapes, orientations, and variegated shades of gray color (Fig. 12). Some of the mud clasts appear to be deformed. Wood and shell fragments, plus granules and pebbles up to 0.5 cm in diameter, rarely occur. The sediment recovered in interval 936A-19X-1, 0 cm, through -23X-4, 135 cm, shows similar gray to black lithologic intervals with variable mud and sand contents and abrupt contacts. Deformed and folded beds, as well as deformed mud clasts of variable lithologies, form "wood-grain" or "chevron" patterns because of "biscuit" formation by drilling disturbance (Fig. 13; see "Lithostratigraphy" section in the "Explanatory Notes" chapter, this volume). Wood fragments and rock pebbles to granules are rare in this interval.

The remainder of the section downhole to the base of the unit (interval 936A-23X-4, 135 cm, through -32X-4, 26 cm) consists predominantly of very dark gray (5Y 3/1)silty clay. Some parts of this interval show no apparent evidence of disturbance or deformation,

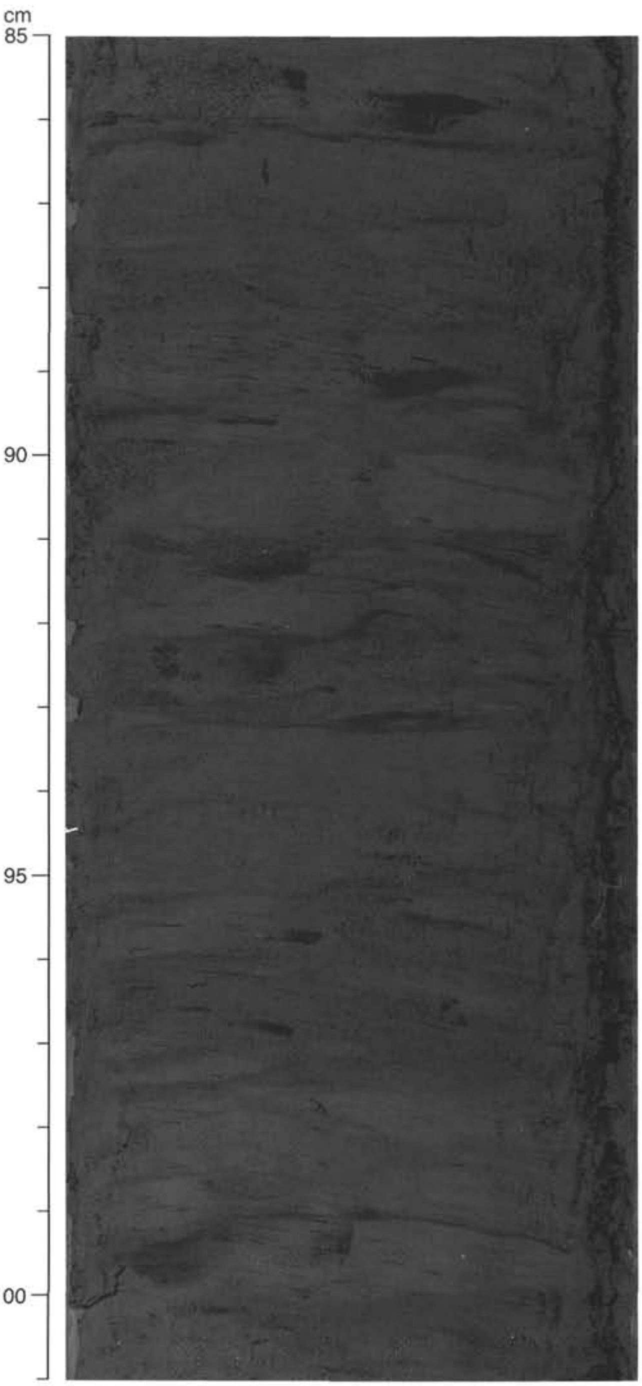

Figure 12. Mud clasts of various shapes and variegated color in Unit IV (interval 155-936A-18X-3, 85–101 cm). Some clasts appear to be deformed.

whereas other intervals show only a faint or subtle "wood-grain" pattern indicative of disturbance. However, a few zones do reveal that this interval is disturbed. Intervals 936-26X-6, 10–16 cm and 23–27 cm, are beds of deformed black (N2) clay that may be deformed mud clasts. Interval 936A-28X-2, 0 cm, through -CC, 20 cm, contains beds of variegated shades of black (N2 to 5Y 2.5/1) silty clay and sandy mud that have dipping, irregular contacts, as well as internal zones with a faint "wood-grain" pattern. Rare wood fragments and flakes and sand blebs occur. These beds may actually be thick mud clasts.

Core 936A-25X contains silty clay with flowed, folded, or stretched, discontinuous sand stringers and blebs. Clasts of sand occur, and some show parallel lamination, and rarely, cross-lamination within them (Fig. 14A). One of these sand clasts had cross-laminae that appeared to be upside down (interval 936A-29X-5, 100–101 cm). Thus, these sand clasts appear to be derived from formerly in-place silt and fine sand beds. Core 936A-30X has silty clay that appears undeformed; however, rare rock granules (Fig. 14B) and sand clasts are scattered within the clay.

The base of Unit IV is marked by a sharp horizontal contact and a change from black (5Y 2.5/1) silty clay in Unit IV to dark olive gray (5Y 4/1) silty clay of Subunit VA below. The sharply contrasting lithologies of the beds in Unit IV, together with distinct dipping contacts, mud clasts, scattered wood fragments and rock pebbles, and deformed, folded, and sheared(?) beds all indicate that this unit was deposited by mass-transport processes, probably muddy debris flows and possibly slumps. The number of depositional events is uncertain.

### *Unit V*

Interval: 155-936A-32X-4, 26 cm, through -44X-1, 69 cm
Age: middle Pleistocene
Depth: 294.16 to 405.69 mbsf

Unit V is characterized by fine to coarse sandy deposits interbedded with silty clay and is subdivided into Subunits VA to VD based on the variable lithologies present. However, the true boundaries of these subunits are somewhat uncertain because of the poor core recovery throughout this section (Figs. 4 and 5). Unfortunately, only the uppermost portion of this unit (<320 mbsf) was successfully logged, so wireline logs cannot be used to help define boundaries.

#### *Subunit VA*

Subunit VA extends from 294.16 to 307.35 mbsf (interval 936A-32X-4, 26 cm, through -33X-CC, 30 cm) and consists of very dark gray (5Y 3/1 to 5Y 4/1) silty clay with abundant silt laminae and thin to medium beds of silt to fine sand. The silt and sand beds are 1 to 25 cm thick (average = 5 cm) and many show parallel or cross-laminations. The beds commonly show normal grading with sharp, irregular basal contacts and grade from fine sand up to homogeneous clay (Fig. 15). This subunit averages about three to four silt laminae and/or beds of silt and fine sand per meter. The carbonate content is uniformly low (~2%–3.5%). Subunit VA represents a series of thin to medium thickness turbidites in overbank levee deposits.

#### *Subunit VB*

Subunit VB extends from 307.35 to 377.40 mbsf (interval 936A-33X-CC, 30 cm, through -41X-1, 140 cm) and apparently represents sediment of much coarser grain size than in Subunit VA. This subunit had the lowest core recovery rate (8%) of any unit in the hole (Fig. 4). Intervals 936A-35X-1, 10–35 cm, and 50–94 cm, consist of fine to medium sand with zones of high concentrations of organic detritus. Although both sand beds are very unconsolidated, they appear to be slightly graded and have sharp bases and gradational tops. No sediment was recovered in Cores 936A-36X, -37X, -38X, and -40X; however, several siltstone pebbles up to 6 cm long, plus a rock pebble, were recovered from -36X-CC (Fig. 16A) and a few similar but smaller siltstone pebbles were recovered from -38X-CC. The largest pebble in -36X-CC is lithified olive (5Y 5/2) silty claystone with ~25% silt. The silt in this pebble is ~95% angular quartz with minor mica and plant fragments. One well-defined silt lamina occurs, as well as burrow-mottled zones and a "clotted" texture in the mud, which suggests pellets or fine burrows. There are several scattered radiating (rosette) crystal growths up to 1 mm diameter (Fig. 16B). These crystals turned a bluish-white color after one day and are thus probably vivianite.

Interval 936A-39X-1, 0 cm, through -CC, 8 cm, consists entirely of 96 cm of dark gray (5Y 3/1) structureless fine sand with disseminated organic detritus. Interval 936A-41X-1, 0–140 cm, marks the base of Subunit VB and consists of sandy mud to muddy sand with

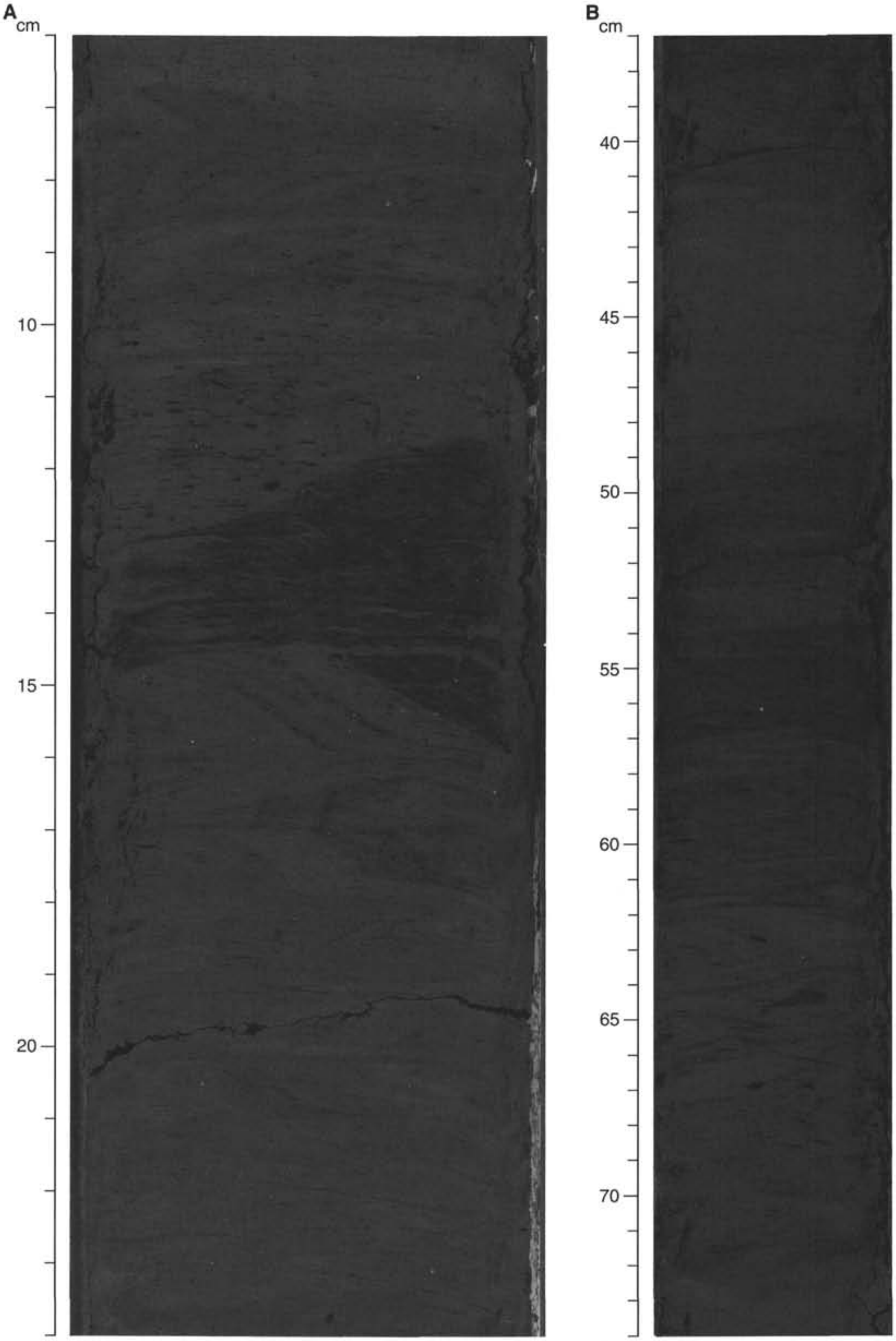


Figure 13. Deformed, folded, and possibly sheared laminae, beds, and mud clasts in Unit IV. **A.** Interval 155-936A-19X-6, 6–24 cm. **B.** Interval 155-936A-21X-2, 37–74 cm. Note the "wood-grain" and "chevron" patterns caused by "biscuit" formation during drilling disturbance (see "Lithostratigraphy" section of the "Explanatory Notes" chapter, this volume).

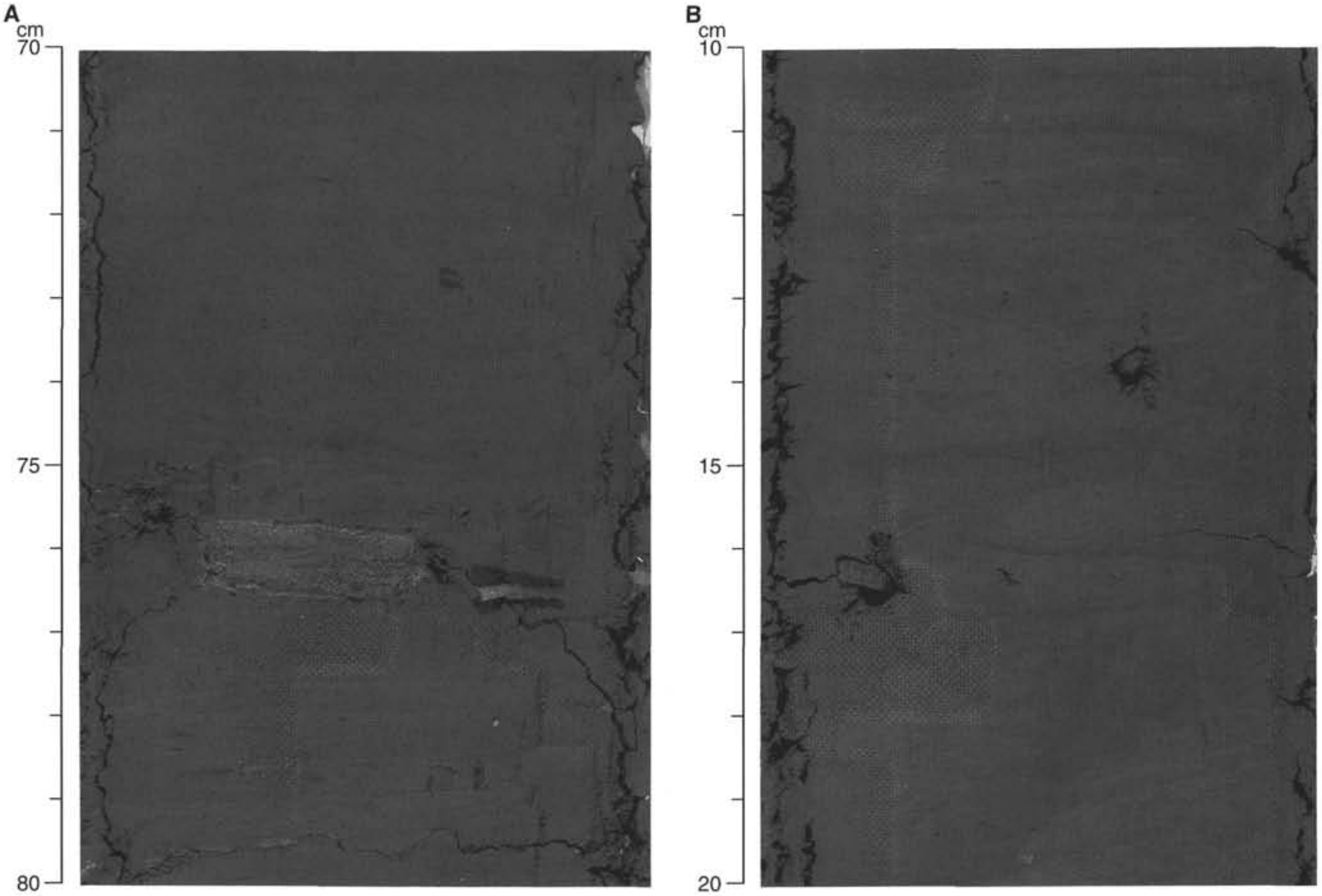


Figure 14. Sand and rock clasts in Unit IV. **A.** Small clast of cross-laminated silt and fine sand (interval 155-936A-29X-2, 70–80 cm). Note: small white particle to the right of the clast is a piece of plastic core liner. **B.** Rock granules in silty clay (interval 155-936A-30X-2, 10–20 cm).

scattered mud clasts of various sizes and disseminated organic detritus, which includes wood chips up to 3 cm long (Fig. 17).

The coarse deposits recovered and the poor core recovery indicate that this subunit must consist primarily of sand and possibly coarser grained deposits. The uppermost portion of this subunit was logged (<325 mbsf; see "Downhole Logging" section, this chapter), and an abrupt increase in sand content apparently occurs from 310 to 325 mbsf. Subunit VB thus appears to represent thick sand and possibly coarser grained deposits.

*Subunit VC*

Subunit VC is a short interval that extends from 377.40 to 387.52 mbsf (936A-41X-1, 140 cm, through -42X-2, 32 cm). This subunit consists of very dark gray (5Y 4/1 to 5Y 3/1) silty clay with abundant silt and fine sand laminae and beds, and is quite similar to Subunit VA. Silt to fine sand beds range up to 18 cm in thickness and many are normally graded with sharp bases. A few show mud-draped cross-laminations (Fig. 18). Carbonate content ranges from 1.9% in the upper part of the subunit to 11.7% near the base. This subunit appears to represent overbank turbidites in a levee sequence. However, because this section is from a zone of poor core recovery between two zones of mass-transport deposits, we cannot rule out that some or all of the sediment of this subunit may be displaced blocks.

*Subunit VD*

Subunit VD extends from 387.52 to 405.69 mbsf (intervals 936A-42X-2, 32 cm, through -44X-1, 69 cm) and consists mainly of silty clay to sandy mud of variable lithologies and colors. Mud clasts of various sizes are common throughout and many of the thicker beds may actually be clasts or blocks. The carbonate content is low (~2%–4%); however, significantly higher values occur in a few intervals as noted below. The top of the unit is marked by a 5-cm-thick bed of black (N2) sandy mud (Fig. 18) that has an irregular, scoured(?) base and a higher than normal carbonate content of 8.7%. Interval 936A-42X-2, 36 cm, through -CC, 10 cm, consists of mud-clast conglomerate, which is clast-supported and has a marble-like appearance (Figs. 19 and 20A). The elongated mud clasts show a range of colors (medium gray, 10Y 4/1, to black, N2), thicknesses (from <1 to >20 cm), and lithologies (sandy mud to carbonate-rich clay). Most clasts extend beyond the core diameter and are marked by irregular sharp boundaries and color changes (Figs. 19 and 20A). Two clasts are composed of medium gray carbonate-rich (22%–32%) clay (Fig. 20A). These high carbonate values compared to the very low values (2%–4%) of the rest of the subunit provide additional evidence that these beds are displaced clasts or blocks.

The sediment of interval 936A-43X-1, 0 cm, through -44X-1, 69 cm, appears to be a mud-clast conglomerate composed of a thick series of displaced beds or clasts of variable size and lithologies. Colors range from gray to black. Deformed mud clasts of variegated color occur from 936A-43X-3, 130 cm, to -4, 15 cm (Fig. 20B), and the dark gray to black sandy mud just beneath has numerous, scattered, angular mud and sand clasts of various sizes and lighter colors (Fig. 21A). A sharp horizontal boundary (Fig. 21B) marks the base of this sandy mud and of Subunit VD, which appears to be composed entirely of displaced sediment that was probably emplaced by muddy debris flows.

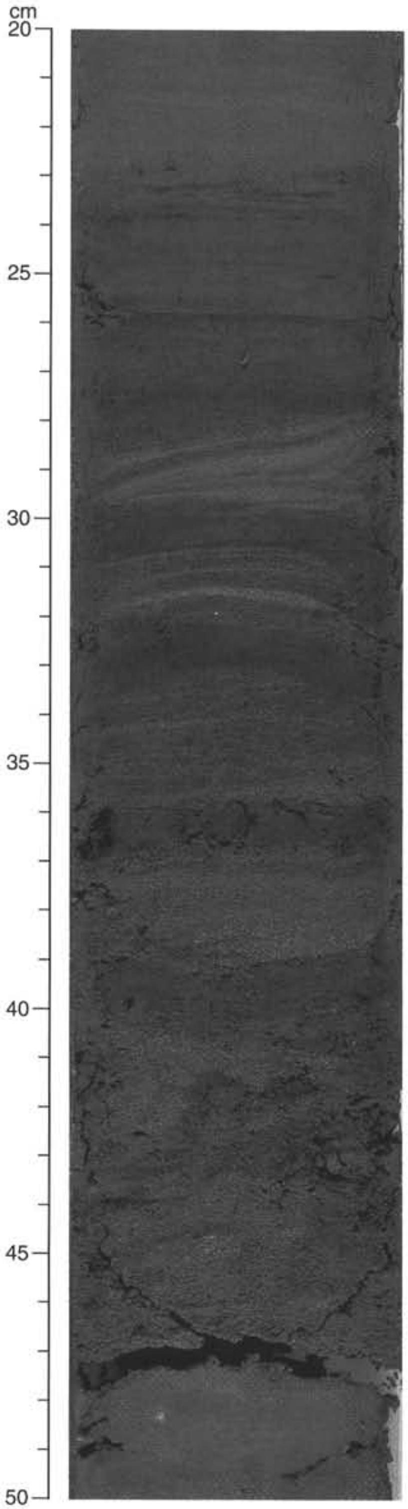


Figure 15. Normally graded bed of fine sand to clay in Subunit VA (interval 155-936A-32X-6, 20–50 cm). Note that moderately dipping laminae between 27 and 30 cm were caused by drilling disturbance.

### *Unit VI*

Interval: 155-936A-44X-1, 69 cm, through -46X-CC, 38 cm
Age: middle Pleistocene
Depth: 405.69 mbsf to 426.20 mbsf

Unit VI extends from the sharp boundary at the base of Unit V (Fig. 21B) to the base of the hole (Figs. 4 and 5) and shows a markedly different lithology from Subunit VD above. This unit is divided into two thin subunits, VIA and VIB. The lithologic boundary between these two subunits is gradational and is arbitrarily placed just above the first downhole occurrence of silt and fine sand laminae and beds in the unit.

#### *Subunit VIA*

Subunit VIA extends from 405.69 to 415.34 mbsf (936A-44X-1, 69 cm, through -45X-1, 74 cm) and consists of dark gray (5Y 4/1) silty clay, which grades downward into very dark gray (5Y 4/2) silty clay (Fig. 21B). Silt laminae are rare. The sediment of this subunit is slightly to moderately burrowed, and foraminifers are common. The carbonate content is 6.7% in Sample 936A-44X-2, 57–58 cm, and decreases downward to 3.7% near the base of the subunit; however, the carbonate content may be somewhat higher near the top of the subunit because foraminifers are most common in that zone. These carbonate values are relatively high for this type of sediment, and this subunit apparently represents hemipelagic sedimentation. The lower boundary is gradational.

#### *Subunit VIB*

Subunit VIB extends from 415.34 to 426.20 mbsf (936A-45X-1, 74 cm, through -46X-CC, 38 cm) and consists of very dark gray (5Y3/1) clay to silty clay with numerous silt laminae and common beds of silt to fine sand up to 13 cm thick. Beds are thickest and most frequent in interval 936A-45X-3, 0 cm, through -4, 150 cm, and -46X. Some laminae and beds show parallel and/or cross-lamination. The carbonate content is uniformly low (~2.5%–3.5%). This subunit apparently represents overbank turbidity-current deposition in the uppermost portion of a levee deposit. Apparently turbidity-current deposition gradually ceased or was sharply reduced, and hemipelagic deposition ensued and deposited Subunit VIA.

## Mineralogy

Mineralogy was determined by estimation of mineral volume percentages in smear slides, three thin sections, and by X-ray diffraction (XRD) analysis of samples from silt laminae and beds.

### *Smear-slide Synthesis*

Silty clay is the dominant lithology of Units II, IV, and VIB, and is composed of 50%–90% clay with 10%–50% silt. The silt is approximately 70%–75% quartz (mainly monocrystalline), 15% feldspar (mainly plagioclase), 7% mica, and 15% accessory minerals. The accessories include common hornblende (green), augite, hypersthene, opaques, rare zircon, spinel, and monazite. Organic detritus, foraminifers, and sponge spicules compose less than 5%; nannofossils compose less than 1%.

Unit III consists of fine to coarse sand, commonly with mud clasts, interbedded with silty clay with laminae and beds of silt and fine sand. The fine to medium sand types of Subunit IIIA (e.g., Sample 936A-10H-1, 1–2 cm) consist of about 70% quartz (mainly monocrystalline), 4%–12% feldspar (mainly plagioclase), 1%–6% mica, 1%–6% amphibole and pyroxene, and 1%–6% opaque minerals, which include hydrotroilite and unidentified oxides. Approximately 50% of the quartz and feldspar grains are well rounded, frequently with iron-oxide surface coatings. This distinguishes them from the finer silt grains, which are angular to subangular.

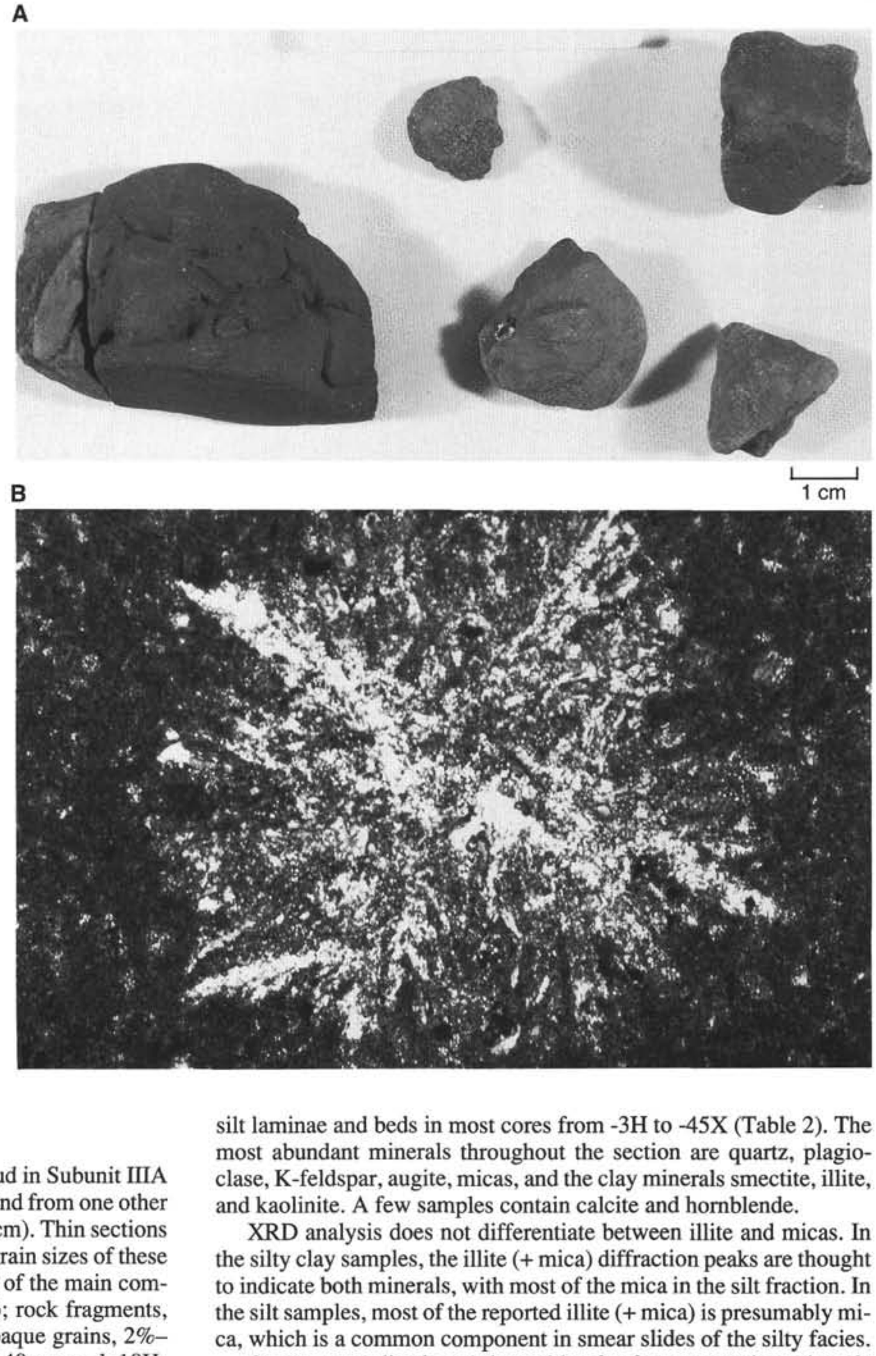


Figure 16. **A.** Olive-colored siltstone pebbles and a sandstone pebble (top center) recovered in Section 155-936A-36X-CC in Subunit VB. Scale shown under photo. **B.** Photomicrograph in cross-polarized light of radial, bladed ?vivianite crystals (Sample 155-936A-36X-CC, 0–3 cm). Scale: 69 mm on photo = 1 mm.

### *Sand Petrography from Thin Sections*

Sand was sieved from two intervals of sandy mud in Subunit IIIA (Samples 936A-9H-1, 38–40 cm, and 90–100 cm) and from one other sand bed from this unit (Sample 936A-10H-1, 1–2 cm). Thin sections were cut from grain mounts of these samples. The grain sizes of these samples is 0.2–0.4 mm. The estimated percentages of the main components are: quartz, 55%–80%; feldspar, 8%–15%; rock fragments, 5%–20%; accessory (heavy) minerals, 5%–7%; opaque grains, 2%–5%; and micas, about 1%. Samples 936A-9H-1, 38–40 cm, and -10H-1, 1–2 cm, contain 1%–2% planktonic and benthic foraminifers.

Twinned feldspars (?plagioclase) are commonly fresh and angular to subangular, whereas many untwinned feldspars (?K-feldspar) are partially altered to phyllosilicate minerals (Fig. 22A). Rock fragments include pieces of shale, ?slate, ?basalt with microlitic texture, siltstone, and chert. Accessory minerals include abundant green hornblende and euhedral enstatite, common augite (Sample 936A-10H-1, 1–2 cm), and rare epidote, hypersthene, clear garnet, zircon, and blue polycrystalline vivianite. Quartz grains are generally subangular to subrounded, except for the largest quartz grains in each sample, many of which are well rounded.

### *XRD Data*

X-ray diffraction analysis was performed on four bulk samples of silty clay from Cores 936A-1H and -2H, and on bulk samples from silt laminae and beds in most cores from -3H to -45X (Table 2). The most abundant minerals throughout the section are quartz, plagioclase, K-feldspar, augite, micas, and the clay minerals smectite, illite, and kaolinite. A few samples contain calcite and hornblende.

XRD analysis does not differentiate between illite and micas. In the silty clay samples, the illite (+ mica) diffraction peaks are thought to indicate both minerals, with most of the mica in the silt fraction. In the silt samples, most of the reported illite (+ mica) is presumably mica, which is a common component in smear slides of the silty facies.

Quartz-normalized peak intensities for ferromagnesian minerals and feldspars are fairly constant throughout the cored interval (Fig. 23A). The only component that shows a large stratigraphic variation is the sum of clay minerals and micas. These minerals show a sharp decline in relative abundance between samples at 72.2 and 89.8 mbsf (i.e., at the contact between Units II and III). Ratios between the intensities of clay-mineral and mica peaks (Fig. 23B) show that this downhole decline in abundance is a result of a decrease in illite (+ mica). Because most samples are silt, the implication is that silt beds below Unit II contain less mica than shallower silt beds. Insufficient smear slides of silt were examined to independently confirm this inference.

## Spectrophotometry

Reflectance of visible light was low throughout the sediment column at Site 936. Reflectance values range between 15% and 25% for

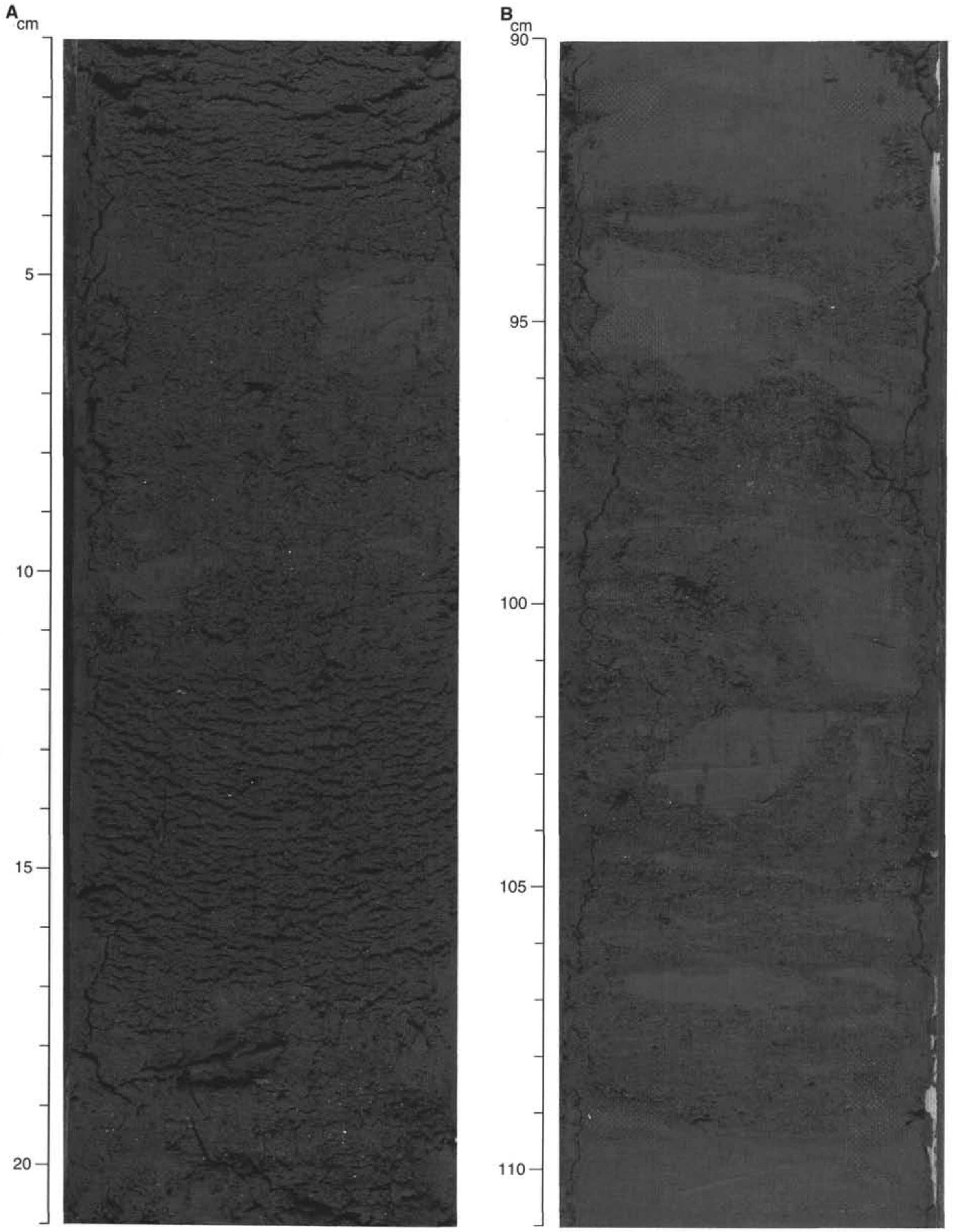


Figure 17. Mud clasts in sandy mud from Subunit VB. **A.** Interval 155-936A-41X-1, 1–21 cm. Note large wood chip at 18.2 cm. **B.** Interval 155-936A-41X-1, 90–111 cm.

all wavelength bands from 400 to 700 nm. Most significant correlations between spectrophotometry results and defined lithologic units exist in the ratio of the red (650–700) vs. the blue (450–500) spectrum (Fig. 4). Positive deviations from the mean red/blue reflectance value of 1.12 in Hole 936A are mainly determined by the content of iron oxyhydroxides associated with sand layers in Units III and VB, and with the brown calcareous clay in Unit I.

The high-frequency variability in the red/blue reflectance ratio observed between 5 and 72 mbsf (Unit II) is characteristic for the dark gray, black mottled, and color-banded silty clay, which contains abundant laminae and beds of silt and fine sand. In contrast, the silty clay with mud clasts of the mass-flow deposits of Unit IV exhibits much less variability in the red/blue signal (Fig. 4). Most negative deviations from the mean red/blue ratio are associated either with the

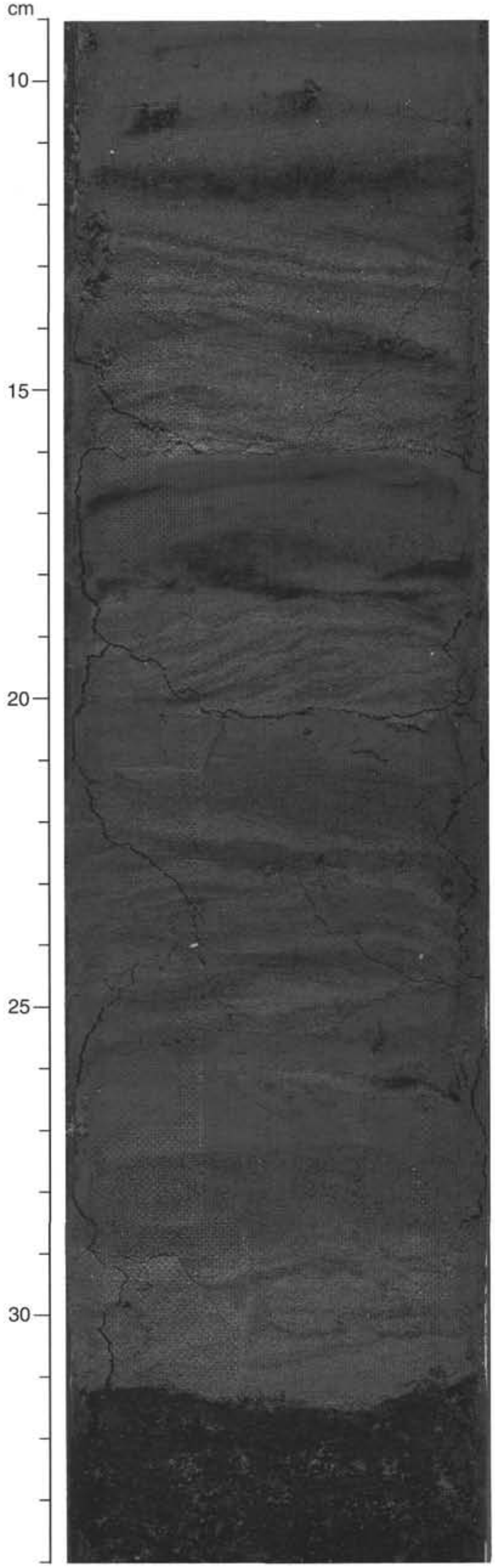


Figure 18. Examples of silt to fine sand beds in Subunit VC (interval 155-936A-42X-2, 9–34 cm). Note mud-draped cross-laminae in the intervals 14–16 cm and 18–20 cm. Irregular contact at the top of the black sandy mud bed (31–32 cm) marks the top of Subunit VD.

very dark gray and black mottled silty clay, which is barren of silt and sand beds (Unit IV: 155 to 185 mbsf), or with the calcareous clay of Subunit VIA, in which the iron occurs as iron sulfide.

## Discussion

The lithologic units recovered at Site 936 highlight the wide variability in fan lithologies and depositional processes. Hole 936A penetrated levee sediment of both the Amazon and the Brown Channel-levee systems, the associated HARP units directly below, the entire thickness of Unit R, and the underlying levees of older channel-levee systems of the Middle (Red Channel-levee System) and the Lower (Gold Channel-levee System) Levee complexes.

Subunit VIB, the deepest unit recovered, apparently represents a fining- and thinning-upward series of overbank turbidites in the upper part of the Gold Channel-levee System (see "Core-Seismic Integration" section, this chapter). These overbank deposits grade upward into the thin hemipelagic interval of Subunit VIA, which indicates that turbidity-current sedimentation on this levee must have slowed and then halted, at least temporarily. Unit VI may represent a comparable depositional history to that shown by Unit II at the top of the section.

Subunit VD is composed predominantly of silty clays to sandy mud with mud-clast conglomerates. The mud clasts and blocks(?) suggest emplacement by muddy debris flows. In contrast, the silty clay with thin silt and fine sand laminae and beds of overlying Subunit VC apparently represent another sequence of overbank turbidites in the Red, or possibly the Gold, Channel-levee System.

Subunit VB represents deposition of much coarser and thicker deposits emplaced by turbidity currents and sandy mass flows that may represent channel deposits associated with the Red Channel-levee System. Similar, but slightly finer, channel deposits were found in the floor of the abandoned meander of the Amazon Channel at Site 934 (see Unit IV in the "Lithostratigraphy" section, "Site 934" chapter, this volume). Subunit VA shows a return to overbank levee sedimentation by turbidity currents within the Red Channel-levee System as evidenced by the graded thin- to medium-bedded turbidites that compose this subunit.

The thick muddy sequence represented in Unit IV shows contrasting abrupt changes in lithology, together with sharp dipping contacts, mud clasts, scattered wood fragments and rock pebbles, and deformed, folded, and sheared(?) beds. These features all indicate that this unit was deposited by mass-transport processes, probably muddy debris flows and possibly slumps. The number of depositional events is uncertain from the lithology; however, the wireline log and physical-property data may help to determine boundaries for individual events. Most of Unit IV corresponds to acoustic Unit R on seismic data, which has been interpreted as debris-flow deposits.

Subunit IIIC is a series of thin- to medium-bedded silt to fine sand turbidites in silty clays that apparently represent overbank deposits; however, the poor recovery from this unit and the wireline log data imply that even thicker and coarser beds may be present in this subunit. The recovered sediment is quite similar to the sediment of the overlying Subunit IIIB, which also represents an interval of overbank turbidite deposits; however, the silt and sand beds of Subunit IIIC appear to be thicker than those of IIIB.

Subunit IIIA contains the thickest, coarsest beds recovered in this hole and represents a series of thick beds of sand to gravel, which include black sandy mud, thin to thick normally graded sand beds, and thick beds of matrix-supported muddy sand with mud clasts. These lithologies suggest that some beds were deposited by turbidity currents, whereas others were emplaced by sandy mass flows such as debris flows. These beds probably represent channel or proximal lobe deposits. Similar, but slightly finer, channel deposits were found in the floor of the abandoned meander of the Amazon Channel (see Unit IV in "Lithostratigraphy" section, "Site 934" chapter, this volume). Erosional surfaces apparently mark the top and base of this subunit.

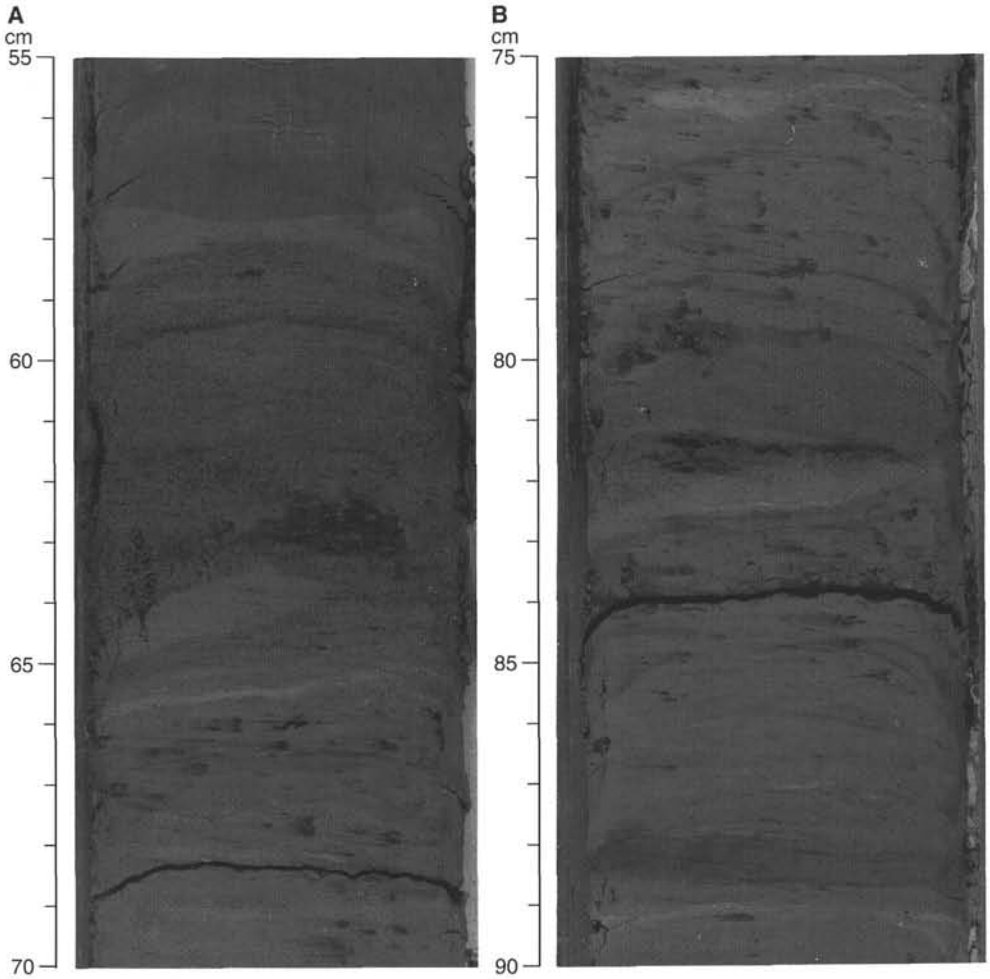


Figure 19. Elongated mud clasts of various sizes, colors, and lithologies in Subunit VD. Virtually all discrete lithologic units in these photos are individual mud clasts stacked one upon the other and with little or no matrix material (see text). **A.** Interval 155-936A-42X-2, 55–70 cm. **B.** Interval 155-936A-42X-2, 75–90 cm.

All of the deposits of Unit III apparently were recovered from the HARP acoustic unit at the base of the Upper Levee Complex.

Subunit IIB apparently represents a fining- and thinning-upward deposit of overbank turbidites in the Upper Levee Complex. Silt laminae are absent in overlying Subunit IIA, which suggests that overbank deposition stopped in the latest Pleistocene, and hemipelagic deposition ensued. Thus, Unit II represents a fining- and thinning-upward sequence that probably signals the cessation of sediment transport through the Amazon Channel. Hemipelagic sediment composes Unit I; however, this more carbonate-rich sediment apparently records the rather abrupt decrease in terrigenous sediment supply to the entire Amazon Fan in response to sea-level rise at the beginning of the Holocene (e.g., Damuth, 1977).

## BIOSTRATIGRAPHY

### Calcareous Nannofossils

Nannofossils are abundant and well preserved in the hemipelagic mud of Holocene age (Zone CN15b; Samples 936A-1H-1, 0–1 cm, through -1H-1, 43–46 cm). Nannofossils become rare and poorly preserved below 1.02 mbsf (Sample 936A-1H-1, 100–102 cm), a characteristic of the glacial-age sediment of the Amazon Fan (Table 3). Calcareous nannofossils are absent in Unit II and the upper part of Unit III from 17.6 to 74.1 mbsf in the pre-Holocene levee sequence of silty clay (Samples 936A-2H-CC, 21–22 cm, through -8H-CC, 25–26 cm). Calcareous nannofossils occur sporadically from 117.5 to 125.5 mbsf in the upper part of the underlying HARP unit in Subunits IIIA and IIIB (Samples 936A-14X-CC, 28–29 cm, to -15X-CC, 11–12 cm). Abundant and well-preserved nannofossils representing Zone CN15b, and thus younger than 85 ka, appear in Subunit IIIC from 147.4 to 149.07 mbsf (Sample 936A-17X-2, 111 cm, through -3, 127 cm). Sporadic and poorly preserved nannofossils are found in low abundances from 156.4 to 286.7 mbsf in the mass-transport Unit IV (Samples 936A-18X-2, 41 cm, through -31X-CC, 38–39 cm). An exception to this is an assemblage found in a clast at 158.2 mbsf, which contains reworked Miocene nannofossils, including common *Discoaster deflandrei* (Sample 936A-18X-3, 70 cm).

The sporadic occurrence of poorly preserved nannofossils continues from 299.1 to 385.8 mbsf in the underlying Subunits VA (silty sand turbidites) and VB (sandy mass flow) (Samples 936A-32X-CC, 32–33 cm, through -42X-1, 17 cm). At 386.8 mbsf within the overbank turbidite of Subunit VC, calcareous nannofossils become abundant and well preserved (Sample 936A-42X-1, 113–115 cm). *Emiliania huxleyi* is rare, which implies an age of 85 to 260 ka (Zone CN15a). The occurrence of well-preserved nannofossils continues downcore into the underlying debris flow (Subunit VD). The nannofossil assemblages remain unchanged across the lithostratigraphic boundaries.

Subunit VIA at 405.7 mbsf (Sample 936A-44X-1, 76–78 cm) is characterized by well-preserved nannofossil assemblages dominated by species of *Gephyrocapsa*. This assemblage includes common

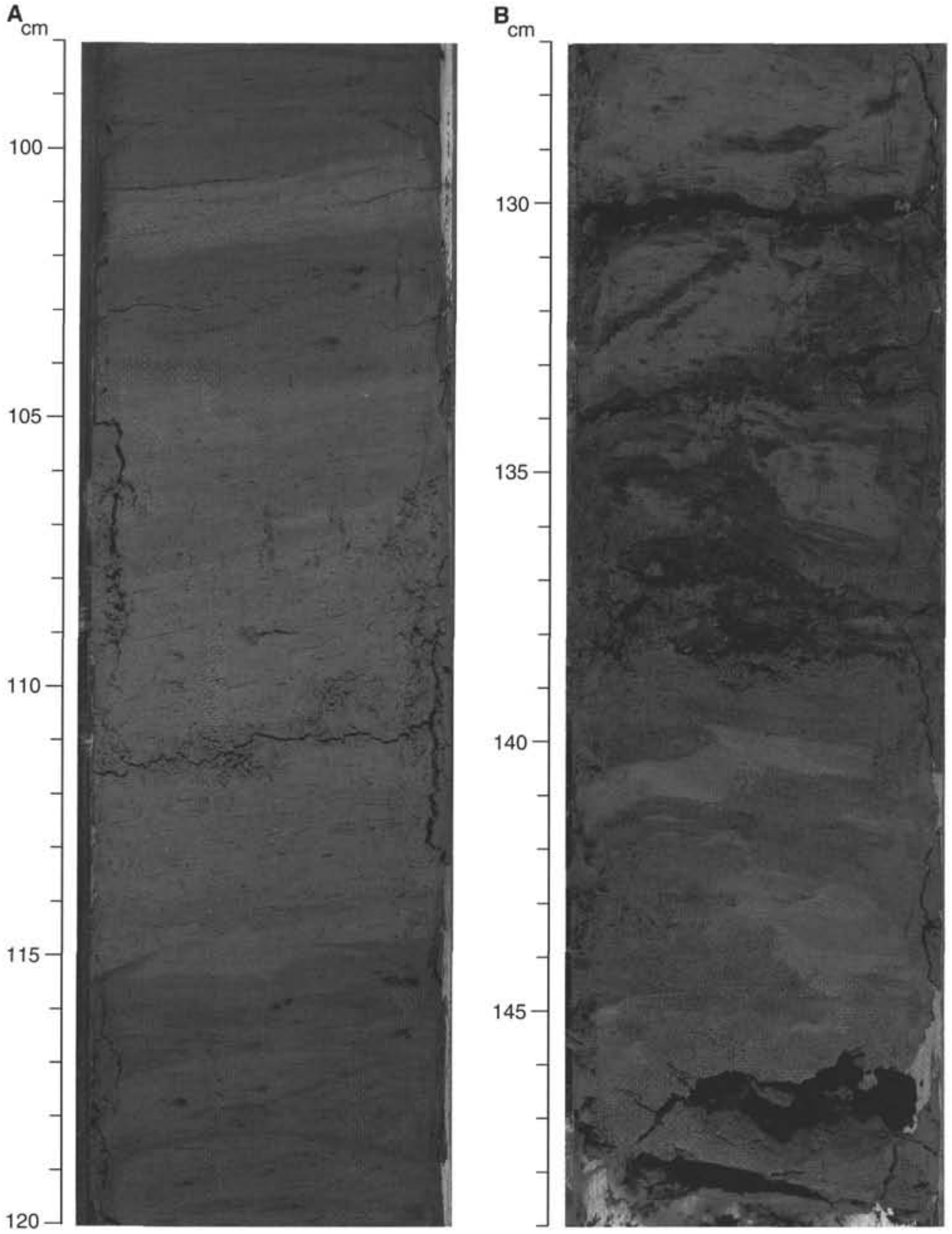


Figure 20. Mud clasts of various sizes, colors, and lithologies in Subunit VD. **A.** Interval 155-936A-42X-2, 98–120 cm. Note medium gray carbonate-rich clay clasts from 100 to 102 cm and ~105 to 115 cm. Carbonate contents are 22.4% at 107 cm and 32.2% at 112 cm (see previous figure and text). **B.** Interval 155-936A-43X-3, 127–149 cm.

*Helicosphaera inversa*. As *P. lacunosa* and *Emiliania huxleyi* are absent, an age of 0.46 to 0.26 Ma is assigned to this assemblage (Zone CN14b). The nannofossil assemblages of Subunit VIA have a true pelagic appearance with no signs of reworking. The lower part of Unit VI (Subunit VIB) at 422.9 mbsf is barren of calcareous nannofossils (Core 936A-45X).

## Planktonic Foraminifers

Ericson zones were assigned to sediment in Hole 936A. The boundary between Ericson Zone Z and Y (disappearance of *G. tumida*) is between 0.53 and 1.01 mbsf (Samples 936A-1H-1, 52–54 cm, and -1H-1, 100–102 cm; Table 4; Fig. 24).

Foraminifers are found in low abundances in Units II and III from 1 to 135 mbsf (Samples 936A-1H-1, 100–102 cm, through -16X-CC, 17–26 cm). The interval between the Z/Y boundary and 63 mbsf, in Unit II (Fig. 24), has been defined as the Y Zone on the basis of the absence of *G. menardii* and *G. tumida* (Sample 936A-7H-CC, 1–9 cm). The age of this interval can be constrained to younger than 40 ka by the absence of *P. obliquiloculata*. In the sandy Subunit IIIA, in the interval between 73 mbsf (Sample 936A-8H-CC, 16–25 cm) and 93 mbsf (Sample 936A-11X-CC, 17–26 cm), planktonic and benthic foraminifers are barren. From 96.7 to 135.8 mbsf in Subunit IIIB and the top of Subunit IIIC, rare *G. ruber* as well as wood, shell fragments, and sponge spicules occur (Samples 936A-12X-CC, 0–2 cm, through -16X-CC, 17–26 cm), suggesting that this interval is re-

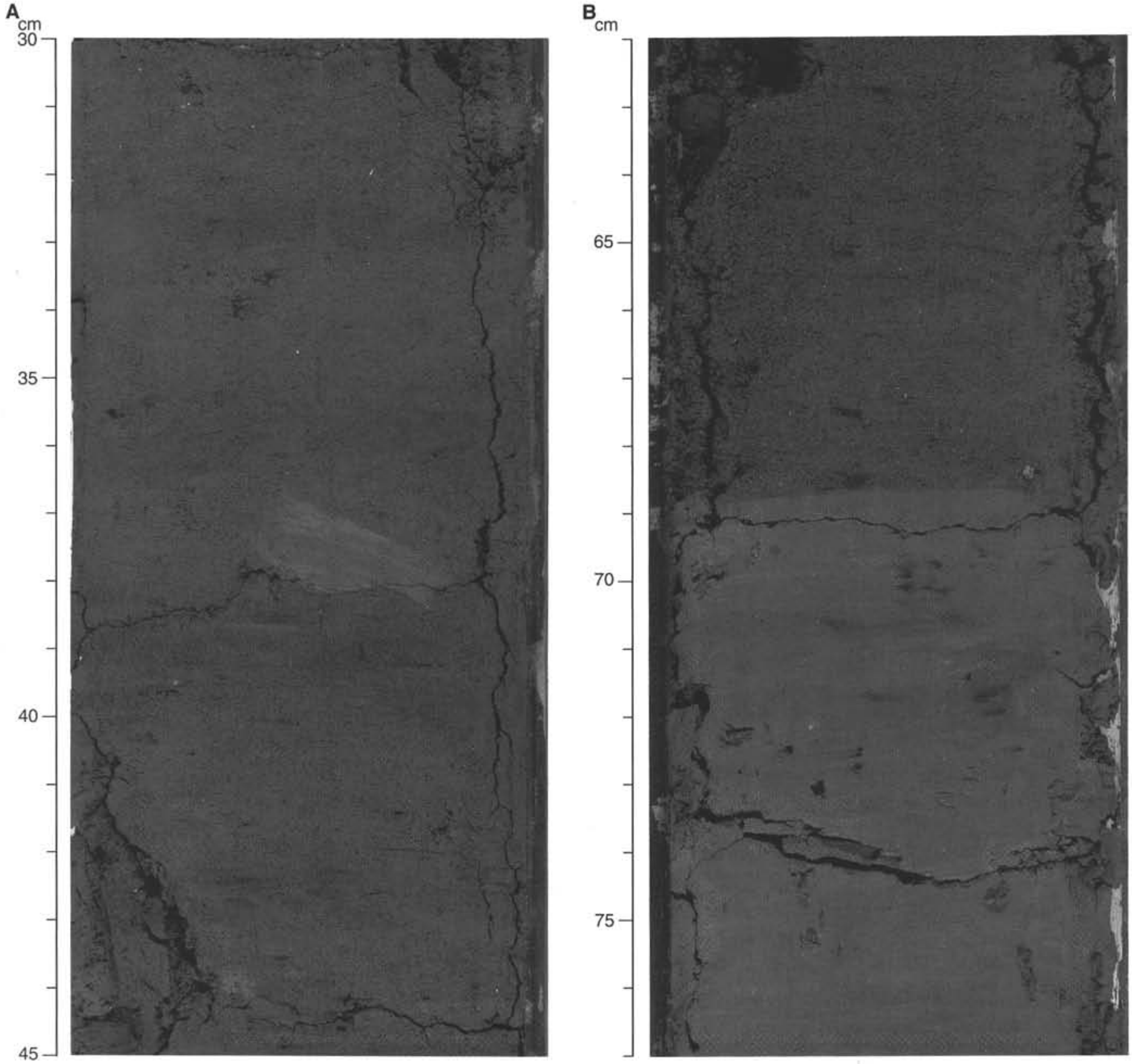


Figure 21. **A.** Dark-colored sandy mud in the lower part of Subunit VD with lighter colored angular mud clast (interval 155-936A-43X-5, 30–45 cm). **B.** Sharp lithologic boundary between Units V and VI at 69 cm (interval 155-936A-44X-1, 62–77 cm). Black sandy silty clay of Subunit VD overlies dark gray hemipelagic silty clay of Subunit VIA (see text).

worked. From 148.8 to 150.8 mbsf at the base of Subunit IIIC there are abundant foraminifers and no evidence of reworking (Samples 936A-17X-3, 99–104 cm, and -CC, 7–16 cm). Rare but well-preserved *P. obliquiloculata* are found at 148.8 mbsf (Sample 936A-17X-3, 99–104 cm), suggesting that this short section may be Y Zone, but older than 40 ka. The true position of the $Y_{P.\ obliq.}$ cannot be ascertained as the sediment above this interval is barren of foraminifers. Unit IV, described as a debris flow, has relatively high abundances of planktonic foraminifers indicative of the Y Zone before 40 ka, indicated by the presence of *P. obliquiloculata*. Unit IV from 172.2 to 286.7 mbsf (936A-19X-CC to -31X-CC, 38 cm) also contains the following:

1. high abundances of shell and wood fragments,
2. heavily calcified and iron-stained planktonic and benthic foraminifers,
3. high abundances of bathyal benthic foraminifers found usually above a water depth of 2000 m, in particular *Bulimina exilis* (see "Benthic Foraminifers" section).

These characteristics suggest that Unit IV is reworked. At the base of Unit IV there is another short interval between 299 and 307 mbsf, which is barren of all foraminifers (Samples 936A-32X-CC, 23–32 cm, and -33X-CC, 20–29 cm). Core recovery was very poor in Subunits VA and VB. In these subunits there are sporadic occurrences of

A B

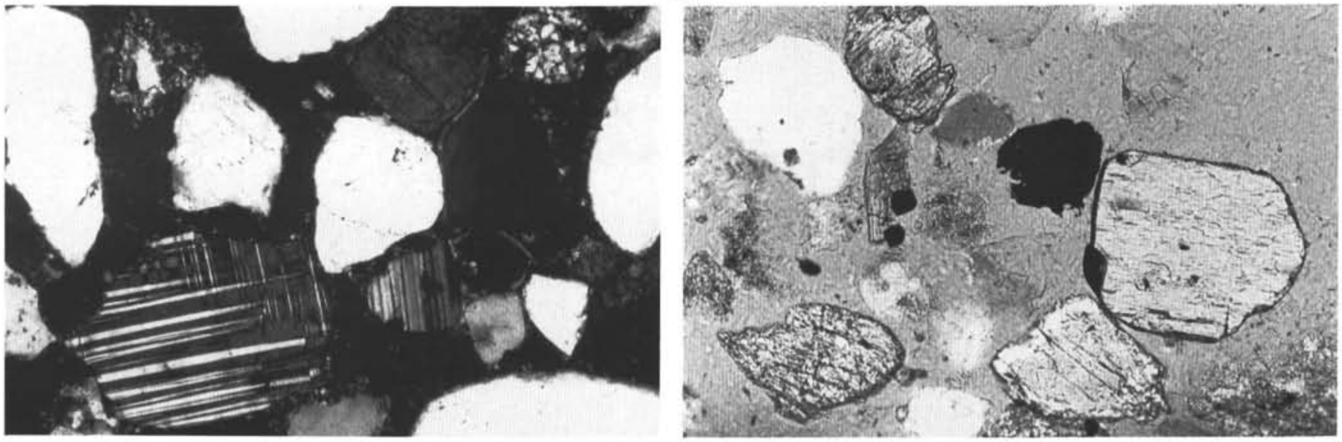

Figure 22. Thin-section photomicrographs (Sample 155-936A-10H-1, 1–2 cm), Subunit IIIA. **A.** Fresh twinned feldspar (bottom left) and partially altered untwinned ?K-feldspar (upper center); cross-polarized light. Scale: 54 mm on photo = 0.5 mm. **B.** Three moderate-relief angular grains of hornblende and a prismatic crystal of enstatite; plane light. Scale: 86 mm on photo = 0.5 mm.

**Table 2. Relative peak intensities of the main minerals in four silty clays and 25 silts from Hole 936A.**

| Core, section, interval (cm) | Lithology | Depth (mbsf) | Relative intensity of primary peaks | | | | | | | | |
|---|---|---|---|---|---|---|---|---|---|---|---|
| | | | Smectite | Mica + Illite | Kaolinite | Quartz | Plagioclase | K-feldspar | Augite | Hornblende | Calcite |
| 155-936A- | | | | | | | | | | | |
| 1H-1, 59–60 | Clay | 0.59 | 12.8 | 14.0 | 10.2 | 100.0 | 9.3 | * | * | * | * |
| 1H-3, 80–81 | Clay | 3.80 | 13.1 | 19.6 | 10.8 | 100.0 | 9.4 | 5.7 | * | * | * |
| 1H-4, 39–40 | Clay | 4.89 | 13.8 | 25.4 | 13.5 | 100.0 | 10.8 | * | 2.8 | * | * |
| 2H-1, 90–91 | Clay | 7.40 | 15.5 | 28.4 | 13.0 | 100.0 | 8.0 | 8.4 | 2.4 | * | * |
| 3H-5, 110–111 | Silt | 23.10 | 14.1 | 30.0 | 16.4 | 100.0 | 15.3 | 4.5 | 2.9 | * | * |
| 5H-6, 137–138 | Silt | 43.87 | 14.7 | 36.6 | 14.8 | 100.0 | 16.9 | 4.5 | 1.2 | 1.2 | * |
| 6H-3, 21–22 | Silt | 47.71 | 9.3 | 23.4 | 11.3 | 100.0 | 9.7 | * | 1.2 | 1.4 | * |
| 7H-5, 27–28 | Silt | 59.73 | 8.7 | 17.7 | 11.2 | 100.0 | 11.6 | 5.2 | 1.2 | 0.7 | * |
| 8H-6, 124–125 | Silt | 72.24 | 14.1 | 31.7 | 17.0 | 100.0 | 15.3 | 4.8 | 0.8 | 2.3 | * |
| 10H-5, 134–135 | Silt | 89.84 | 2.5 | 6.5 | 3.4 | 100.0 | 6.0 | 3.5 | 1.3 | 0.8 | |
| 11X-1, 83–84 | Silt | 92.83 | 5.5 | 8.9 | 4.6 | 100.0 | 11.0 | 5.8 | 1.0 | 2.6 | 0.4 |
| 13X-3, 73–74 | Silt | 110.03 | 3.6 | 7.7 | 4.3 | 100.0 | 10.9 | 3.3 | 1.4 | 1.2 | * |
| 14X-1, 104–105 | Silt | 116.94 | 6.5 | 8.8 | 5.1 | 100.0 | 13.2 | 3.8 | 1.5 | * | * |
| 17X-2, 53–54 | Silt | 146.83 | 5.2 | 11.5 | 5.8 | 100.0 | 10.0 | 4.6 | 1.6 | * | * |
| 19X-4, 84–85 | Silt | 169.44 | 8.5 | 10.7 | 5.2 | 100.0 | 10.2 | 4.3 | 1.8 | * | * |
| 21X-4, 86–87 | Silt | 188.76 | 2.2 | 5.0 | 3.6 | 100.0 | 8.4 | 3.8 | 0.8 | * | * |
| 23X-3, 129–130 | Silt | 207.09 | 4.8 | 8.0 | 3.6 | 100.0 | 8.8 | 4.4 | 1.1 | * | * |
| 24X-1, 53–54 | Silt | 213.03 | 6.3 | 6.3 | 4.8 | 100.0 | 10.1 | 4.0 | 1.6 | * | * |
| 26X-3, 52–53 | Silt | 235.22 | 8.1 | 15.0 | 7.5 | 100.0 | 8.0 | * | 2.2 | * | * |
| 27X-6, 122–123 | Silt | 250.12 | 2.5 | 6.2 | 3.1 | 100.0 | 13.6 | 3.1 | 1.1 | 0.3 | 2.3 |
| 28X-3, 38–39 | Silt | 254.48 | 2.2 | 4.4 | 2.5 | 100.0 | 7.4 | 3.5 | 1.2 | * | * |
| 29X-5, 76–77 | Silt | 267.46 | 4.4 | 16.6 | 8.0 | 100.0 | 9.0 | 4.3 | 1.9 | * | * |
| 30X-5, 96–97 | Silt | 277.36 | 5.0 | 11.3 | 5.9 | 100.0 | 9.7 | * | 2.2 | * | * |
| 33X-3, 80–81 | Silt | 302.80 | 3.7 | 7.9 | 5.0 | 100.0 | 10.6 | 5.3 | 1.0 | * | * |
| 39X-1, 22–23 | Silt | 357.02 | 1.7 | 3.3 | 2.3 | 100.0 | 14.1 | 5.1 | 0.5 | 0.6 | * |
| 41X-2, 36–37 | Silt | 377.86 | 3.5 | 9.1 | 3.7 | 100.0 | 10.3 | 4.9 | 1.1 | 1.7 | 0.9 |
| 43X-6, 113–114 | Silt | 403.27 | 4.0 | 7.6 | 4.1 | 100.0 | 8.8 | 4.0 | 1.1 | * | 2.6 |
| 44X-1, 26–27 | Silt | 405.26 | 2.4 | 4.8 | 2.9 | 100.0 | 8.0 | 3.1 | 0.9 | * | 1.8 |
| 45X-3, 71–72 | Silt | 417.55 | 1.6 | 3.4 | 2.1 | 100.0 | 7.9 | 3.8 | 0.9 | * | * |

Notes: See "Lithostratigraphy" section in the "Explanatory Notes" chapter, this volume, for XRD methods. * denotes non-detection.

*G. tumida flexuosa, G. tumida,* and *G. menardii* from 319 to 357 mbsf (Samples 936A-35X-CC, 10–19 cm, through -39X-CC, 6–15 cm). The appearance of these species occurs in samples that also contain iron-stained foraminifers, rare bathyal benthic foraminifers, broken sponge spicules, and shell and wood fragments, suggesting that Subunits VA and VB contain reworked interglacial material. The occurrence and low abundance of *G. tumida flexuosa* means that the material could be from oxygen isotope Stages 5 through 11. Subunits VC and VD contain a well-preserved interglacial assemblage from 386 to 405 mbsf containing *G. tumida flexuosa, G. tumida, G. menardii,* and *P. obliquiloculata* (Samples 936A-42X-1, 67–69 cm, through -43X-CC, 54–63 cm). There is no strong evidence to suggest that these subunits were reworked. The occurrence of abundant abyssal benthic foraminifers in some of these samples suggests a much lower sedimentation rate than in the Y Zone sediment. The relatively high abundance of *G. tumida flexuosa* and the occurrence of *G. hexagonus* suggests this interval is probably from the oxygen isotope Stage 5 (X Zone) by comparison with assemblages in the eastern equatorial Atlantic. Subunit VIA and VIB from 408 to 426 mbsf also contains *G. tumida flexuosa, G. tumida, G. menardii,* and *P. obliquiloculata* (Samples 936A-44X-CC, 35–44 cm, through -45X-CC, 28–37 cm). Subunit VIA contains bathyal benthic foraminifers (see "Benthic Foraminifers" section), suggesting a reworked component, whereas Subunit VIB did not contain bathyal benthic foraminifers.

## Benthic Foraminifers

Two types of benthic foraminifers are found at Site 936 (Table 4). The first is an upper- to mid-bathyal group composed of *Bulimina marginata, Bulimina exilis, Bolivina striatula,* and *Quinqueloculina*

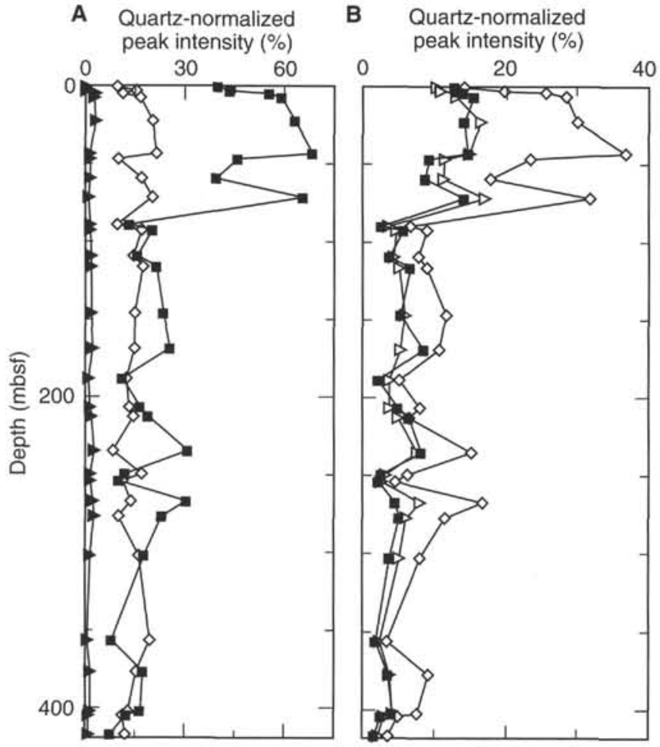


Figure 23. Relative abundance of silicate minerals based on XRD analysis of Site 936 sediment (from Table 2). See text for discussion. **A.** Squares = clay minerals + mica; diamonds = feldspar; triangles = augite + hornblende. **B.** Squares = smectite; diamonds = illite (+ mica); triangles = kaolinite.

sp. The second is a deep-water, low-oxygen abyssal group comprising *Uvigerina* spp. and *Pyrgo* spp. Abyssal benthic foraminifers are found in the Holocene section of Hole 936A. Rare abundance of bathyal benthic foraminifers found at 16 mbsf and at 26 mbsf (Samples 936A-2H-CC, 12–21 cm, and -3H-CC, 34–43 cm) suggests there was a contribution from pelagic material and material transported from above 2000 m to the sediment deposited at Site 936 in the late Y Zone. Bathyal benthic foraminifers occur in abundance in Subunit IIIA from 96.7 to 112.2 mbsf and in Unit IV from 172.2 to 286.7 mbsf, indicating, along with the evidence mentioned above (see "Planktonic Foraminifers" section), that there was significant reworking of these units. Abundant abyssal benthic foraminifers occur in Subunits VC and VD from 386.3 to 407.2 mbsf, suggesting much lower sedimentation rates in this section. Rare bathyal benthic foraminifers also sporadically occur in Subunits VC, VD, and VIA, suggesting a small reworked contribution to this sediment.

### Siliceous Microfossils

Site 936 is barren of diatoms, except for the mud-line sample where a few solution-resistant species of marine pelagic diatoms are present (Table 4). Siliceous sponge spicules are present in low abundances throughout Hole 936A.

### Palynology

Twenty-six samples were examined from Hole 936A (Table 5). In general, low abundance and moderate preservation are characteristic of most of these samples. One sample from the uppermost Unit I is barren, which is similar to samples examined from the Holocene (Z Zone) calcareous clay at most of the previous sites. A late Pleistocene (Y Zone) pollen and spore assemblage is obtained from sediment types ranging from clays, silty clays, and sandy clays (Units II, III, and IV) between 1.75 mbsf and 286.72 mbsf (Table 5; Samples 936A-1H-2, 23–25 cm, through -31X-CC, 38–39 cm) and has variable abundance with *Mauritia*, Caryophyllaceae, Gramineae, monosulcus (probably Palmae), tricolporate, tricolpate (TC), and stephanoporate (SP) pollen types, with Cyatheaceae, *Hymenophyllum*, and monolete spores present. Eight core-catcher samples were examined between 307.65 mbsf and 426.19 mbsf (Table 5). In general, the samples are barren or of low abundance and diversity, similar to the Holocene assemblage (Fig. 24). Wood particles have been observed in all sample slides in low abundance. Macroscopic wood, seed, and leaf material (>63 µm) was observed in core-catcher samples between 90.97 and 135.80 mbsf (Table 5). Five other core-catcher samples contained macroscopic organic material at 181.45 mbsf, 210.05 mbsf, 307.55 mbsf, 319.63 mbsf, and 357.73 mbsf (Table 5). Dinoflagellates are not present in the samples examined.

### Stratigraphic Summary

Unit I contains nannofossil and planktonic foraminifer assemblages indicative of the Holocene. The disappearance downcore of *G. tumida* places the boundary of the Ericson Z and Y Zone between 0.53 mbsf and 1.01 mbsf (Fig. 24). Unit I is barren of pollen and spores, which is characteristic of the Holocene (Z Zone) calcareous clay at most Leg 155 sites.

Unit II, between the Z/Y boundary and 63 mbsf has been defined as the Y Zone on the basis of the absence of *G. menardii* and *G. tumida*. It can also be constrained to younger than 40 ka due to the absence of *P. obliquiloculata*. Nannofossils are absent or very rare in this unit.

Subunit IIIA is predominantly sand and is barren of planktonic and benthic foraminifers, and has rare nannofossils. Subunit IIIB and the top of Subunit IIIC contain rare *G. ruber* as well as wood and shell fragments, and sponge spicules, suggesting that this interval is reworked. The base of Subunit IIIC has abundant foraminifers and nannofossils, and shows no evidence of reworking. The nannofossil assemblage represents Zone CN15b, suggesting the subunit is younger than 85 ka. Rare but well-preserved *P. obliquiloculata* are found 148 mbsf, suggesting that this short section is older than 40 ka.

Unit IV, a mass-transport deposit, has relatively high abundances of planktonic foraminifers and low abundances of poorly preserved nannofossils. The planktonic foraminifers indicate the sediment predates the 40-ka $Y_{P.\ obliq.}$ Zone marker. Strong evidence suggests this unit is reworked, which is consistent with its inferred origin as a mass-transport or debris-flow unit.

Subunits VA and VB contain sporadic occurrences of *G. tumida flexuosa*, *G. tumida*, and *G. menardii*, and poorly preserved nannofossil assemblages and have strong evidence of reworking.

Subunits VC and VD contain a well-preserved interglacial planktonic foraminifer assemblage, abundant abyssal benthic foraminifers, and rare *Emiliania huxleyi* referring the unit to Zone CN15a. The relatively high abundance of *G. tumida flexuosa* and the occurrence of *G. hexagonus* suggests this interval is from the highstand interglacial period that, from the nannofossils, must be equivalent to either oxygen isotopic Stage 5 or 7. Pollen and spore assemblages from Units V and VI were barren or had low abundance and moderate preservation. Subunit VIA contains a well-preserved nannofossil assemblage representing Zone CN14b (0.26–0.46 Ma). The foraminifer assemblage in Subunit VIA is an interglacial assemblage that contains *G. tumida flexuosa*, *G. tumida*, *G. menardii*, and *P. obliquiloculata*.

## PALEOMAGNETISM

### Remanence Studies

Archive-half sections from all 10 APC cores drilled in Hole 936A were measured on the pass-through cryogenic magnetometer. Only a few highly disturbed sections were not measured. Downcore twisting, as reflected by progressive westerly drift of declination, did not

**Table 3. Calcareous nannofossil and siliceous microfossil abundance data for Hole 936A.**

| Core, section, interval (cm) | Top interval (mbsf) | Bottom interval (mbsf) | Calcareous nannofossils | | | Diatoms | | Sponge spicules | Radiolarians | Ericson Zone (inferred from foraminifers) | Age (inferred from foraminifers) |
|---|---|---|---|---|---|---|---|---|---|---|---|
| | | | Abundance | Preservation | Zone | Marine | Freshwater | | | | |
| 155-936A- | | | | | | | | | | | |
| 1H-Ml, 0 | 0.00 | | a | g | CN15b | vr | b | r | vr | Z | Holocene |
| 1H-CC, 16–17 | 6.53 | 6.54 | b | — | | b | b | b | b | Y | late Pleist.? |
| 2H-CC, 21–22 | 16.28 | 16.29 | tr | — | | b | b | b | b | | |
| 3H-CC, 43–44 | 26.35 | 26.36 | b | — | | b | b | b | b | | |
| 4H-CC, 50–51 | 35.86 | 35.87 | b | — | | b | b | r | b | | |
| 6H-CC, 50–51 | 54.88 | 54.89 | b | — | | b | b | b | b | | |
| 7H-CC, 9–10 | 63.51 | 63.52 | b | — | | b | b | b | b | | |
| 8H-CC, 25–26 | 73.61 | 73.62 | b | — | | b | b | b | b | ? | ? |
| 10H-CC, 9–10 | 91.06 | 91.07 | b | — | | b | b | b | b | ? | ? |
| 11X-CC, 26–27 | 93.25 | 93.26 | b | — | | b | b | b | b | ? | ? |
| 12X-CC, 2–3 | 96.72 | 96.73 | tr | — | | b | b | b | b | ? | ? |
| 13X-CC, 26–31 | 112.26 | 112.31 | b | — | | b | b | b | b | RW | late Pleist. |
| 14X-CC, 28–29 | 117.50 | 117.51 | b | — | | b | b | b | b | RW | late Pleist. |
| 15X-CC, 11–12 | 125.91 | 125.92 | b | — | | b | b | b | b | RW | late Pleist. |
| 16X-CC, 26–27 | 135.89 | 135.90 | b | — | | b | b | b | b | RW | late Pleist. |
| 17X-2, 31 | 146.61 | | b | — | | b | b | b | b | | |
| 17X-2, 111 | 147.41 | | r | p | | b | b | b | b | | |
| 17X-3, 99 | 148.79 | | a | g | | b | b | b | b | $Y_{P. obliq.}$ | late Pleist. |
| 17X-3, 100 | 148.80 | | a | g | | b | b | b | b | | |
| 17X-3, 127 | 149.07 | | r | p | | b | b | b | b | | |
| 17X-CC, 16–17 | 150.89 | 150.90 | b | — | | | | | | Y | late Pleist. |
| 18X-1, 30 | 154.80 | | tr | — | | | | | | | |
| 18X-2, 41 | 156.41 | | b | — | | | | | | | |
| 18X-2, 82–84 | 156.82 | 156.84 | tr | — | | | | | | | |
| 18X-3, 62–65 | 158.12 | 158.15 | tr | — | | | | | | | |
| 18X-3, 70 | 158.20 | | a/rw | — | | | | | | | |
| 18X-4, 28–30 | 159.28 | 159.30 | r | — | | | | | | | |
| 18X-4, 77–80 | 159.77 | 159.80 | vr | — | | | | | | | |
| 18X-4, 98–100 | 159.98 | 160.00 | vr | — | | | | | | | |
| 18X-5, 56–58 | 161.06 | 161.08 | vr | — | | | | | | | |
| 18X-5, 136–139 | 161.86 | 161.89 | vr | — | | | | | | | |
| 18X-CC, 37–38 | 164.02 | 164.03 | b | — | | b | b | b | b | RW | late Pleist. |
| 19X-1, 18–19 | 164.28 | 164.29 | tr | — | | | | | | | |
| 19X-4, 18–19 | 168.78 | 168.79 | f | — | | | | | | | |
| 19X-5, 56–58 | 170.66 | 170.68 | tr | — | | | | | | | |
| 19X-6, 18–19 | 171.78 | 171.79 | r | — | | | | | | | |
| 19X-CC, 27–28 | 172.34 | 172.35 | vr | — | CN15a? | | | | | RW | late Pleist. |
| 20X-1, 93 | 173.81 | | tr | — | | | | | | | |
| 20X-2, 93 | 176.23 | | r | — | | | | | | | |
| 20X-5, 39–41 | 180.19 | 180.21 | b | — | | | | | | | |
| 20X-CC, 35–36 | 181.54 | 181.55 | b | — | | | | | | RW | late Pleist. |
| 21X-2, 46–48 | 185.36 | 185.38 | b | — | | | | | | | |
| 21X-3, 65–67 | 187.05 | 187.07 | b | — | | | | | | | |
| 21X-5, 65–67 | 190.05 | 190.07 | b | — | | | | | | | |
| 21X-CC, 16–17 | 191.29 | 191.30 | vr | — | | b | b | r | b | RW | late Pleist. |
| 22X-CC, 20–21 | 199.78 | 199.79 | tr | — | | b | b | f | b | RW | late Pleist. |
| 23X-3, 30–32 | 206.10 | 206.12 | b | — | | b | b | r | b | RW | late Pleist. |
| 23X-4, 35–37 | 206.15 | 206.17 | tr | — | | b | b | r | b | | |
| 23X-CC, 31–32 | 210.14 | 210.15 | tr | — | | b | b | b | b | RW | late Pleist. |
| 24X-CC, 76–77 | 220.76 | 220.77 | b | — | | b | b | b | b | RW | late Pleist. |
| 25X-3, 144–148 | 226.54 | 226.58 | b | — | | b | b | r | b | | |
| 25X-4, 143–148 | 228.03 | 228.08 | b | — | | b | b | r | b | | |
| 25X-CC, 41–42 | 229.77 | 229.78 | tr | — | | b | b | r | b | RW | late Pleist. |
| 26X-CC, 41–42 | 241.51 | 241.52 | b | — | | b | b | r | b | RW | late Pleist. |
| 27X-CC, 24–25 | 251.57 | 251.58 | tr | — | | b | b | b | b | RW | late Pleist. |
| 28X-CC, 19–20 | 259.59 | 259.60 | b | — | | b | b | b | b | RW | late Pleist. |
| 29X-CC, 35–36 | 268.46 | 268.47 | b | — | | b | b | b | b | RW | late Pleist. |
| 30X-CC, 44–45 | 279.11 | 279.12 | tr | — | | b | b | r | b | RW | late Pleist. |
| 31X-CC, 38–39 | 286.72 | 286.73 | b | — | | b | b | r | b | RW | late Pleist. |
| 32X-CC, 32–33 | 299.11 | 299.12 | tr | — | | | | | | ? | |
| 33X-CC, 29–30 | 307.64 | 307.65 | vr | — | | | | | | ? | |
| 34X-CC, 0 | 318.20 | | tr | — | | | | | | ? | |
| 36X-CC, 2–3 | 327.92 | 327.93 | r | — | | b | b | r | b | (RW)? | m.-l. Pleist. |
| 37X-CC, 2–3 | 337.52 | 337.53 | vr | — | | | | | | (RW)? | m.-l. Pleist. |
| 39X-CC, 15–16 | 357.82 | 357.83 | b | — | | b | b | b | b | (RW)? | m.-l. Pleist. |
| 41X-4, 77–79 | 381.27 | 381.29 | b | — | | | | | | ? | |
| 41X-CC, 18–19 | 382.18 | 382.19 | b | — | | b | b | b | b | ? | |
| 42X-1, 17 | 385.87 | | b | — | | | | | | ? | m.-l. Pleist. |
| 42X-1, 67–69 | 385.37 | 385.39 | a | — | CN15a | | | | | ? | m.-l. Pleist. |
| 42X-1, 113–115 | 386.83 | 386.85 | a | — | | | | | | | |
| 42X-1, 125–130 | 386.95 | 386.00 | a | g | | | | | | | |
| 42X-1, 131–134 | 387.01 | 387.04 | a | g | | | | | | | |
| 42X-2, 4–6 | 387.24 | 387.26 | f | g | | | | | | | |
| 42X-2, 70–72 | 387.90 | 387.92 | c | g | | | | | | | |
| 42X-2, 98–100 | 388.18 | 388.20 | f | g | | | | | | | |
| 42X-2, 106–108 | 388.26 | 388.28 | a | g | | | | | | | |
| 42X-2, 113–115 | 388.33 | 388.35 | a | g | | | | | | ? | m.-l. Pleist. |
| 42X-CC, 8–17 | 388.70 | 388.79 | r | p | | | | | | ? | m.-l. Pleist. |
| 43X-1, 3–7 | 395.33 | 395.37 | vr | — | | | | | | | |
| 43X-1, 63–67 | 395.93 | 395.97 | vr | — | | | | | | | |
| 43X-2, 6–10 | 396.20 | 396.24 | b | — | | | | | | | |
| 43X-2, 81–86 | 396.95 | 397.00 | vr | — | | | | | | | |
| 43X-2, 148–150 | 397.62 | 397.64 | vr | — | | | | | | | |
| 43X-3, 6–10 | 397.70 | 397.74 | tr | — | | | | | | | |
| 43X-3, 57–61 | 398.21 | 398.25 | b | — | | | | | | | |
| 43X-3, 143–146 | 399.07 | 399.10 | c | g | | | | | | | |
| 43X-4, 2–5 | 399.16 | 399.19 | r | m | | | | | | | |

Table 3 (continued).

| Core, section, interval (cm) | Top interval (mbsf) | Bottom interval (mbsf) | Calcareous nannofossils Abundance | Preservation | Zone | Diatoms Marine | Freshwater | Sponge spicules | Radiolarians | Ericson Zone (inferred from foraminifers) | Age (inferred from foraminifers) |
|---|---|---|---|---|---|---|---|---|---|---|---|
| 43X-4, 135–138 | 400.49 | 400.52 | f | g | | | | | | | |
| 43X-5, 37–40 | 400.97 | 401.00 | f | g | | | | | | | |
| 43X-5, 94–98 | 401.58 | 401.62 | b | — | | | | | | | |
| 43X-6, 81–85 | 402.95 | 402.99 | c | g | | | | | | | |
| 43X-7, 79–81 | 404.43 | 404.45 | f | g | | | | | | | |
| 43X-CC, 54–63 | 405.39 | 405.48 | c | g | | | | | | ? (RW) | m.-l. Pleist. |
| 44X-1, 55–58 | 405.55 | 405.58 | f | g | | | | | | | |
| 44X-1, 76–78 | 405.76 | 405.78 | a | g | CN14b | | | | | | |
| 44X-1, 127–130 | 406.27 | 406.30 | c | g | | | | | | | |
| 44X-2, 13–16 | 406.63 | 406.66 | a | g | | | | | | | |
| 44X-2, 54–57 | 407.04 | 407.07 | c | g | | | | | | | |
| 44X-2, 81–84 | 407.31 | 407.34 | f | g | | | | | | | |
| 44X-2, 141–143 | 407.91 | 407.93 | c | g | | | | | | | |
| 44X-3, 3–6 | 408.03 | 408.06 | f | g | | | | | | | |
| 44X-CC, 35–44 | 408.58 | 408.67 | a | g | | | | | | ? (RW) | m.-l. Pleist. |
| 45X-1, 64–66 | 415.24 | 415.26 | tr | — | | | | | | | |
| 45X-2, 10–12 | 415.44 | 415.46 | b | — | | | | | | | |
| 45X-2, 56–58 | 415.90 | 415.92 | b | — | | | | | | | |
| 45X-2, 135–137 | 416.69 | 416.71 | b | — | | | | | | | |
| 45X-CC, 33–42 | 422.95 | 423.04 | tr | — | | | | | | ? | m.-l. Pleist. |
| 45X-3, 56–58 | 417.40 | 417.42 | b | — | | | | | | | |
| 46X-CC, 37–38 | 426.19 | 426.20 | b | — | | b | b | b | b | ? | m.-l. Pleist. |

appear as a notable effect, except for Cores 936A-6H and -7H. The Tensor tool provided azimuthal orientations for Cores 936A-3H through -10H. The corrected declinations at the top of each oriented core were near 0°, except for Core 936A-5H, whose declinations were ~310° throughout the core.

Selected sections from 27 of the 36 XCB cores were also measured on the cryogenic magnetometer. For these cores, the declinations were strongly biased toward ~30°, and their inclinations remained high (20° to 50°), even after AF demagnetization to 20 mT. Again pervasive and persistent drill stem remanence appears to have seriously degraded the archive-half measurements of the XCB cores. Test AF demagnetizations of discrete samples to levels >20 mT appeared to be more successful in removing this secondary component.

An apparent geomagnetic excursion was identified in Section 936A-7H-6, from 60.5 to 61.5 mbsf, within an undisturbed interval of dark silty clay. The feature had the same general form as those in the previous holes (i.e., a rapid shift of inclination from moderately negative to high positive inclinations downhole, with an intensity peak corresponding to the maximum in positive inclination). However, high field AF demagnetization of discrete samples from this anomalous interval resulted in inclinations that stabilized at low values. Therefore, the feature appears to have resulted from incomplete removal of drill-stem remanence before the pass-through measurements. Hence, the feature does not represent a geomagnetic excursion.

A 2-m zone of undisturbed silty clay from Core 936A-8H contains eight oscillations in declination, inclination, and intensity (Fig. 25).

### Magnetic Susceptibility

Whole-core and discrete-sample susceptibilities, measured on all cores from Hole 936A, show similar downhole trends (Fig. 26). The highest values are associated with Subunits IIIA and IIIC. The lowest values are within Unit II. There is a clear increase in susceptibility across the Unit II/Unit III boundary (about 73 mbsf). Whole-core susceptibility values then decrease across the Unit III/Unit IV boundary and increase again across the Unit IV/Unit V boundary. These results suggest a relationship between the measured susceptibility and sediment type at this site.

The discrete sample data show a spike at about 400 mbsf that is associated with dark, coarse-grained banding in Core 936A-43X. The pass-through magnetometer data indicated a remanence peak (~20 times higher than background remanence intensity) associated with this and other dark sandy bands in the bottom cores of Hole 936A.

## ORGANIC GEOCHEMISTRY

### Volatile Hydrocarbons

Headspace methane concentrations in Hole 936A are moderately high throughout the core. The concentrations range from ~5500 ppm to ~18500 ppm with a lower value (~970 ppm) at 356.80 mbsf in a predominantly sandy interval. The highest methane concentration (18,561 ppm) was measured near the bottom of the hole (424.20 mbsf; Table 6; Fig. 27). Vacutainer methane values are as much as two orders of magnitude higher than headspace concentrations (Fig. 27), ranging from 113,000 ppm to 804,000 ppm in Hole 936A. The maximum concentration (804,000 ppm) was detected at 31.50 mbsf. Higher molecular weight hydrocarbons were not observed, indicating a predominantly biogenic methane source at Site 936.

### Carbon, Nitrogen, and Sulfur Concentrations

The carbonate content, calculated as $CaCO_3$, is 42% at 0.10 mbsf, decreases to 5.8% at 0.75 mbsf, and ranges from 0% to 4.2% between 3.60 and 381 mbsf (Table 7; Fig. 28). Below 381 mbsf, higher carbonate values were measured in several samples, including 22.4% in a clast at 388.26 mbsf and 32.2% in a clast at 388.32 mbsf. Below 388.32 mbsf, carbonate content ranges from 2.2% to 6.7%. TOC is low (~0.5%) in the two shallowest samples (0.27 and 0.75 mbsf) and increases to 1.24% at 15.91 mbsf. From 15.91 to 381 mbsf, TOC values steadily decrease to between 0.8% and 0.9% at the top of lithologic Unit V. Exceptions are low concentrations, ranging from 0.7% to 0.1%, measured in silt and sand layers and in carbonate-rich zones in hemipelagic clays. Below 381 mbsf, TOC concentrations vary from 0.18% to 1.42% and correspond to various lithologic changes. The lowest concentration (0.18%) was measured in a sample taken in a black clast containing high amounts of sulfide and with a TS concentration of 8%.

Most TN concentrations in Hole 936A range from 0.11% to 0.14% down to the top of lithologic Unit V, at 305.84 mbsf. Below 381 mbsf, TN concentrations show a high variability similar to the TOC profile in this interval.

TS concentrations range from 0% to 0.5%, increasing slightly downhole. Elevated concentrations, from 0.8% to 1.84%, were mea-

**Table 4. Foraminifer abundance data for Hole 936A.**

| Core, section, interval (cm) | Top interval (mbsf) | Bottom interval (mbsf) | *Globorotalia menardii* | *Globorotalia tumida* | *Globorotalia tumida flexuosa* | *Pulleniatina obliquiloculata* | *Globigerinoides ruber* (white) | *Globigerinoides ruber* (pink) | *Globorotalia hexagonus* | *Neogloboquadrina dutertrei* | *Globorotalia trilobus trilobus* | *Globorotalia inflata* | *Globorotalia truncatulinoides* | *Globigerina bulloides* | *Globigerinoides trilobus sacculifer* | *Globorotalia fimbriata* | *Bolliella adamsi* | *Hastigerinella digitata* | *Globigerina calida calida* | *Globorotalia crassaformis hessi* | *Globorotalia crassaformis viola* | *Globorotalia tosaensis* | *Globorotalia crassaformis crassaformis* | Other planktonic foraminifers | Vivianite nodules | Overall foraminifer abundance | Preservation |
|---|---|---|---|---|---|---|---|---|---|---|---|---|---|---|---|---|---|---|---|---|---|---|---|---|---|---|---|
| 155-936A- | | | | | | | | | | | | | | | | | | | | | | | | | | | |
| 1H-1, 20–22 | 0.20 | 0.22 | F | F | B | F | C | F | F | C | C | R | F | B | F | F | B | B | B | R | B | B | B | B | B | A | G |
| 1H-1, 43–45 | 0.43 | 0.45 | F | F | B | F | C | R | B | C | C | B | R | B | F | B | B | B | B | B | B | B | B | B | B | A | G |
| 1H-1, 52–54 | 0.52 | 0.54 | R | F | B | F | C | R | B | F | F | B | R | B | F | R | B | B | B | B | B | B | B | B | B | C | M |
| 1H-1, 100–102 | 1.00 | 1.02 | B | B | B | F | C | F | B | F | F | B | R | B | R | B | B | B | B | B | B | B | B | B | B | F | M |
| 1H-CC, 7–16 | 6.44 | 6.53 | R | R | B | B | F | R | B | C | C | B | R | B | C | R | B | B | B | B | B | B | B | B | C | R | M |
| 2H-CC, 12–21 | 16.29 | 16.38 | B | B | B | B | F | B | C | C | B | B | B | B | C | B | B | B | B | B | B | B | B | B | A | R | M |
| 3H-CC, 34–43 | 26.26 | 26.35 | B | B | B | B | F | B | B | C | C | B | B | B | C | B | B | B | B | B | B | B | B | B | A | R | M |
| 4H-CC, 41–50 | 35.77 | 35.86 | B | B | B | B | F | F | B | A | C | B | B | B | B | B | B | B | R | B | B | B | B | B | C | R | G |
| 5H-CC, 40–49 | 45.29 | 45.38 | B | B | B | B | B | B | B | B | B | B | B | B | B | B | B | B | B | B | B | B | B | B | A | B | B |
| 6H-CC, 41–50 | 54.79 | 54.88 | B | B | B | B | B | B | B | C | C | B | B | B | A | B | B | B | B | B | B | B | B | B | A | F | G |
| 7H-CC, 1–9 | 63.42 | 63.51 | B | B | B | B | C | B | B | C | C | B | F | B | B | B | B | B | B | B | B | B | B | B | A | R | G |
| 8H-CC, 16–25 | 73.52 | 73.61 | B | B | B | B | B | B | B | B | B | B | B | B | B | B | B | B | B | B | B | B | B | B | B | B | B |
| 9H-CC, 0–9 | 75.37 | 75.46 | B | B | B | B | B | B | B | B | B | B | B | B | B | B | B | B | B | B | B | B | B | B | B | B | B |
| 10H-CC, 1–9 | 90.97 | 91.06 | B | B | B | B | B | B | B | B | B | B | B | B | B | B | B | B | B | B | B | B | B | B | F | B | B |
| 11X-CC, 17–26 | 93.16 | 93.25 | B | B | B | B | B | B | B | B | B | B | B | B | B | B | B | B | B | B | B | B | B | B | R | B | B |
| 12X-CC, 0–2 | 96.70 | 96.72 | B | B | B | B | R | B | R | B | B | B | B | B | B | B | B | B | B | B | B | B | B | B | R | R | G |
| 13X-CC, 0–4 | 112.26 | 112.30 | B | B | B | B | R | B | B | B | B | B | B | B | B | B | B | B | B | B | B | B | B | B | R | R | M |
| 14X-CC, 19–28 | 117.41 | 117.50 | B | B | B | B | B | B | B | B | B | B | B | B | B | B | B | B | B | B | B | B | B | B | B | B | B |
| 15X-CC, 2–11 | 125.82 | 125.91 | B | B | B | B | B | B | B | B | B | B | B | B | B | B | B | B | B | B | B | B | B | B | B | B | B |
| 16X-CC, 17–26 | 135.80 | 135.89 | B | B | B | B | B | B | B | B | R | B | B | B | B | B | B | B | B | B | B | B | B | B | R | B | M |
| 17X-3, 99–104 | 148.79 | 148.84 | B | F | B | R | C | B | B | F | F | R | B | B | F | B | B | B | R | B | B | B | B | B | B | A | G |
| 17X-CC, 7–16 | 150.80 | 150.89 | B | B | B | B | C | R | B | C | C | B | C | B | C | B | B | B | R | B | B | B | B | B | R | C | G |
| 18X-CC, 28–37 | 163.93 | 164.02 | B | B | B | B | C | F | B | C | C | B | C | B | C | B | B | B | B | B | B | B | B | B | C | C | G |
| 19X-CC, 18–27 | 172.25 | 172.34 | B | B | B | C | F | R | B | C | C | B | C | B | C | B | B | B | B | B | B | B | B | B | C | C | M |
| 20X-CC, 26–35 | 181.45 | 181.54 | B | B | B | C | C | B | B | C | F | B | C | B | R | B | B | B | B | B | B | B | B | B | C | F | M |
| 21X-CC, 7–16 | 191.20 | 191.29 | B | B | B | C | F | R | B | C | F | B | A | B | B | B | B | B | B | B | B | B | B | B | C | R | M |
| 22X-CC, 11–20 | 199.69 | 199.78 | B | B | B | C | C | B | B | C | B | B | C | B | B | B | B | B | B | B | B | B | B | B | A | F | M |
| 23X-CC, 22–31 | 210.05 | 210.14 | B | B | B | R | C | B | B | C | F | B | F | B | F | B | B | B | B | B | B | B | B | B | F | F | M |
| 24X-CC, 67–76 | 220.67 | 220.76 | B | B | B | F | R | B | B | R | F | B | F | B | R | B | B | B | B | B | B | B | B | B | A | F | B |
| 25X-CC, 32–41 | 229.68 | 229.77 | B | B | B | B | F | B | B | R | F | B | B | B | R | B | B | B | B | B | B | B | B | B | A | F | M |
| 26X-CC, 32–41 | 241.42 | 241.51 | B | B | B | R | F | B | B | F | F | B | F | B | R | B | B | B | B | B | B | B | B | B | F | C | M |
| 27X-CC, 15–24 | 251.49 | 251.58 | B | B | B | C | R | R | B | C | C | B | B | B | F | B | B | B | B | B | B | B | B | B | B | F | M |
| 28X-CC, 10–19 | 259.50 | 259.59 | B | B | B | C | F | B | B | C | B | B | C | B | R | B | B | B | B | B | B | B | B | B | F | R | M |
| 29X-CC, 26–35 | 268.37 | 268.46 | B | B | B | R | F | B | B | C | C | B | C | B | F | B | B | B | B | B | B | B | B | B | A | F | G |
| 30X-CC, 35–44 | 279.02 | 279.11 | B | B | B | F | F | B | B | C | C | B | C | B | R | B | B | B | B | B | B | B | B | B | B | F | G |
| 31X-CC, 29–38 | 286.63 | 286.72 | B | B | B | F | C | R | B | C | C | B | C | B | F | B | B | B | B | B | B | B | B | B | A | C | G |
| 32X-CC, 23–32 | 299.02 | 299.11 | B | B | B | B | B | B | B | B | B | B | B | B | B | B | B | B | B | B | B | B | B | B | A | B | B |
| 33X-CC, 20–29 | 307.55 | 307.64 | B | B | B | B | B | B | B | B | B | B | B | B | B | B | B | B | B | B | B | B | B | B | F | B | B |
| 35X-CC, 10–19 | 319.63 | 319.72 | B | B | R | R | B | B | B | R | R | B | B | B | B | B | B | B | B | B | B | B | B | B | F | R | M |
| 36X-CC, 0–2 | 327.90 | 327.92 | B | B | B | B | B | B | B | B | B | B | B | B | B | B | B | B | B | B | B | B | B | B | R | B | B |
| 38X-CC, 0–1 | 347.20 | 347.21 | B | B | B | B | B | B | B | B | B | B | B | B | B | B | B | B | B | B | B | B | B | B | R | B | B |
| 39X-CC, 6–15 | 357.73 | 357.82 | R | F | R | R | R | B | B | R | R | B | R | B | B | B | B | B | B | B | B | B | B | B | R | R | P |
| 41X-CC, 9–18 | 382.09 | 382.18 | B | R | B | B | R | B | B | B | B | B | B | B | B | B | B | B | B | B | B | B | B | B | F | R | G |
| 42X-1, 67–69 | 386.37 | 386.39 | B | F | B | C | C | R | B | C | F | B | B | B | B | B | B | B | B | B | B | B | B | B | B | C | G |
| 42X-2, 113–115 | 388.33 | 388.35 | C | C | F | F | C | B | R | C | C | B | C | B | B | B | B | B | B | B | B | B | B | B | B | A | G |
| 42X-CC, 8–17 | 388.70 | 388.79 | F | F | R | F | C | B | B | F | F | R | F | B | F | B | B | B | B | B | B | B | B | B | F | F | G |
| 43X-3, 67–69 | 398.31 | 398.33 | F | C | B | C | C | B | B | C | R | B | B | B | R | B | B | B | B | B | B | B | B | B | C | R | M |
| 43X-CC, 54–63 | 405.39 | 405.48 | R | F | B | B | C | B | B | F | C | B | R | B | R | B | B | B | B | B | B | B | B | B | R | F | G |
| 44X-2, 76–78 | 407.26 | 407.28 | F | F | F | B | F | B | R | C | C | B | C | B | C | B | B | B | B | B | B | B | R | B | B | A | M |
| 44X-CC, 35–44 | 408.58 | 408.67 | B | C | F | F | F | B | R | F | B | B | B | B | B | B | B | B | B | F | B | B | B | B | B | A | P |
| 45X-CC, 33–42 | 422.95 | 423.04 | B | F | R | F | C | B | B | F | C | B | B | B | B | B | B | B | B | R | B | B | B | B | F | C | M |
| 46X-CC, 28–37 | 426.10 | 426.19 | B | R | B | B | R | B | B | R | B | B | B | B | B | B | B | B | B | B | B | B | B | B | F | R | P |

Notes: Key to Comments section: Sediment composition: S = sand, M = mica, BN = black nodules, IN = iron nodules, AM = authigenic minerals; indicators of reworking: SF = shell fragments, W = wood fragments, SP = spicules, IS = iron-stained foraminifers. Note also the occurrence of bathyal benthic foraminifers.

sured in intervals enriched in iron sulfides at 3.60, 155.19, 155.21, 239.49, and 387.52 mbsf.

The majority of the [C/N]a ratios range from 6 to 11 and decrease slightly to a depth of 305.84 mbsf. Below 381 mbsf the ratios vary more widely, from 5 to 23. The high variability is characteristic of this interval (381 to 424.77 mbsf) and is consistent with the high lithologic variability.

### *Bitumen Characterization*

Five samples (0.27, 15.91, 44.87, 92.26, and 387.52 mbsf) were extracted with *n*-hexane for preliminary characterization of the extractable organic matter by gas chromatography. Two representative gas chromatograms (Samples 936A-6H-1, 37–38 cm [44.87 mbsf], and 936A-42X-2, 32–33 cm [387.52 mbsf]) are shown in Figure 29. The *n*-alkanes were identified by comparison of their retention times with those of standards.

All five samples shallower than 100 mbsf show similar *n*-alkane distributions, with a predominance of odd-carbon numbers and *n*-$C_{29}H_{60}$ as the major *n*-alkane. This predominance is especially marked in the three samples of late Pleistocene age (15.91, 44.87, and 92.26 mbsf) as reflected in the high $CPI_{25-33}$ values (Bray and Evans, 1961; see "Explanatory Notes" chapter, this volume) of 5.4 in each of these samples. These *n*-alkane distribution patterns are typical of cuticular waxes from higher land plants (e.g., Tissot and Welte, 1984). In these three samples, *n*-alkanes are the major components of the gas

Table 4 (continued).

| Core, section, interval (cm) | Top interval (mbsf) | Bottom interval (mbsf) | Abundance of bathyal benthic foraminifers | Abundance of abyssal benthic foraminifers | Comments | Ericson Zone | Age |
|---|---|---|---|---|---|---|---|
| 155-936A- | | | | | | | |
| 1H-1, 20–22 | 0.20 | 0.22 | R | B | | Z | Holocene |
| 1H-1, 43–45 | 0.43 | 0.45 | B | B | | Z | Holocene |
| 1H-1, 52–54 | 0.52 | 0.54 | R | B | | Z | Holocene |
| 1H-1, 100–102 | 1.00 | 1.02 | B | B | S | Y | late Pleist. |
| 1H-CC, 7–16 | 6.44 | 6.53 | B | B | | Y | late Pleist. |
| 2H-CC, 12–21 | 16.29 | 16.38 | B | R | | Y | late Pleist. |
| 3H-CC, 34–43 | 26.26 | 26.35 | B | R | S | Y | late Pleist. |
| 4H-CC, 41–50 | 35.77 | 35.86 | B | B | | Y | late Pleist. |
| 5H-CC, 40–49 | 45.29 | 45.38 | B | B | | Y | late Pleist. |
| 6H-CC, 41–50 | 54.79 | 54.88 | B | B | | Y | late Pleist. |
| 7H-CC, 1–9 | 63.42 | 63.51 | B | B | M | Y | late Pleist. |
| 8H-CC, 16–25 | 73.52 | 73.61 | B | B | S | ? | ? |
| 9H-CC, 0–9 | 75.37 | 75.46 | B | B | S | ? | ? |
| 10H-CC, 1–9 | 90.97 | 91.06 | B | B | S,M | ? | ? |
| 11X-CC, 17–26 | 93.16 | 93.25 | B | B | S,W | ? | ? |
| 12X-CC, 0–2 | 96.70 | 96.72 | R | B | S,W,SF | RW | late Pleist. |
| 13X-CC, 0–4 | 112.26 | 112.30 | R | B | S,W,M | RW | late Pleist. |
| 14X-CC, 19–28 | 117.41 | 117.50 | B | B | S | RW | late Pleist. |
| 15X-CC, 2–11 | 125.82 | 125.91 | B | B | S,W | RW | late Pleist. |
| 16X-CC, 17–26 | 135.80 | 135.89 | B | B | S,W,SP | RW | late Pleist. |
| 17X-3, 99–104 | 148.79 | 148.84 | B | F | F | $Y_{P. obliq.}$ | late Pleist. |
| 17X-CC, 7–16 | 150.80 | 150.89 | B | R | | Y | late Pleist. |
| 18X-CC, 28–37 | 163.93 | 164.02 | R | B | SP, IS | RW | late Pleist. |
| 19X-CC, 18–27 | 172.25 | 172.34 | C | B | | RW | late Pleist. |
| 20X-CC, 26–35 | 181.45 | 181.54 | F | B | W,SP,IS | RW | late Pleist. |
| 21X-CC, 7–16 | 191.20 | 191.29 | R | B | BN,SP | RW | late Pleist. |
| 22X-CC, 11–20 | 199.69 | 199.78 | F | B | SP,BN | RW | late Pleist. |
| 23X-CC, 22–31 | 210.05 | 210.14 | B | B | IS | RW | late Pleist. |
| 24X-CC, 67–76 | 220.67 | 220.76 | A | B | SP | RW | late Pleist. |
| 25X-CC, 32–41 | 229.68 | 229.77 | A | B | IS,SF,SP | RW | late Pleist. |
| 26X-CC, 32–41 | 241.42 | 241.51 | A | B | IS,SP,SF | RW | late Pleist. |
| 27X-CC, 15–24 | 251.49 | 251.58 | C | R | IS,SP | RW | late Pleist. |
| 28X-CC, 10–19 | 259.50 | 259.59 | B | B | IS,IN | RW | late Pleist. |
| 29X-CC, 26–35 | 268.37 | 268.46 | R | B | IS | RW | late Pleist. |
| 30X-CC, 35–44 | 279.02 | 279.11 | F | R | SP | RW | late Pleist. |
| 31X-CC, 29–38 | 286.63 | 286.72 | F | B | SP | RW | late Pleist. |
| 32X-CC, 23–32 | 299.02 | 299.11 | B | B | | ? | ? |
| 33X-CC, 20–29 | 307.55 | 307.64 | B | B | M,W | ? | ? |
| 35X-CC, 10–19 | 319.63 | 319.72 | R | B | IS,W,S | (RW) ? | m.-l. Pleist. |
| 36X-CC, 0–2 | 327.90 | 327.92 | B | B | S | (RW) ? | m.-l. Pleist. |
| 38X-CC, 0–1 | 347.20 | 347.21 | B | B | S | (RW) ? | m.-l. Pleist. |
| 39X-CC, 6–15 | 357.73 | 357.82 | R | B | IS,S,W,SF,SP | (RW) ? | m.-l. Pleist. |
| 41X-CC, 9–18 | 382.09 | 382.18 | R | B | S | ? | m.-l. Pleist. |
| 42X-1, 67–69 | 386.37 | 386.39 | B | C | S,SP | ? | m.-l. Pleist. |
| 42X-2, 113–115 | 388.33 | 388.35 | B | B | | ? | m.-l. Pleist. |
| 42X-CC, 8–17 | 388.70 | 388.79 | B | B | BN,AM | ? | m.-l. Pleist. |
| 43X-3, 67–69 | 398.31 | 398.33 | B | R | IS | ? | m.-l. Pleist. |
| 43X-CC, 54–63 | 405.39 | 405.48 | R | R | S | (RW) ? | m.-l. Pleist. |
| 44X-2, 76–78 | 407.26 | 407.28 | B | C | | ? | m.-l. Pleist. |
| 44X-CC, 35–44 | 408.58 | 408.67 | F | B | | (RW) ? | m.-l. Pleist. |
| 45X-CC, 33–42 | 422.95 | 423.04 | B | B | | ? | m.-l. Pleist. |
| 46X-CC, 28–37 | 426.10 | 426.19 | B | B | Broken tests | ? | m.-l. Pleist. |

chromatogram. In contrast, the Holocene sample at 0.27 mbsf shows lower amounts of odd-numbered *n*-alkanes, which are present only in trace amounts, and a $CPI_{25-33}$ value of 2.4. This difference in distribution pattern might be due to reduced terrigenous input.

The sulfide-rich sample, taken in a black clast from the debris flow (387.52 mbsf), shows a different gas chromatogram. The *n*-alkane distribution shows a lower predominance of odd-carbon-numbered *n*-alkanes with a $CPI_{25-33}$ value of 2.8. In contrast to previously described extracts, *n*-nonacosane ($C_{29}$) and *n*-hentriacontane ($C_{31}$) show similar concentrations. An interesting feature of this chromatogram is a group of at least five peaks that elute between *n*-$C_{17}H_{36}$ and *n*-$C_{19}H_{40}$ and represent the major components of this extract (Fig. 29B). Identification of these unknown compounds will require detailed studies of their molecular composition with coupled gas chromatography/mass spectrometry.

## INORGANIC GEOCHEMISTRY

### Interstitial Water Analyses

Interstitial water samples were collected from 15 sediment samples at Hole 936A. Samples were taken approximately every 10 m for

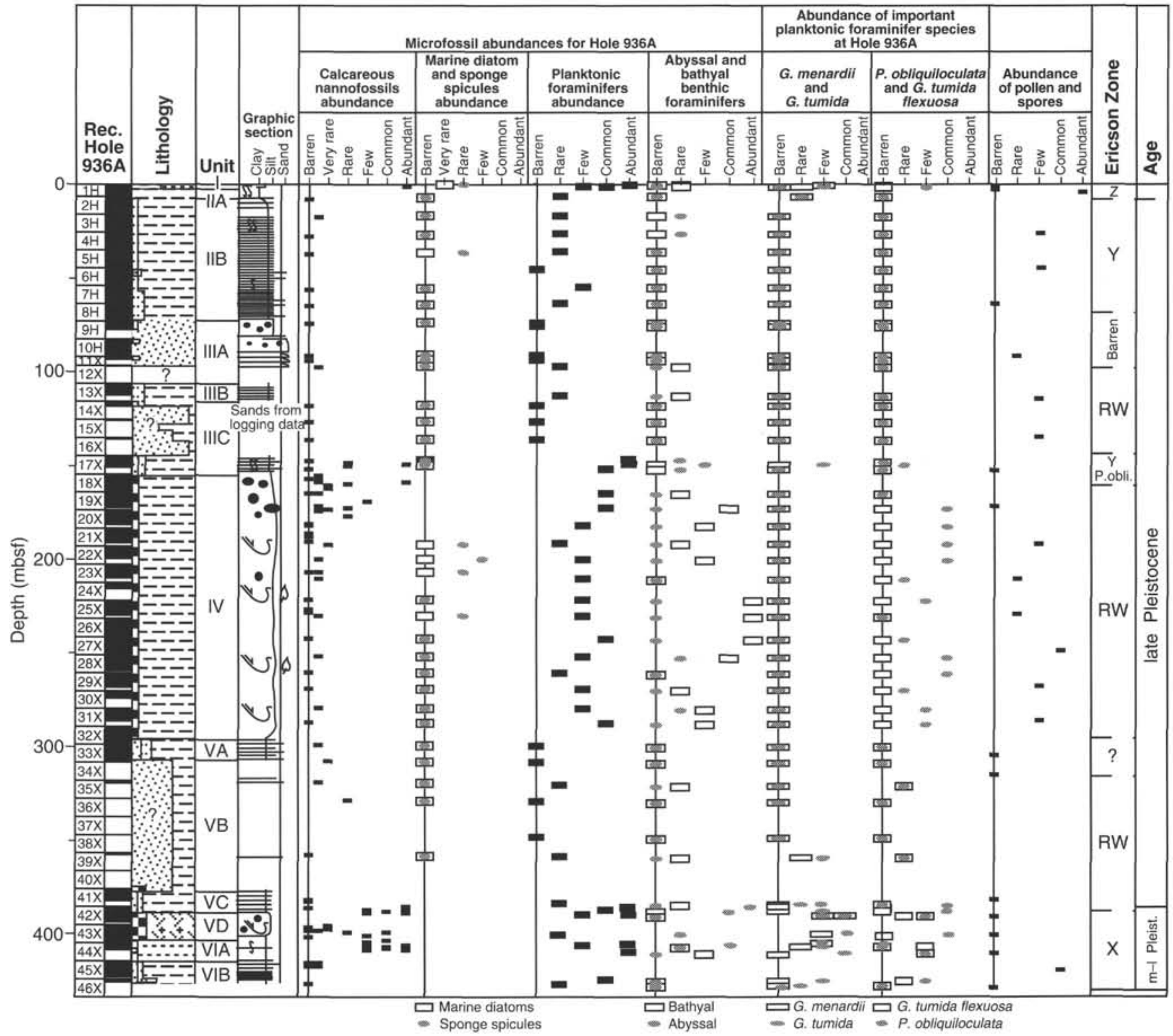

Figure 24. Biostratigraphic summary for Site 936.

the upper 40 mbsf and approximately every 30 m thereafter to a depth of 406.85 mbsf, though poor core recovery led to a sampling gap of 85 m from 295.25 to 380.35 mbsf (Table 8; Fig. 30).

Salinities of the water samples range from 32.0 to 34.0 (Fig. 30A). In the upper 24.95 m of the hole, salinity varies from 34.0 to 32.0. Below 24.95 mbsf, salinity is relatively constant, ranging from 32.0 to 33.0.

Chloride concentrations increase steadily in the upper 42.40 m of the core, from 553 at 1.45 mbsf to 564 mM at 42.40 mbsf (Fig. 30B). Chloride values then decrease more slowly to 555 mM at 208.65 mbsf. An anomalously low concentration, 547 mM, was found at 266.55 mbsf. Samples from above and below this depth have concentrations of 558 mM (239.05 mbsf) and 556 mM (295.25 mbsf). In the lowermost sample of the hole, chloride increases again to 562 mM.

Pore-water pH decreases from 7.71 at 1.45 mbsf to 7.30 at 32.90 mbsf (Fig. 30C). The values then increase downhole to 7.71 at 149.20 mbsf. The pH is relatively constant, around 7.6 from 178.20 to 295.25 mbsf, and increases slightly to around 7.8 in the two lowermost samples.

Alkalinity varies from 4.59 to 15.90 mM (Fig. 30D), with no overall trend downhole. No shallow maximum in alkalinity was observed. Below 42.40 mbsf, alkalinity is relatively constant around 10 mM, with the exception of the sample at 149.20 mbsf, which has 15.90 mM of alkalinity.

As observed at all previous sites, dissolved magnesium and calcium concentrations decrease quickly over the first few meters of the hole. Values decrease from seawater concentrations to around 40 and 5 mM, respectively, by 15.45 mbsf (Fig. 30E and 30F). Below 15.45 mbsf, the values are relatively constant. Magnesium concentrations, however, decrease slightly downhole to values as low as 32.7 mM at 380.35 mbsf.

Pore-water sulfate concentrations decrease from 18.1 mM at 1.45 mbsf to zero by 15.45 mbsf (Fig. 30G). Most of the values are within analytical uncertainty of zero for most of the remainder of the hole. Above-zero values, however, were measured in samples from 149.20, 178.20, and 295.25 mbsf. These are probably sampling artifacts.

**Table 5. Spores and pollen data for Hole 936A.**

| Core, section, interval (cm) | Top interval (mbsf) | Bottom interval (mbsf) | Pollen and spores: Abundance | Preservation | Major types recorded | Dinocysts | Wood/carbonized particles | Ericson Zone (inferred from forams.) | Age (inferred from forams.) |
|---|---|---|---|---|---|---|---|---|---|
| 155-936A- | | | | | | | | | |
| 1H-1, 43–45 | 0.43 | 0.45 | b | | | b | f | Z | Holocene |
| 1H-2, 23–25 | 1.73 | 1.75 | b | | | b | f | Y | late Pleist. |
| 1H-4, 10–12 | 4.60 | 4.62 | a | g | Gramineae, TCP, TC, Caryophyllaceae, Cyatheaceae, monolete and trilete spores | b | c | Y | late Pleist. |
| 3H-CC, 43–44 | 26.35 | 26.36 | f | m | Cyatheaceae | b | f | Y | late Pleist. |
| 5H-CC, 49–50 | 45.38 | 45.39 | f | m | Trilete and monolete spores | b | c | Y | late Pleist. |
| 7H-CC, 9–10 | 63.51 | 63.52 | b | | | b | f | Y | late Pleist. |
| 10H-CC, 9–10 | 91.06 | 91.07 | r | m | Stephanoporate | b | c | ? | ? |
| 13X-CC, 4–5 | 112.30 | 112.31 | f | m | Cyatheaceae | b | c | RW | late Pleist. |
| 15X-CC, 11–12 | 125.91 | 125.92 | f | m | TCP, monolete spores | b | c | RW | late Pleist. |
| 17X-CC, 16–17 | 150.89 | 150.90 | b | | | b | f | Y | late Pleist. |
| 18X-1, 75–77 | 155.25 | 155.27 | f | p | Cyatheaceae | b | c | Y | late Pleist. |
| 19X-CC, 27–28 | 172.34 | 172.35 | b | | | b | f | RW | late Pleist. |
| 21X-CC, 16–17 | 191.29 | 191.30 | f | m | TCP, Cyatheaceae | b | c | RW | late Pleist. |
| 23X-CC, 31–32 | 210.14 | 210.15 | r | p | TCP | b | c | RW | late Pleist. |
| 25X-CC, 41–42 | 229.77 | 229.78 | r | m | Trilete spore | b | f | RW | late Pleist. |
| 27X-CC, 24–25 | 251.58 | 251.59 | c | m | Palmae, Cyatheaceae, monolete spores | b | a | RW | late Pleist. |
| 29X-CC, 35–36 | 268.46 | 268.47 | f | m | Gramineae, monolete spore, *Hymenophyllum* | b | c | RW | late Pleist. |
| 31X-CC, 38–39 | 286.72 | 286.73 | f | p | Monolete (verrucate) spores, *Mauritia* | b | f | RW | late Pleist. |
| 33X-CC, 29–30 | 307.64 | 307.65 | b | | | b | r | ? | ? |
| 34X-CC, 0 | 318.20 | | b | | | b | r | ? | ? |
| 41X-CC, 18–19 | 382.18 | 382.19 | b | | | b | f | RW | m.-l. Pleist. |
| 42X-CC, 17–18 | 388.79 | 388.80 | b | | | b | f | ? | m.-l. Pleist. |
| 43X-CC, 63–64 | 405.48 | 405.49 | b | | | b | f | ? | m.-l. Pleist. |
| 44X-CC, 44–45 | 408.67 | 408.68 | b | | | b | f | ? | m.-l. Pleist. |
| 45X-CC, 42–43 | 423.04 | 423.05 | f | m | Cyatheaceae, monolete spores | b | c | ? | m.-l. Pleist. |
| 46X-CC, 37–38 | 426.19 | 426.20 | b | | | b | c | ? | m.-l. Pleist. |

Notes: TCP = tricolporate; TC = tricolpate.

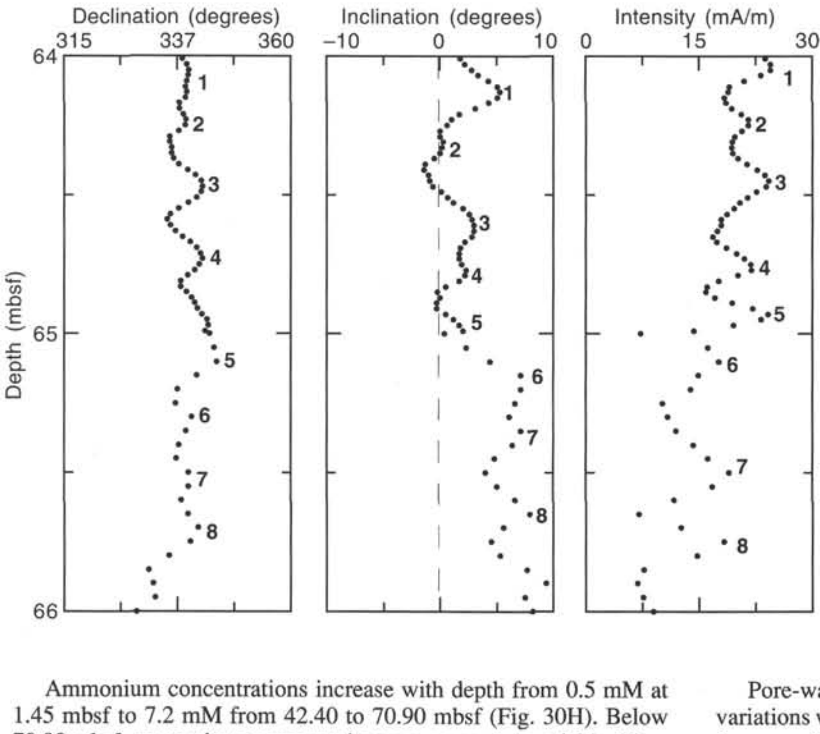


Figure 25. Apparent secular variation cycles from Sections 155-936A-8H-1 and -2 (numbered 1–8), as recorded in magnetic declination, inclination, and intensity. AF demagnetization level was 20 mT. Measurement interval was 2 cm for Section 155-936A-8H-1 (64–65 mbsf), and 5 cm for Section 155-936A-8H-2 (65–66 mbsf).

Ammonium concentrations increase with depth from 0.5 mM at 1.45 mbsf to 7.2 mM from 42.40 to 70.90 mbsf (Fig. 30H). Below 70.90 mbsf, ammonium concentrations are somewhat variable. They decrease to 4.6 mM at 110.70 mbsf, then increase to 7.3 mM at 208.65 mbsf, decrease to 5.0 mM at 295.25 mbsf, and finally increase again to 8.0 mM near the bottom of the hole.

Pore-water phosphate concentrations show a peak of 83.1 µM at 1.45 mbsf (Fig. 30I). Below 1.45 mbsf, phosphate concentrations are generally below 10 µM.

Dissolved silica concentrations increase steadily from 284 µM at 1.45 mbsf to 471 µM at 178.20 mbsf (Fig. 30J). A local minimum of 277 µM is found at 208.65 mbsf, then the values increase again to 589 µM at 295.25 mbsf. Below 295.25 mbsf, silica decreases to 293 µM at 380.35 mbsf and subsequently increases to 459 µM near the bottom of the hole.

Pore-water potassium and sodium concentrations exhibit similar variations with depth (Fig. 30K and 30L). Concentrations decrease in the upper 24.95 mbsf, from 11.3 to 7.2 mM for potassium, and from 479 to 466 mM for sodium. Potassium and sodium concentrations then both increase over the interval 24.65–149.20 mbsf to 9.2 mM potassium and 476 mM sodium, decrease from 149.20 to 266.55 mbsf to 5.9 mM potassium and 463 mM sodium, and increase again to 8.7 mM potassium and 478 mM sodium near the bottom of the hole.

Iron concentrations increase in the upper 25 m of the hole, from 48.1 µM at 1.45 mbsf to 118.3 µM at 24.95 mbsf (Fig. 30M). Iron then decreases to 52.0 µM at 42.40 mbsf. The concentration decreases more slowly, to 9.7 µM at 208.65 mbsf, then increases to 58.6 µM at 295.25 mbsf, and finally decreases again to near 9 µM near the bottom of the hole.

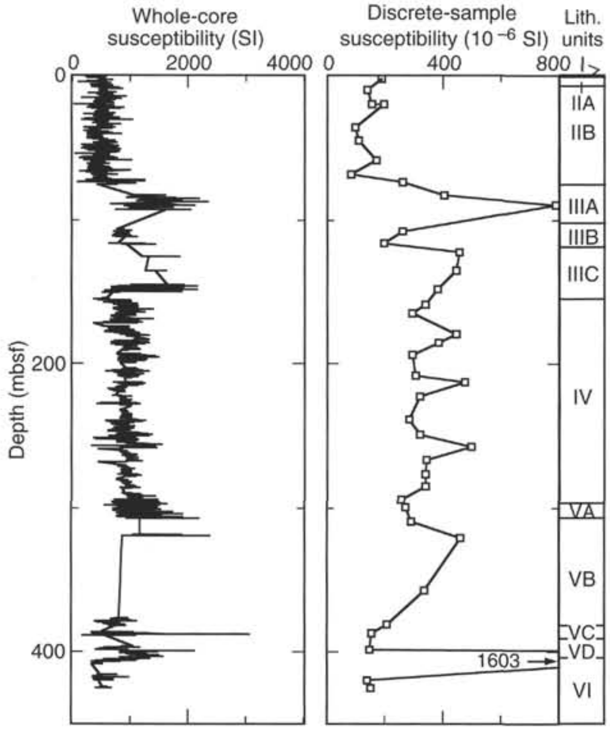


Figure 26. Whole-core and discrete-sample magnetic susceptibility data for Site 936.

Manganese concentrations are at a maximum of 29.2 µM at 1.45 mbsf (Fig. 30N). Thereafter, the concentrations are relatively constant, varying from 1.8 to 6.0 µM through the remainder of the hole.

## Sediment Geochemistry

Five mud samples and one sand sample were analyzed for major- and trace-element geochemistry (Tables 9 and 10). Mud samples were taken from the Upper, Middle, and Lower Levee complexes and from the Unit R Debris Flow; the sand sample was taken from the lower part of the Middle Levee Complex.

The composition of four of the muds is similar to muds of previous sites. $SiO_2$ varies from 62 to 63 wt%, $Al_2O_3$ is between 20 and 22 wt%, and CaO is between 0.6 and 0.9 wt%, indicating a mineralogy dominated by terrigenous clays. The mud from 403.14 mbsf has higher $SiO_2$ (71 wt%) and lower $Al_2O_3$ (14.5 wt%), indicating a less-clay-rich mineralogy and likely a greater sand component. CaO content of this sample is also relatively high (1.61 wt%), probably reflecting a greater carbonate component.

The sand composition is 85% $SiO_2$ and 6.9 wt% $Al_2O_3$ and has low concentrations of most other oxides and elements (Tables 9 and 10). A greater component of feldspar in the sand than in the mud is shown by higher $K_2O/Al_2O_3$ and $Na_2O/Al_2O_3$ (0.24 and 0.17, respectively, in the sand; 0.14 and 0.06–0.07 in the muds).

## PHYSICAL PROPERTIES

### Index Properties

Index properties were determined for all lithologic units in Hole 936A (Table 11).

The value of the single water content measurement in Unit I is 45.6%. Water content decreases downhole in Unit II from 57% to 30% (Fig. 31). Between 19 and 23 mbsf, water content is about 3% to 4% less than the downhole trend. Below the base of Unit II at 72 mbsf, water content decreases rapidly to 14% in sand types at 83 mbsf. These values are probably unrepresentative of in-situ conditions as pore-water drainage is likely to have occurred prior to sampling. At 83.53 mbsf, a clay clast within the sand unit has a water content of 31.5% (Sample 936A-10H-1, 103–105 cm), which is typical for sediment in the lower part of Unit II. Sand and silty clay intervals below the clast have water contents only slightly reduced from

**Table 6. Gas concentrations in sediments from Site 936.**

| Core, section, interval (cm) | Depth (mbsf) | Sed. temp.* (°C) | Methane HS (ppm) | Methane VAC (ppm) |
|---|---|---|---|---|
| 155-936A- | | | | |
| 1H-1, 0–5 | 0.00 | 2 | 7,801 | |
| 2H-7, 0–5 | 15.50 | 2 | 9,048 | 178,465 |
| 3H-7, 0–5 | 25.00 | 3 | 7,322 | 263,941 |
| 4H-5, 0–5 | 31.50 | 3 | 7,870 | 803,804 |
| 5H-6, 0–5 | 42.50 | 3 | 8,021 | 235,827 |
| 6H-6, 0–5 | 52.00 | 3 | 7,099 | 433,806 |
| 7H-1, 145–150 | 55.45 | 4 | 6,926 | |
| 8H-6, 0–5 | 71.00 | 4 | 9,654 | 40,179 |
| 10H-6, 0–5 | 90.00 | 5 | 5,466 | 112,625 |
| 11X-1, 0–5 | 92.00 | 5 | 6,320 | |
| 13X-4, 0–5 | 110.80 | 5 | 7,972 | |
| 14X-1, 0–5 | 115.90 | 5 | 18,128 | |
| 16X-1, 0–5 | 135.20 | 6 | 8,427 | |
| 17X-4, 0–5 | 149.30 | 6 | 8,427 | 16,990 |
| 18X-6, 0–5 | 162.00 | 7 | 8,907 | |
| 19X-5, 0–5 | 170.10 | 7 | 10,799 | |
| 20X-4, 0–5 | 178.30 | 7 | 16,065 | |
| 21X-5, 0–5 | 189.40 | 7 | 16,697 | |
| 22X-4, 0–5 | 197.60 | 8 | 6,767 | |
| 23X-5, 0–5 | 208.80 | 8 | 11,222 | |
| 24X-1, 145–150 | 213.95 | 8 | 7,159 | |
| 25X-5, 0–5 | 228.10 | 8 | 7,666 | |
| 26X-6, 0–5 | 239.20 | 9 | 7,033 | |
| 27X-5, 0–5 | 247.40 | 9 | 7,033 | |
| 28X-5, 0–5 | 257.10 | 9 | 5,622 | |
| 29X-5, 0–5 | 266.70 | 9 | 9,511 | |
| 30X-5, 0–5 | 276.40 | 10 | 7,143 | |
| 31X-4, 0–5 | 284.40 | 10 | 14,937 | |
| 32X-6, 0–5 | 296.90 | 10 | 9,845 | 237,541 |
| 33X-6, 0–5 | 306.50 | 11 | 10,146 | 440,786 |
| 35X-1, 0–5 | 318.20 | 11 | 17,503 | |
| 36X-CC, 0–5 | 327.90 | 11 | 5,476 | |
| 38X-CC, 0–5 | 347.20 | 12 | 5,671 | |
| 39X-1, 0–5 | 356.80 | 12 | 973 | |
| 41X-4, 0–5 | 380.50 | 13 | 7,549 | |
| 42X-1, 0–5 | 385.70 | 13 | 8,199 | |
| 43X-6, 0–5 | 402.14 | 13 | 7,319 | 373,560 |
| 44X-2, 0–5 | 406.50 | 13 | 13,143 | |
| 45X-2, 0–5 | 415.34 | 14 | 9,336 | |
| 46X-1, 0–5 | 424.20 | 14 | 18,561 | |

Notes: HS = Headspace; VAC = Vacutainer. Geothermal gradient = 28°C/km. Bottom-water temperature = 2°C. *See "In-situ Temperature Measurements" section, this chapter.

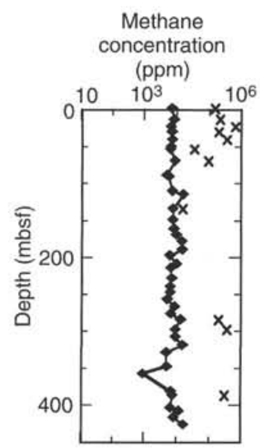


Figure 27. Methane concentrations at Site 936. Headspace (diamond) and vacutainer (×) samples are plotted.

Table 7. Elemental and organic carbon compositions of sediments from Site 936.

| Core, section, interval (cm) | Depth (mbsf) | IC (%) | $CaCO_3$* (%) | TC (%) | TOC (%) | TN (%) | TS (%) | [C/N]a | Lith. unit |
|---|---|---|---|---|---|---|---|---|---|
| 155-936A- | | | | | | | | | |
| 1H-1, 27–28 | 0.27 | 5.06 | 42.1 | 5.58 | 0.52 | 0.07 | 0.13 | 9 | I |
| 1H-1, 75–76 | 0.75 | 0.70 | 5.8 | 1.16 | 0.46 | 0.10 | 0.19 | 5 | |
| 1H-3, 60–61 | 3.60 | 0.19 | 1.6 | 1.18 | 0.99 | 0.12 | 0.80 | 10 | |
| 1H-5, 29–30 | 6.29 | 0.17 | 1.4 | 1.19 | 1.02 | 0.11 | 0.12 | 11 | |
| 2H-3, 107–108 | 10.57 | 0.28 | 2.3 | 1.38 | 1.10 | 0.13 | 0.08 | 10 | |
| 2H-7, 41–42 | 15.91 | 0.22 | 1.8 | 1.46 | 1.24 | 0.14 | 0.00 | 10 | |
| 3H-2, 54–55 | 17.99 | 0.17 | 1.4 | 1.31 | 1.14 | 0.13 | 0.00 | 10 | |
| 3H-5, 54–55 | 22.49 | 0.22 | 1.8 | 1.26 | 1.04 | 0.14 | 0.00 | 9 | |
| 4H-1, 90–91 | 26.40 | 0.14 | 1.2 | 1.07 | 0.93 | 0.09 | 0.08 | 12 | |
| 4H-1, 96–97 | 26.46 | 0.28 | 2.3 | 1.36 | 1.08 | 0.13 | 0.17 | 10 | II |
| 4H-6, 32–33 | 33.32 | 0.21 | 1.7 | 1.15 | 0.94 | 0.13 | 0.00 | 8 | |
| 5H-3, 50–52 | 38.50 | 0.28 | 2.3 | 1.38 | 1.10 | 0.14 | 0.00 | 9 | |
| 5H-6, 50–52 | 43.00 | 0.22 | 1.8 | 1.29 | 1.07 | 0.12 | 0.00 | 10 | |
| 6H-1, 37–38 | 44.87 | 0.28 | 2.3 | 1.44 | 1.16 | 0.13 | 0.00 | 10 | |
| 6H-5, 54–55 | 51.04 | 0.21 | 1.7 | 1.31 | 1.10 | 0.13 | 0.00 | 10 | |
| 7H-3, 60–61 | 57.60 | 0.19 | 1.6 | 1.20 | 1.01 | 0.12 | 0.00 | 10 | |
| 7H-2, 85–86 | 56.35 | 0.14 | 1.2 | 0.81 | 0.67 | 0.09 | 0.00 | 9 | |
| 7H-7, 84–85 | 63.30 | 0.25 | 2.1 | 1.32 | 1.07 | 0.12 | 0.00 | 10 | |
| 8H-6, 29–30 | 71.29 | 0.18 | 1.5 | 1.34 | 1.16 | 0.13 | 0.13 | 10 | |
| 8H-6, 132–133 | 72.32 | 0.00 | 0.0 | 0.10 | 0.10 | 0.07 | 0.00 | 2 | |
| 8H-7, 6–7 | 72.56 | 0.22 | 1.8 | 1.02 | 0.80 | 0.11 | 0.08 | 8 | |
| 9H-1, 119–120 | 74.19 | 0.12 | 1.0 | 0.87 | 0.75 | 0.10 | 0.08 | 9 | |
| 10H-4, 99–100 | 87.99 | 0.11 | 0.9 | 0.64 | 0.53 | 0.06 | 0.00 | 10 | |
| 11X-1, 26–27 | 92.26 | 0.17 | 1.4 | 1.18 | 1.01 | 0.11 | 0.08 | 11 | III |
| 13X-2, 46–47 | 108.26 | 0.22 | 1.8 | 1.20 | 0.98 | 0.11 | 0.07 | 10 | |
| 14X-1, 8–9 | 115.98 | 0.18 | 1.5 | 1.01 | 0.83 | 0.11 | 0.00 | 9 | |
| 17X-3, 97–98 | 148.77 | 0.09 | 0.7 | 0.19 | 0.10 | 0.02 | 0.25 | 5 | |
| 17X-3, 107–108 | 148.87 | 0.39 | 3.2 | 0.83 | 0.44 | 0.07 | 0.23 | 7 | |
| 17X-4, 102–103 | 150.32 | 0.36 | 3.0 | 1.01 | 0.65 | 0.10 | 0.22 | 8 | |
| 18X-1, 69–70 | 155.19 | 0.20 | 1.7 | 1.05 | 0.85 | 0.08 | 2.01 | 12 | |
| 18X-1, 71–72 | 155.21 | 0.32 | 2.7 | 1.01 | 0.69 | 0.08 | 1.34 | 10 | |
| 19X-1, 40–41 | 164.50 | 0.34 | 2.8 | 1.19 | 0.85 | 0.09 | 0.28 | 11 | |
| 19X-5, 33–34 | 170.43 | 0.50 | 4.2 | 1.20 | 0.70 | 0.10 | 0.29 | 9 | |
| 20X-3, 45–46 | 177.25 | 0.31 | 2.6 | 1.15 | 0.84 | 0.11 | 0.31 | 9 | |
| 20X-4, 85–86 | 179.15 | 0.31 | 2.6 | 1.21 | 0.90 | 0.10 | 0.16 | 11 | |
| 22X-2, 30–31 | 194.90 | 0.18 | 1.5 | 0.89 | 0.71 | 0.08 | 0.06 | 10 | |
| 22X-4, 109–110 | 198.69 | 0.26 | 2.2 | 1.23 | 0.97 | 0.11 | 0.22 | 10 | |
| 23X-5, 59–60 | 209.39 | 0.31 | 2.6 | 1.19 | 0.88 | 0.11 | 0.06 | 9 | |
| 23X-1, 110–111 | 203.90 | 0.30 | 2.5 | 1.15 | 0.85 | 0.10 | 0.09 | 10 | |
| 24X-2, 106–107 | 215.06 | 0.32 | 2.7 | 1.22 | 0.90 | 0.10 | 0.07 | 11 | |
| 25X-1, 60–61 | 222.70 | 0.31 | 2.6 | 1.19 | 0.88 | 0.10 | 0.08 | 10 | IV |
| 25X-5, 96–97 | 229.06 | 0.30 | 2.5 | 1.18 | 0.88 | 0.10 | 0.09 | 11 | |
| 26X-4, 28–29 | 236.48 | 0.31 | 2.6 | 1.24 | 0.93 | 0.10 | 0.04 | 11 | |
| 26X-6, 29–30 | 239.49 | 0.16 | 1.3 | 1.02 | 0.86 | 0.11 | 0.94 | 9 | |
| 27X-6, 72–73 | 249.62 | 0.30 | 2.5 | 1.24 | 0.94 | 0.09 | 0.23 | 12 | |
| 28X-4, 107–108 | 256.67 | 0.25 | 2.1 | 0.90 | 0.65 | 0.07 | 0.08 | 10 | |
| 28X-5, 89–90 | 257.99 | 0.26 | 2.2 | 1.13 | 0.87 | 0.10 | 0.18 | 10 | |
| 29X-2, 90–91 | 263.10 | 0.33 | 2.7 | 1.18 | 0.85 | 0.10 | 0.11 | 10 | |
| 29X-5, 88–89 | 267.58 | 0.31 | 2.6 | 1.18 | 0.87 | 0.10 | 0.08 | 10 | |
| 30X-5, 40–41 | 276.80 | 0.29 | 2.4 | 1.09 | 0.80 | 0.09 | 0.05 | 10 | |
| 30X-5, 90–91 | 277.30 | 0.27 | 2.2 | 1.01 | 0.74 | 0.09 | 0.05 | 9 | |
| 31X-3, 93–94 | 283.83 | 0.32 | 2.7 | 1.17 | 0.85 | 0.14 | 0.26 | 7 | |
| 32X-4, 12–13 | 294.02 | 0.17 | 1.4 | 0.77 | 0.60 | 0.11 | 0.16 | 7 | |
| 32X-4, 28–29 | 294.18 | 0.29 | 2.4 | 1.13 | 0.84 | 0.12 | 0.00 | 8 | |
| 33X-1, 21–22 | 299.21 | 0.23 | 1.9 | 0.98 | 0.75 | 0.11 | 0.09 | 8 | |
| 33X-5, 84–85 | 305.84 | 0.41 | 3.4 | 1.27 | 0.86 | 0.10 | 0.07 | 10 | |
| 41X-4, 50–51 | 381.00 | 0.23 | 1.9 | 0.89 | 0.66 | 0.07 | 0.14 | 10 | |
| 42X-1, 66–67 | 386.36 | 1.40 | 11.7 | 1.81 | 0.41 | 0.08 | 0.06 | 6 | |
| 42X-2, 32–33 | 387.52 | 1.04 | 8.7 | 1.22 | 0.18 | 0.05 | 8.01 | 4 | |
| 42X-2, 59–62 | 387.79 | 0.27 | 2.2 | 0.71 | 0.44 | 0.05 | 0.43 | 10 | V |
| 42X-2, 106–107 | 388.26 | 2.69 | 22.4 | 4.15 | 1.46 | 0.09 | 0.48 | 18 | |
| 42X-2, 112–113 | 388.32 | 3.86 | 32.2 | 4.54 | 0.68 | 0.08 | 0.43 | 10 | |
| 43X-2, 59–60 | 396.73 | 0.27 | 2.2 | 1.13 | 0.86 | 0.10 | 0.38 | 10 | |
| 43X-6, 98–99 | 403.12 | 0.32 | 2.7 | 0.71 | 0.39 | 0.05 | 0.13 | 9 | |
| 43X-7, 103–104 | 404.67 | 0.36 | 3.0 | 0.76 | 0.40 | 0.07 | 0.10 | 7 | |
| 44X-1, 19–20 | 405.19 | 0.46 | 3.8 | 0.85 | 0.39 | 0.06 | 0.21 | 8 | |
| 44X-2, 57–58 | 407.07 | 0.81 | 6.7 | 1.15 | 0.34 | 0.09 | 0.07 | 4 | |
| 45X-1, 13–14 | 414.73 | 0.45 | 3.7 | 1.41 | 0.96 | 0.08 | 0.08 | 14 | VI |
| 45X-3, 67–68 | 417.51 | 0.30 | 2.5 | 1.65 | 1.35 | 0.08 | 0.11 | 19 | |
| 46X-1, 57–58 | 424.77 | 0.43 | 3.6 | 1.35 | 0.92 | 0.12 | 0.00 | 9 | |

*Calculated assuming all IC is calcite.

that of the clast and are thought to be more representative of in-situ conditions.

In the upper part of lithologic Unit IV, between 154 and 225 mbsf, water content is lower than it is in the clayey sediment of Unit III and ranges from 22% to 30%. The water content profile comprises a series of 10- to 15-m-thick intervals each exhibiting a downhole increase (Fig. 32). These trends are similar to those noted at Site 932, but they do not coincide with core boundaries. Water content ranges from 19% to 20% and is less variable in the lower part of Unit IV (225 mbsf to 294 mbsf); however, the pattern of water content trends is more complex (Fig. 32).

Below 294 mbsf, in Subunits VA and VB, water content is high at the top of a sequence of poor recovery. Sample 936A-35X-1, 85–87 cm (319.05 mbsf), comprises soft mud and may be severely dis-

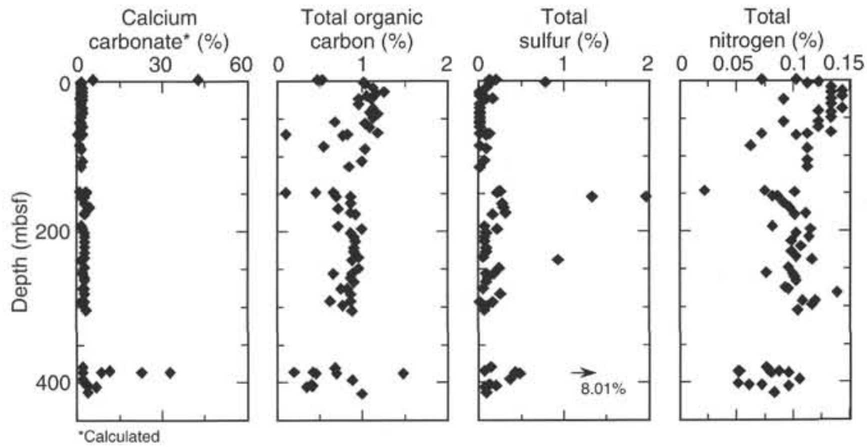


Figure 28. Concentration profiles of calcium carbonate, total organic carbon, total sulfur, and total nitrogen in Hole 936A.

turbed. Water content decreases downhole from 26% to 16% in lithologic Subunits VC and VD. In lithologic Unit VI, it gradually decreases with depth from 24% to 22% at the base of the hole.

The porosity and wet-bulk density profiles show fluctuations similar to those of the water content profile. The trends within the upper part of Unit IV are even more marked on the porosity and wet-bulk density profiles (Fig. 31). These trends suggest that the 154–225 mbsf interval comprises several mass-transport deposits that experienced pore-water drainage at their upper surface prior to the deposition of the subsequent flow.

Grain density ranges between 2.70 and 2.80 g/cm$^3$ (Table 11). The variability is low, as are differences in grain density between lithologies. Silty clays compose the bulk of the samples measured and have an average grain density of 2.74 g/cm$^3$. Average grain density for sand types at the top of Unit III is 2.70 g/cm$^3$. An anomalously high value of 2.97 g/cm$^3$ was obtained from sand types at 405.4 mbsf.

Because of the low variability in grain density, the downhole variation of wet-bulk density in Hole 936A essentially matches the variation in water content (Fig. 31). From the top of Unit II to the base of the hole, wet-bulk density increases from approximately 1.40 to 2.20 g/cm$^3$. GRAPE data reflect the general trends in wet-bulk density (Fig. 31). The divergence in the GRAPE and discrete sample data begins in Core 936A-2H, coinciding with the first occurrence of gas-induced sediment expansion. Unlike at previous sites, the discrepancy between the GRAPE and the discrete-sample wet-bulk densities is low, 0.1 to 0.3 g/cm$^3$. Between 10 and 70 mbsf, it is only 0.1 g/cm$^3$. Locally, wet-bulk density measurements from discrete samples are lower than those from the GRAPE, most notably in the upper 10 m and at 40 mbsf, 75 mbsf, and 90 mbsf.

## Compressional-wave Velocity

Transverse velocities averaging 1489 m/s were obtained by the PWL for the upper 5.9 m in Hole 936A. Longitudinal velocity measurements using the DSV were only successful in the upper 3.7 m and range from 1482 to 1488 m/s. Because core expansion produced pervasive microfractures in the sediment, velocities were not obtained from greater depths.

## Shear Strength

Measurements of undrained shear strength were made using the motorized shear vane on most cores from Hole 936A (Table 12). Below 145 mbsf, compressive strengths were determined using a pocket penetrometer. There is good correlation between shear-strength values assumed from the compressive strength and those determined by the motorized shear vane, particularly with those shear-vane measurements where failure involved only a limited degree of cracking.

The shear-strength profile can be subdivided with boundaries similar to those shown by the index properties. From seafloor to 72 mbsf (Units I and II), undrained shear strength increases steadily except in an interval with elevated values at 40 mbsf (Fig. 33). Below 40 mbsf, the variability in shear strength increases. The poor core recovery in lithologic Unit III, between 72 and 150 mbsf, allowed only a few scattered measurements, which range from 27 to 81 kPa. The upper part of Unit IV (150 to 225 mbsf) has shear strengths generally between 75 and 115 kPa, slightly below that expected from the compressive-strength measurements, which range from 170 to 270 kPa (Table 12). Scatter in shear-strength values increases in the lower part of Unit IV (between 225 and 294 mbsf). Shear strengths are generally between 110 and 200 kPa in this interval. Values are extremely scattered within Subunits VA and VB. The high shear strength (256.4 kPa) at 306.95 mbsf probably results from pore-water drainage by underlying coarser sediment. The section of good recovery from 376 mbsf to the base of the hole (Subunits VC and VD, and Unit VI) yielded the stiffest sediment in Hole 936A. This sediment commonly exceeded the capacity of both the pocket penetrometer ($S_u$ > 220 kPa) and the motorized shear vane (>240 kPa). Values determined below these limits may be the result of premature failing by fracturing.

## Resistivity

Longitudinal and transverse resistivity were determined (Table 13). Longitudinal resistivity displays a general downhole increase that parallels the downhole decrease in porosity (Fig. 34). Longitudinal resistivity follows similar trends in Unit II and the upper part of Unit IV (to 225 mbsf), increasing at $0.95 \times 10^{-3}$ Ωm per meter downhole. Small offsets in the general trend of resistivities within lithologic Unit II and the upper part of lithologic Unit IV do not correspond with changes noted in porosity (Fig. 31). Below 225 mbsf there is much greater variability in the resistivity values, with several zones of downhole increases that correspond with decreases in porosity. The lowermost interval (Subunits VC and VD, and Unit VI) has the highest resistivity. Resistivity is highly variable in this interval and increases with depth from 0.5 to 0.7 Ωm.

As in Hole 935A, resistivity anisotropy does not differ significantly among lithologic units. Most units at the site are characterized by a scatter of ±10% in the anisotropy. Greater scatter in anisotropy is present in the mass-transport deposit between 225 and 294 mbsf in Unit IV and in Subunit IIIC.

The overall trends downhole in laboratory resistivity measurements in the upper part of Unit IV are similar to those obtained by downhole logging, but the profiles differ in the detail of offsets and small-scale trends. The small-scale trends in the borehole resistivity log match the trends in water content (Fig. 32). This match combined with the correspondence of the offsets in the laboratory resistivity

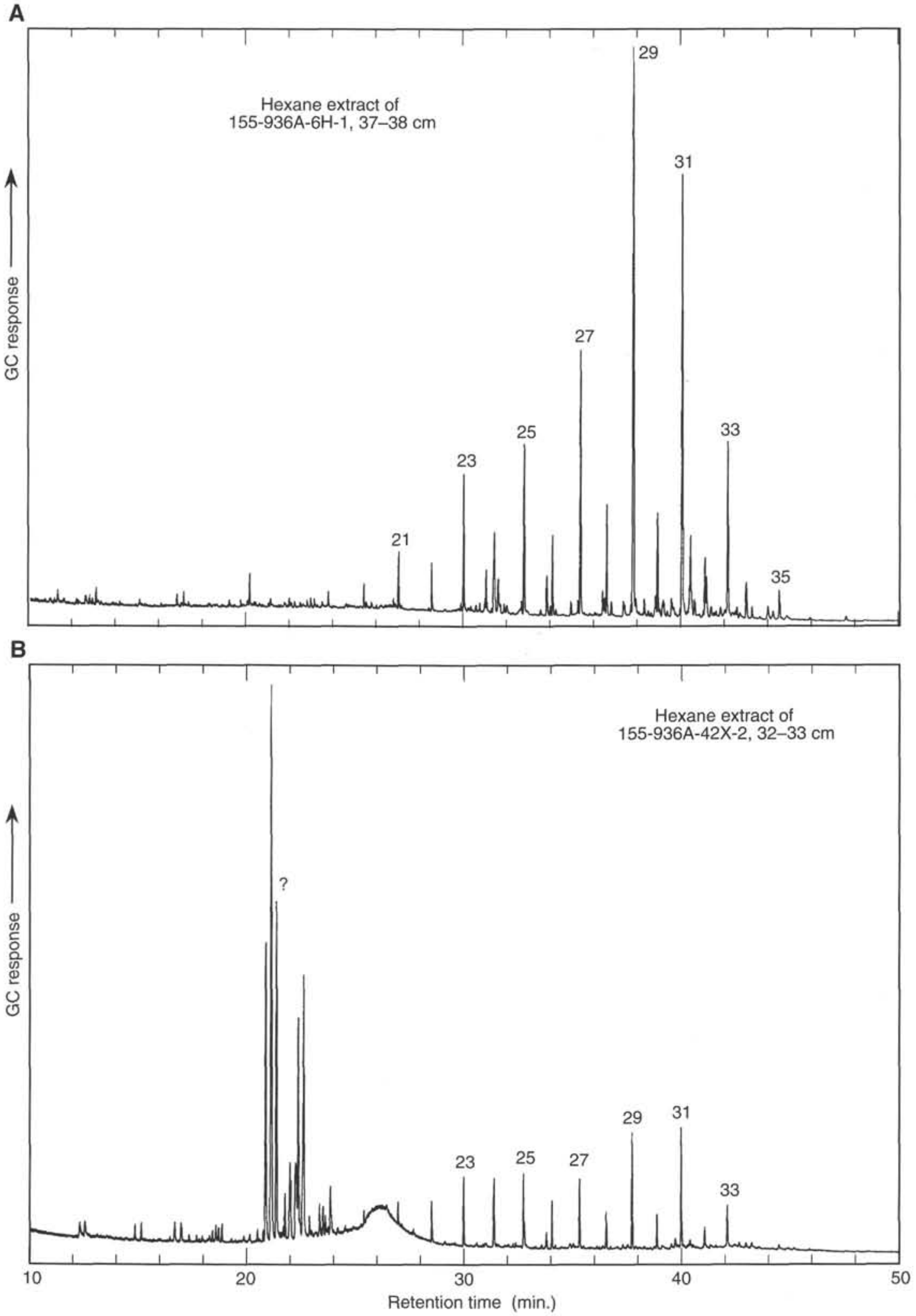


Figure 29. **A.** Gas chromatogram of *n*-hexane extract from Sample 155-936A-6H-1, 37–38 cm. **B.** Gas chromatogram of *n*-hexane extract from Sample 155-936A-42X-2, 32–33 cm. The chromatographic peaks corresponding to the major hydrocarbons are identified by their carbon number. Identification is assigned based on co-injection with authentic standards. Odd-carbon-numbered *n*-alkanes are marked with their carbon number.

**Table 8. Interstitial water chemistry, Site 936.**

| Core, section, interval (cm) | Depth (mbsf) | Salinity | pH | Alkalinity (mM) | $Cl^-$ (mM) | $Mg^{2+}$ (mM) | $Ca^{2+}$ (mM) | $K^+$ (mM) | $HPO_4^{2-}$ (µM) | $SO_4^{2-}$ (mM) | $NH_4^+$ (mM) | $H_4SiO_4$ (µM) | $Na^+$ (mM) | $Fe^{2+}$ (µM) | $Mn^{2+}$ (µM) |
|---|---|---|---|---|---|---|---|---|---|---|---|---|---|---|---|
| 155-936A- | | | | | | | | | | | | | | | |
| 1H-1, 145–150 | 1.45 | 34.0 | 7.71 | 9.92 | 553 | 46.0 | 8.5 | 11.3 | 83.1 | 18.1 | 0.5 | 284 | 479 | 48.1 | 29.2 |
| 2H-6, 145–150 | 15.45 | 32.0 | 7.42 | 9.70 | 557 | 39.2 | 4.1 | 7.5 | 6.9 | 0.0 | 5.2 | 361 | 468 | 90.2 | 4.8 |
| 3H-6, 145–150 | 24.95 | 34.0 | 7.32 | 7.05 | 559 | 39.2 | 4.2 | 7.2 | 3.4 | 0.0 | 6.9 | 332 | 466 | 118.3 | 5.3 |
| 4H-5, 140–150 | 32.90 | 32.5 | 7.30 | 6.39 | 563 | 39.4 | 4.2 | 7.4 | 3.1 | 0.0 | 7.1 | 334 | 467 | 85.2 | 5.8 |
| 5H-5, 140–150 | 42.40 | 33.0 | 7.39 | 4.59 | 564 | 40.1 | 4.5 | 7.4 | 2.1 | 0.0 | 7.2 | 351 | 465 | 52.0 | 4.4 |
| 8H-5, 140–150 | 70.90 | 33.0 | 7.55 | 10.91 | 564 | 40.3 | 4.8 | 8.1 | 7.5 | 0.0 | 7.2 | 344 | 469 | 46.1 | 4.0 |
| 13X-3, 140–150 | 110.70 | 32.0 | 7.68 | 8.17 | 559 | 35.9 | 4.4 | 7.7 | 2.5 | 0.0 | 4.6 | 396 | 474 | 54.0 | 4.2 |
| 17X-3, 140–150 | 149.20 | 33.0 | 7.71 | 15.90 | 559 | 38.9 | 5.4 | 9.2 | 5.1 | 2.2 | 4.7 | 445 | 476 | 26.0 | 5.6 |
| 20X-3, 140–150 | 178.20 | 32.5 | 7.61 | 10.39 | 557 | 39.3 | 5.1 | 8.2 | 4.3 | 3.2 | 5.8 | 471 | 471 | 34.0 | 6.0 |
| 23X-4, 135–150 | 208.65 | 33.0 | 7.61 | 9.81 | 555 | 37.8 | 4.7 | 8.3 | 5.0 | 0.0 | 7.3 | 277 | 464 | 9.7 | 2.1 |
| 26X-5, 135–150 | 239.05 | 32.5 | 7.58 | 10.33 | 558 | 39.0 | 4.9 | 6.5 | 3.7 | 0.0 | 6.6 | 440 | 467 | 15.3 | 3.8 |
| 29X-4, 135–150 | 266.55 | 32.0 | 7.58 | 11.16 | 547 | 37.1 | 4.4 | 5.9 | 4.2 | 0.0 | 5.8 | 450 | 463 | 29.4 | 2.8 |
| 32X-4, 135–150 | 295.25 | 32.5 | 7.51 | 11.28 | 556 | 37.5 | 5.5 | 6.9 | 11.2 | 2.6 | 5.0 | 589 | 474 | 58.6 | 3.7 |
| 41X-3, 135–150 | 380.35 | 32.5 | 7.86 | 9.99 | 557 | 32.7 | 4.1 | 8.7 | 6.7 | 0.0 | 6.1 | 293 | 478 | 9.6 | 1.8 |
| 44X-1, 135–150 | 406.35 | 33.0 | 7.72 | 13.48 | 562 | 32.5 | 4.6 | 6.7 | 7.5 | 0.0 | 8.0 | 459 | 486 | 8.9 | 3.8 |

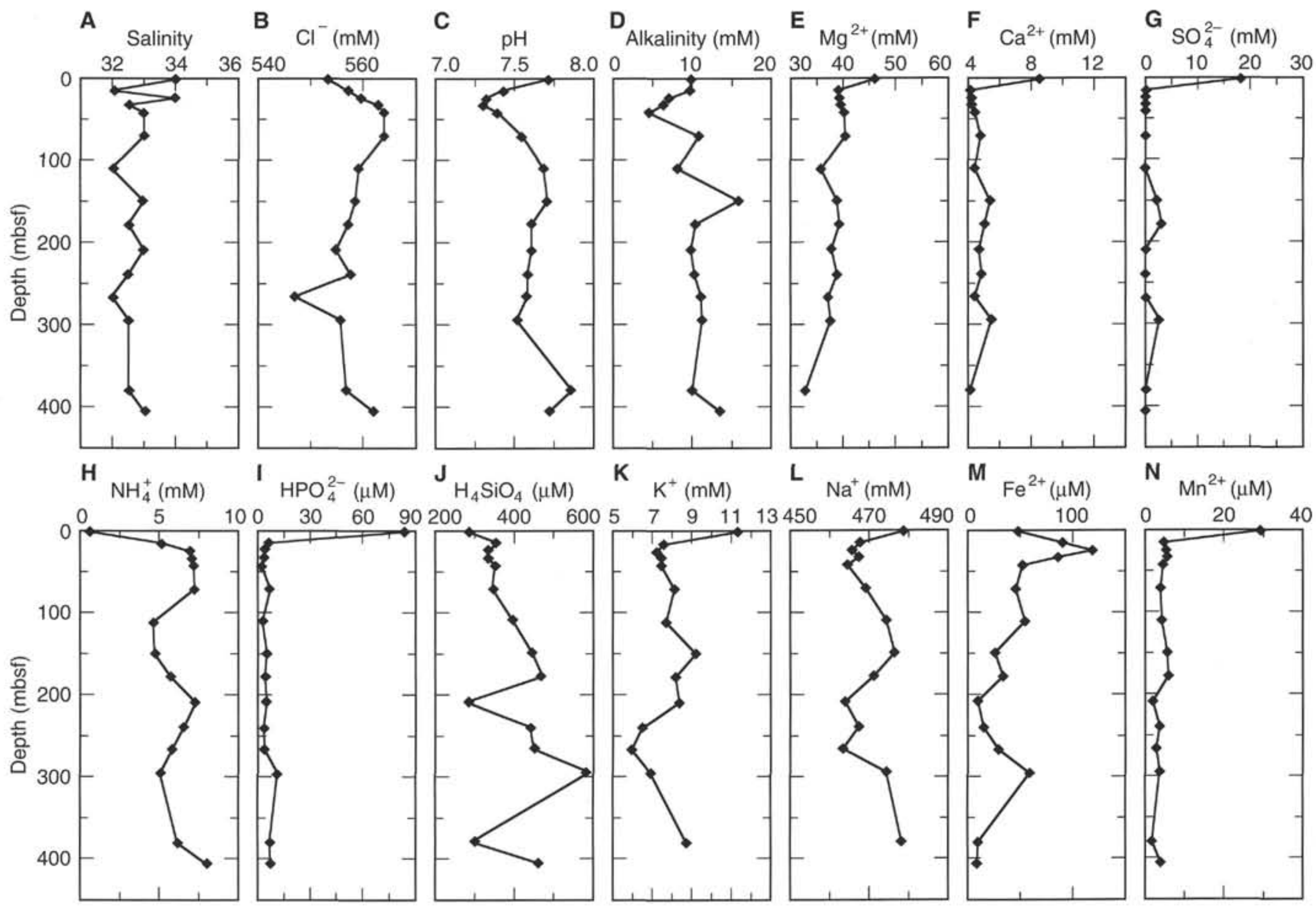


Figure 30. Downcore variation in pore-water chemistry: **A.** Salinity. **B.** Chloride. **C.** pH. **D.** Alkalinity. **E.** Magnesium. **F.** Calcium. **G.** Sulfate. **H.** Ammonium. **I.** Phosphate. **J.** Silica. **K.** Potassium. **L.** Sodium. **M.** Iron. **N.** Manganese.

measurements with core boundaries, suggests that the laboratory resistivity trends are derived in part from the coring and sampling processes.

## DOWNHOLE LOGGING

### Logging Operations and Quality of Logs

After completion of drilling and coring, the borehole was cleaned by circulating sepiolite mud mixed with seawater, and the drill pipe was raised to 83.5 mbsf, then returned to total depth to ream out borehole irregularities. At 383 mbsf, 25 m of fill was encountered and removed by circulating seawater. The base of the bottom-hole assembly (BHA) then was set at 83 mbsf, and the drill string was prepared to be raised to 65 mbsf during logging. The logging program included the Quad-combination, Formation MicroScanner (FMS), and geochemical (GLT) tool strings. During the first logging run, a bridge was encountered at 333 mbsf. During subsequent logging runs, sediment continued to fill the hole, and successive runs covered slightly shorter intervals (Table 14).

**Table 9. Major element composition (wt%) of sediment samples, Site 936.**

| Core, section, interval (cm) | Depth (mbsf) | Lith. | $SiO_2$ | $TiO_2$ | $Al_2O_3$ | $Fe_2O_3$ | MnO | MgO | CaO | $Na_2O$ | $K_2O$ | $P_2O_5$ | Total | LOI |
|---|---|---|---|---|---|---|---|---|---|---|---|---|---|---|
| 155-936A- | | | | | | | | | | | | | | |
| 4H-6, 29–31 | 33.29 | Mud | 61.65 | 1.09 | 22.02 | 7.78 | 0.11 | 2.08 | 0.68 | 1.32 | 3.04 | 0.18 | 99.94 | 7.94 |
| 25X-4, 50–55 | 227.10 | Mud | 62.24 | 1.09 | 21.11 | 7.79 | 0.11 | 2.07 | 0.92 | 1.57 | 2.93 | 0.20 | 100.03 | 7.84 |
| 39X-1, 40–45 | 357.20 | Sand | 85.41 | 0.40 | 6.85 | 2.16 | 0.03 | 0.50 | 0.68 | 1.13 | 1.62 | 0.03 | 98.81 | 1.87 |
| 41X-4, 110–115 | 381.60 | Mud | 63.33 | 1.07 | 20.45 | 7.23 | 0.07 | 1.91 | 0.57 | 1.34 | 2.94 | 0.25 | 99.16 | 6.87 |
| 43X-6, 100–105 | 403.14 | Mud | 71.10 | 0.80 | 14.50 | 5.34 | 0.07 | 1.34 | 1.61 | 1.21 | 2.32 | 0.15 | 98.45 | 5.49 |
| 46X-2, 65–68 | 425.64 | Mud | 61.87 | 1.04 | 20.86 | 8.56 | 0.12 | 2.06 | 0.82 | 1.45 | 2.95 | 0.19 | 99.91 | 7.60 |

Notes: Total iron is reported as $Fe_2O_3$. LOI = loss on ignition.

**Table 10. Trace element composition (ppm) of sediment samples, Site 936.**

| Core, section, interval (cm) | Depth (mbsf) | Lith. | Ba | Ce | Cr | Cu | Nb | Ni | Rb | Sr | V | Y | Zn | Zr |
|---|---|---|---|---|---|---|---|---|---|---|---|---|---|---|
| 155-936A- | | | | | | | | | | | | | | |
| 4H-6, 29–31 | 33.29 | Mud | 474 | 114 | 71 | 34 | 23 | 33 | 134 | 141 | 86 | 40 | 124 | 244 |
| 25X-4, 50–55 | 227.10 | Mud | 493 | 106 | 66 | 31 | 23 | 35 | 128 | 160 | 89 | 39 | 126 | 245 |
| 39X-1, 40–45 | 357.20 | Sand | 395 | 44 | 15 | 4 | 9 | 8 | 56 | 116 | 0 | 24 | 39 | 175 |
| 41X-4, 110–115 | 381.60 | Mud | 480 | 109 | 65 | 31 | 22 | 31 | 129 | 130 | 74 | 39 | 119 | 253 |
| 43X-6, 100–105 | 403.14 | Mud | 420 | 78 | 47 | 18 | 17 | 22 | 98 | 163 | 53 | 34 | 84 | 303 |
| 46X-2, 65–68 | 425.64 | Mud | 480 | 99 | 68 | 31 | 22 | 34 | 123 | 146 | 88 | 40 | 120 | 233 |

Logs of good quality were obtained at this site. The density (HLDT) tool caliper showed significant washed-out intervals only between 75 and 82 mbsf and below 310 mbsf (Fig. 35). A borehole constriction having a diameter of ~5 in. (13 cm) occurred at 82 to 85 mbsf. This upper washout and bridge may have been caused by the movement of the BHA during logging. Data collected within the washouts have been adversely affected by the large borehole diameter. Summary figures of the shore-based processed logs appear at the end of this chapter and on the CD-ROM (back pocket of this volume).

## Results

Logging data were obtained over lithostratigraphic Subunit IIB, Units III and IV, and Subunits VA and VB. Below Unit II, a sharp decrease in resistivity marks a change in trend to nearly constant values (~1.25 Ωm) within Unit III. The boundary between Units III and IV (154 mbsf) clearly is defined in all logs, including a distinct change in the gamma-ray character and an abrupt increase in resistivity, density, and sonic velocity within Unit IV. Unit III has higher Si yields and lower Al concentration than Unit IV (Fig. 36). Below Unit IV, an abrupt decrease in resistivity, sonic velocity, and density can be observed.

Well-logs help to determine the physical and chemical characteristics in intervals of poor core recovery in Unit III. Three subunits can be distinguished in the logging data that are similar to those established from core observations. Within Subunit IIIA, we observed relatively low gamma-ray values and high velocity and density. In contrast, Subunit IIIB is characterized by high gamma-ray values and nearly constant velocity and density. Subunit IIIB also displays higher Al and lower Si contents than Subunit IIIA, which correlates to a predominantly silty clay lithology. Although core recovery in Subunit IIIC was poor, its logging signature is similar to that of Subunit IIIA and has been interpreted as containing thick sand beds interbedded with silty clays (Fig. 37A).

Within Unit III, a comparison with core observations shows a strong correlation between the total gamma ray and the presence of finer grained silt and clay intervals (Fig. 37A). It appears that the silty clays and thin-bedded sandy turbidites within Subunit IIIB probably extend uphole to about 100 mbsf. A similar response can be observed at the base of Subunit IIIC, where recovered sediment in Core 936A-17X may have been assigned an incorrect depth interval as a result of partial core recovery. Within Subunit IIIC, gamma-ray character suggests the presence of several thick sand beds having lithologic and grain size characteristics similar to those recovered within Core 936A-10H. Large peaks in gamma-ray values (80–90 API units) between 124 and 133 mbsf suggest intervening beds made up of clays and silty clays.

Within Unit IV, the logging data suggest that this mass-transport deposit is probably composed of multiple flow events. Cyclic variations in natural gamma-ray values suggest the presence of fining-upward cycles. Between 155 and 195 mbsf, three intervals occur in which resistivity decreases downhole, indicating a downhole increase in porosity within each interval (Fig. 37A and 37B). This porosity variation may be related to drainage of pore waters from the formation to the seafloor between individual depositional events. Alternatively, the porosity decrease may be related to grain size variations in each of the individual units, as suggested by the subtle upward increase in gamma-ray counts in these same intervals (Fig. 37A). Within the basal portion of Unit IV, an overall downhole increase in resistivity of up to 5 Ωm can be observed. This high resistivity is probably the result of indurated clay clasts and organic material within the sediment (see "Lithostratigraphy" section, this chapter). Resistivity decreases below 289 mbsf, near the base of Unit IV, then returns to the background values observed above 240 mbsf (~2 Ωm; Fig. 37B). At the base of Unit IV (294 mbsf), an additional decrease in resistivity (to 1 Ωm) is seen. This decrease may reflect the observed increase in silt-sand beds, but may also be related to undercompaction of Unit V. Indicators of undercompaction, such as a decrease in resistivity, sonic velocity, and density (Fig. 35), beneath mass flows also were observed at Sites 931, 933, and 935.

The shipboard logging data provide an initial indication of overall downhole variations of concentrations of major elements (Fig. 36). Calcium and sulfur show overall low yields, which is in agreement with laboratory analyses. A small increase in the calcium yield was observed within lithostratigraphic Unit IV between 190 and 250 mbsf, whereas sulfur shows higher yields between 190 and 220 mbsf. Post-cruise processing of the geochemical logs will allow us to transform the relative concentrations (elemental yields) into normalized oxide concentrations (see "Explanatory Notes" chapter, this volume, and processed logs at the end of this chapter).

The natural gamma-ray and the photoelectric effect (PEF) data provide a first-order estimate of the bulk mineralogy of the sediment (Fig. 38). Within Unit III, PEF is generally less than 3, except within Subunit IIIB, where it is nearly constant at 3. Th/K ratios in Unit III

**Table 11. Index properties at Site 936.**

| Core, section, interval (cm) | Depth (mbsf) | Water content (%) | Wet-bulk density ($g/cm^3$) | Grain density ($g/cm^3$) | Dry-bulk density ($g/cm^3$) | Porosity (%) | Void ratio |
|---|---|---|---|---|---|---|---|
| 155-936A- | | | | | | | |
| 1H-1, 22–24 | 0.22 | 45.6 | 1.49 | 2.78 | 0.85 | 69.4 | 2.27 |
| 1H-1, 82–84 | 0.82 | 57.5 | 1.42 | 2.71 | 0.59 | 78.2 | 3.58 |
| 1H-2, 76–78 | 2.26 | 50.6 | 1.51 | 2.79 | 0.74 | 73.6 | 2.79 |
| 1H-3, 73–75 | 3.73 | 46.6 | 1.56 | 2.79 | 0.83 | 70.3 | 2.37 |
| 1H-4, 76–78 | 5.26 | 44.9 | 1.60 | 2.76 | 0.86 | 68.7 | 2.19 |
| 1H-5, 20–22 | 6.20 | 41.1 | 1.66 | 2.78 | 0.96 | 65.5 | 1.90 |
| 2H-1, 71–73 | 7.21 | 43.3 | 1.61 | 2.77 | 0.91 | 67.4 | 2.06 |
| 2H-2, 65–67 | 8.65 | 40.9 | 1.65 | 2.72 | 0.96 | 64.7 | 1.84 |
| 2H-3, 68–70 | 10.18 | 41.5 | 1.64 | 2.72 | 0.94 | 65.3 | 1.88 |
| 2H-4, 69–71 | 11.69 | 40.0 | 1.69 | 2.74 | 0.98 | 64.1 | 1.78 |
| 2H-5, 63–65 | 13.13 | 38.4 | 1.70 | 2.70 | 1.02 | 62.2 | 1.64 |
| 2H-6, 42–44 | 14.42 | 40.4 | 1.61 | 2.70 | 0.97 | 64.1 | 1.79 |
| 2H-7, 48–50 | 15.98 | 38.7 | 1.63 | 2.77 | 1.03 | 63.1 | 1.71 |
| 3H-1, 75–77 | 16.75 | 38.3 | 1.72 | 2.77 | 1.03 | 62.6 | 1.68 |
| 3H-2, 77–79 | 18.27 | 38.1 | 1.69 | 2.70 | 1.03 | 61.8 | 1.62 |
| 3H-3, 58–60 | 19.58 | 33.9 | 1.77 | 2.69 | 1.15 | 57.5 | 1.35 |
| 3H-4, 43–45 | 20.93 | 35.0 | 1.76 | 2.75 | 1.13 | 59.1 | 1.45 |
| 3H-5, 82–84 | 22.82 | 34.2 | 1.76 | 2.72 | 1.14 | 57.9 | 1.38 |
| 3H-6, 93–95 | 24.43 | 37.9 | 1.67 | 2.75 | 1.04 | 62.0 | 1.63 |
| 3H-7, 73–75 | 25.73 | 36.8 | 1.74 | 2.75 | 1.07 | 60.9 | 1.56 |
| 4H-1, 72–74 | 26.22 | 35.7 | 1.66 | 2.69 | 1.10 | 59.3 | 1.46 |
| 4H-2, 87–89 | 27.87 | 35.5 | 1.68 | 2.73 | 1.11 | 59.4 | 1.46 |
| 4H-3, 68–70 | 29.18 | 35.2 | 1.75 | 2.72 | 1.11 | 59.0 | 1.44 |
| 4H-4, 62–64 | 30.62 | 34.0 | 1.78 | 2.71 | 1.15 | 57.7 | 1.36 |
| 4H-5, 60–62 | 32.10 | 34.2 | 1.77 | 2.73 | 1.15 | 58.1 | 1.39 |
| 4H-6, 61–63 | 33.61 | 33.9 | 1.78 | 2.71 | 1.15 | 57.5 | 1.35 |
| 4H-7, 80–82 | 35.30 | 33.8 | 1.79 | 2.76 | 1.16 | 57.9 | 1.38 |
| 5H-1, 68–70 | 35.68 | 34.1 | 1.79 | 2.77 | 1.15 | 58.3 | 1.40 |
| 5H-2, 65–67 | 37.15 | 35.4 | 1.74 | 2.71 | 1.11 | 59.1 | 1.45 |
| 5H-3, 64–66 | 38.64 | 34.9 | 1.59 | 2.78 | 1.13 | 59.2 | 1.45 |
| 5H-4, 63–65 | 40.13 | 33.4 | 1.80 | 2.72 | 1.17 | 57.1 | 1.33 |
| 5H-5, 96–98 | 41.96 | 33.9 | 1.77 | 2.70 | 1.15 | 57.5 | 1.35 |
| 5H-6, 73–75 | 43.23 | 33.4 | 1.80 | 2.76 | 1.17 | 57.5 | 1.35 |
| 5H-7, 43–45 | 44.43 | 32.7 | 1.81 | 2.76 | 1.20 | 56.6 | 1.31 |
| 6H-1, 65–67 | 45.15 | 31.8 | 1.83 | 2.75 | 1.22 | 55.6 | 1.25 |
| 6H-2, 19–21 | 46.19 | 32.1 | 1.81 | 2.69 | 1.20 | 55.3 | 1.24 |
| 6H-3, 83–85 | 48.33 | 33.0 | 1.79 | 2.69 | 1.17 | 56.4 | 1.30 |
| 6H-4, 39–41 | 49.39 | 32.5 | 1.82 | 2.74 | 1.20 | 56.3 | 1.29 |
| 6H-5, 43–45 | 50.93 | 29.8 | 1.84 | 2.69 | 1.27 | 52.7 | 1.12 |
| 6H-6, 64–66 | 52.64 | 33.0 | 1.78 | 2.68 | 1.17 | 56.2 | 1.29 |
| 6H-7, 66–68 | 54.16 | 31.9 | 1.82 | 2.71 | 1.21 | 55.3 | 1.23 |
| 7H-1, 107–109 | 55.07 | 31.1 | 1.86 | 2.74 | 1.24 | 54.7 | 1.21 |
| 7H-2, 69–71 | 56.19 | 31.4 | 1.84 | 2.71 | 1.23 | 54.8 | 1.21 |
| 7H-3, 17–19 | 57.17 | 31.8 | 1.81 | 2.69 | 1.21 | 55.1 | 1.23 |
| 7H-4, 26–28 | 58.22 | 31.0 | 1.89 | 2.76 | 1.25 | 54.7 | 1.21 |
| 7H-5, 6–8 | 59.52 | 31.7 | 1.86 | 2.75 | 1.22 | 55.6 | 1.25 |
| 7H-6, 40–42 | 61.36 | 31.9 | 1.82 | 2.71 | 1.21 | 55.3 | 1.24 |
| 7H-7, 29–31 | 62.75 | 31.3 | 1.83 | 2.69 | 1.23 | 54.5 | 1.20 |
| 8H-1, 46–48 | 63.96 | 31.3 | 1.85 | 2.77 | 1.24 | 55.2 | 1.23 |
| 8H-2, 48–50 | 65.48 | 31.1 | 1.87 | 2.76 | 1.25 | 54.9 | 1.22 |
| 8H-3, 93–95 | 67.43 | 29.7 | 1.86 | 2.70 | 1.28 | 52.7 | 1.11 |
| 8H-4, 106–108 | 69.06 | 30.1 | 1.86 | 2.71 | 1.27 | 53.2 | 1.14 |
| 8H-5, 87–89 | 70.37 | 29.9 | 1.92 | 2.78 | 1.29 | 53.6 | 1.16 |
| 8H-6, 80–82 | 71.80 | 31.2 | 1.85 | 2.70 | 1.23 | 54.4 | 1.19 |
| 8H-7, 24–26 | 72.74 | 27.6 | 1.93 | 2.71 | 1.35 | 50.2 | 1.01 |
| 8H-7, 78–80 | 73.28 | 25.6 | 1.96 | 2.68 | 1.41 | 47.4 | 0.90 |
| 9H-1, 98–100 | 73.98 | 22.5 | 2.03 | 2.71 | 1.53 | 43.5 | 0.77 |
| 9H-2, 57–59 | 75.07 | 20.7 | 2.09 | 2.73 | 1.61 | 41.0 | 0.70 |
| 10H-1, 24–26 | 82.74 | 13.7 | 2.26 | 2.71 | 1.91 | 29.5 | 0.42 |
| 10H-1, 46–48 | 82.96 | 14.6 | 2.22 | 2.67 | 1.85 | 30.8 | 0.44 |
| 10H-1, 103–105 | 83.53 | 31.5 | 1.85 | 2.68 | 1.22 | 54.6 | 1.20 |
| 10H-2, 46–48 | 84.46 | 28.4 | 1.88 | 2.70 | 1.32 | 51.0 | 1.04 |
| 10H-3, 79–81 | 86.29 | 26.1 | 1.96 | 2.75 | 1.41 | 48.7 | 0.95 |
| 13X-1, 59–61 | 106.89 | 30.6 | 1.86 | 2.71 | 1.25 | 53.8 | 1.17 |
| 13X-2, 60–62 | 108.40 | 30.3 | 1.88 | 2.74 | 1.27 | 53.8 | 1.17 |
| 13X-3, 57–59 | 109.87 | 29.7 | 1.91 | 2.78 | 1.30 | 53.3 | 1.14 |
| 13X-4, 93–95 | 111.73 | 30.1 | 1.88 | 2.78 | 1.28 | 53.8 | 1.17 |
| 14X-1, 77–79 | 116.67 | 32.0 | 1.82 | 2.70 | 1.21 | 55.4 | 1.24 |
| 17X-1, 33–35 | 145.13 | 29.9 | 1.88 | 2.77 | 1.29 | 53.6 | 1.15 |
| 17X-2, 65–67 | 146.95 | 33.1 | 1.83 | 2.76 | 1.18 | 57.2 | 1.34 |
| 17X-3, 47–49 | 148.27 | 32.5 | 1.85 | 2.77 | 1.20 | 56.6 | 1.30 |
| 17X-4, 50–52 | 149.80 | 28.9 | 1.94 | 2.75 | 1.32 | 52.1 | 1.09 |
| 18X-1, 42–44 | 154.92 | 23.9 | 2.03 | 2.77 | 1.50 | 45.9 | 0.85 |
| 18X-2, 42–44 | 156.42 | 24.2 | 2.01 | 2.76 | 1.48 | 46.2 | 0.86 |
| 18X-3, 42–44 | 157.92 | 23.3 | 2.05 | 2.76 | 1.52 | 45.0 | 0.82 |
| 18X-4, 42–44 | 159.42 | 23.1 | 2.08 | 2.75 | 1.52 | 44.7 | 0.81 |
| 18X-5, 42–44 | 160.92 | 24.5 | 1.99 | 2.71 | 1.46 | 46.2 | 0.86 |
| 18X-6, 42–44 | 162.42 | 25.8 | 1.97 | 2.71 | 1.41 | 47.9 | 0.92 |
| 18X-7, 9–11 | 163.59 | 25.2 | 1.99 | 2.76 | 1.45 | 47.6 | 0.91 |
| 19X-1, 100–102 | 165.10 | 27.7 | 1.91 | 2.72 | 1.35 | 50.3 | 1.01 |
| 19X-2, 101–103 | 166.61 | 27.0 | 1.94 | 2.75 | 1.38 | 49.7 | 0.99 |
| 19X-3, 77–79 | 167.87 | 24.0 | 1.99 | 2.72 | 1.48 | 45.6 | 0.84 |
| 19X-4, 66–68 | 169.26 | 26.5 | 1.93 | 2.73 | 1.39 | 49.0 | 0.96 |
| 19X-5, 37–39 | 170.47 | 25.4 | 1.99 | 2.78 | 1.45 | 48.0 | 0.92 |
| 19X-6, 9–11 | 171.69 | 28.1 | 1.88 | 2.72 | 1.34 | 50.9 | 1.04 |
| 20X-1, 41–43 | 174.21 | 30.2 | 1.84 | 2.71 | 1.26 | 53.3 | 1.14 |
| 20X-2, 87–89 | 176.17 | 24.4 | 1.99 | 2.76 | 1.48 | 46.5 | 0.87 |

**Table 11 (continued).**

| Core, section, interval (cm) | Depth (mbsf) | Water content (%) | Wet-bulk density ($g/cm^3$) | Grain density ($g/cm^3$) | Dry-bulk density ($g/cm^3$) | Porosity (%) | Void ratio |
|---|---|---|---|---|---|---|---|
| 20X-3, 99–101 | 177.79 | 28.1 | 1.90 | 2.71 | 1.33 | 50.9 | 1.04 |
| 20X-4, 45–47 | 178.75 | 23.0 | 2.02 | 2.71 | 1.51 | 44.2 | 0.79 |
| 20X-5, 73–75 | 180.53 | 23.0 | 2.02 | 2.71 | 1.52 | 44.2 | 0.79 |
| 21X-1, 75–77 | 184.15 | 24.6 | 1.98 | 2.72 | 1.46 | 46.4 | 0.87 |
| 21X-2, 76–78 | 185.66 | 22.2 | 2.03 | 2.70 | 1.54 | 42.9 | 0.75 |
| 21X-3, 78–80 | 187.18 | 24.5 | 1.97 | 2.70 | 1.45 | 46.1 | 0.86 |
| 21X-4, 83–85 | 188.73 | 24.6 | 2.00 | 2.76 | 1.47 | 46.7 | 0.88 |
| 21X-5, 81–83 | 190.21 | 23.5 | 2.02 | 2.75 | 1.51 | 45.2 | 0.82 |
| 21X-6, 13–15 | 191.03 | 24.3 | 2.01 | 2.74 | 1.48 | 46.2 | 0.86 |
| 22X-1, 76–78 | 193.86 | 25.2 | 1.97 | 2.75 | 1.45 | 47.4 | 0.90 |
| 22X-2, 78–80 | 195.38 | 24.0 | 2.00 | 2.72 | 1.48 | 45.5 | 0.84 |
| 22X-3, 79–81 | 196.89 | 24.2 | 1.99 | 2.72 | 1.47 | 45.8 | 0.85 |
| 22X-4, 77–79 | 198.37 | 23.4 | 2.04 | 2.77 | 1.52 | 45.3 | 0.83 |
| 22X-5, 24–26 | 199.34 | 22.2 | 2.04 | 2.73 | 1.55 | 43.2 | 0.76 |
| 23X-1, 85–87 | 203.65 | 22.9 | 2.04 | 2.78 | 1.54 | 44.7 | 0.81 |
| 23X-2, 85–87 | 205.15 | 23.3 | 2.00 | 2.72 | 1.50 | 44.6 | 0.81 |
| 23X-3, 80–82 | 206.60 | 24.7 | 2.00 | 2.78 | 1.47 | 47.1 | 0.89 |
| 23X-4, 73–75 | 208.03 | 23.9 | 2.02 | 2.77 | 1.50 | 45.9 | 0.85 |
| 23X-5, 61–63 | 209.41 | 22.9 | 2.02 | 2.72 | 1.52 | 44.1 | 0.79 |
| 24X-1, 82–84 | 213.32 | 24.7 | 1.99 | 2.74 | 1.46 | 46.7 | 0.88 |
| 24X-2, 121–123 | 215.21 | 23.6 | 2.03 | 2.77 | 1.51 | 45.5 | 0.83 |
| 25X-1, 90–92 | 223.00 | 24.1 | 2.01 | 2.75 | 1.49 | 46.0 | 0.85 |
| 25X-2, 85–87 | 224.45 | 23.4 | 2.01 | 2.71 | 1.50 | 44.7 | 0.81 |
| 25X-3, 90–92 | 226.00 | 22.6 | 2.03 | 2.73 | 1.54 | 43.8 | 0.78 |
| 25X-4, 99–101 | 227.59 | 22.4 | 2.04 | 2.71 | 1.54 | 43.2 | 0.76 |
| 25X-5, 87–89 | 228.97 | 22.6 | 2.05 | 2.77 | 1.55 | 44.2 | 0.79 |
| 26X-1, 77–79 | 232.47 | 21.7 | 2.09 | 2.77 | 1.59 | 42.8 | 0.75 |
| 26X-2, 79–81 | 233.99 | 21.4 | 2.11 | 2.76 | 1.59 | 42.3 | 0.73 |
| 26X-3, 87–89 | 235.57 | 21.1 | 2.10 | 2.73 | 1.59 | 41.6 | 0.71 |
| 26X-4, 84–86 | 237.04 | 20.7 | 2.12 | 2.77 | 1.62 | 41.4 | 0.71 |
| 26X-5, 79–81 | 238.49 | 20.4 | 2.12 | 2.77 | 1.64 | 40.9 | 0.69 |
| 26X-6, 104–106 | 240.24 | 21.3 | 2.07 | 2.70 | 1.57 | 41.7 | 0.71 |
| 26X-7, 12–14 | 240.82 | 21.4 | 2.10 | 2.77 | 1.60 | 42.4 | 0.74 |
| 27X-1, 24–26 | 241.64 | 20.9 | 2.13 | 2.77 | 1.62 | 41.7 | 0.71 |
| 27X-2, 24–26 | 243.14 | 21.2 | 2.11 | 2.77 | 1.60 | 42.1 | 0.73 |
| 27X-3, 24–26 | 244.64 | 20.4 | 2.10 | 2.71 | 1.61 | 40.4 | 0.68 |
| 27X-4, 23–25 | 246.13 | 21.5 | 2.09 | 2.77 | 1.59 | 42.5 | 0.74 |
| 27X-5, 24–26 | 247.64 | 21.1 | 2.08 | 2.71 | 1.59 | 41.4 | 0.71 |
| 27X-6, 24–26 | 249.14 | 22.1 | 2.07 | 2.76 | 1.57 | 43.3 | 0.77 |
| 28X-1, 130–132 | 252.40 | 21.3 | 2.09 | 2.77 | 1.60 | 42.3 | 0.73 |
| 28X-2, 76–78 | 253.36 | 23.4 | 2.02 | 2.72 | 1.50 | 44.7 | 0.81 |
| 28X-3, 96–98 | 255.06 | 23.1 | 2.05 | 2.71 | 1.51 | 44.3 | 0.80 |
| 28X-4, 94–96 | 256.54 | 19.5 | 2.13 | 2.72 | 1.65 | 39.1 | 0.64 |
| 28X-5, 66–68 | 257.76 | 20.8 | 2.10 | 2.70 | 1.60 | 40.9 | 0.69 |
| 28X-6, 32–34 | 258.92 | 22.8 | 2.04 | 2.71 | 1.52 | 43.8 | 0.78 |
| 29X-1, 109–111 | 261.79 | 22.4 | 2.04 | 2.73 | 1.54 | 43.4 | 0.77 |
| 29X-2, 109–111 | 263.29 | 21.3 | 2.10 | 2.77 | 1.60 | 42.3 | 0.73 |
| 29X-3, 109–111 | 264.79 | 21.1 | 2.10 | 2.76 | 1.61 | 41.9 | 0.72 |
| 29X-4, 109–111 | 266.29 | 20.9 | 2.13 | 2.79 | 1.62 | 41.8 | 0.72 |
| 29X-5, 120–122 | 267.90 | 20.2 | 2.12 | 2.73 | 1.63 | 40.2 | 0.67 |
| 30X-1, 126–128 | 271.66 | 21.1 | 2.00 | 2.70 | 1.58 | 41.4 | 0.71 |
| 30X-2, 104–106 | 272.94 | 14.7 | 1.94 | 2.71 | 1.87 | 31.3 | 0.46 |
| 30X-3, 101–103 | 274.41 | 20.9 | 2.11 | 2.76 | 1.61 | 41.6 | 0.71 |
| 30X-4, 114–116 | 276.04 | 20.7 | 2.10 | 2.72 | 1.61 | 40.9 | 0.69 |
| 30X-5, 78–80 | 277.18 | 20.3 | 2.11 | 2.76 | 1.64 | 40.8 | 0.69 |
| 30X-6, 54–56 | 278.44 | 20.4 | 2.10 | 2.71 | 1.61 | 40.5 | 0.68 |
| 31X-1, 96–98 | 280.86 | 20.9 | 2.11 | 2.75 | 1.61 | 41.5 | 0.71 |
| 31X-2, 98–100 | 282.38 | 20.5 | 2.11 | 2.71 | 1.61 | 40.6 | 0.68 |
| 31X-3, 53–55 | 283.43 | 19.7 | 2.15 | 2.77 | 1.67 | 40.0 | 0.67 |
| 31X-4, 52–54 | 284.92 | 20.9 | 2.09 | 2.75 | 1.61 | 41.4 | 0.71 |
| 31X-5, 25–27 | 286.15 | 20.1 | 2.11 | 2.71 | 1.63 | 40.0 | 0.67 |
| 32X-1, 94–96 | 290.34 | 19.8 | 2.13 | 2.77 | 1.66 | 40.0 | 0.67 |
| 32X-2, 130–132 | 292.20 | 19.4 | 2.15 | 2.76 | 1.68 | 39.3 | 0.65 |
| 32X-3, 92–94 | 293.32 | 19.8 | 2.13 | 2.76 | 1.66 | 40.0 | 0.67 |
| 32X-4, 54–56 | 294.44 | 23.9 | 2.00 | 2.71 | 1.48 | 45.3 | 0.83 |
| 32X-5, 69–71 | 296.09 | 23.7 | 2.03 | 2.78 | 1.51 | 45.8 | 0.84 |
| 32X-6, 88–90 | 297.78 | 23.0 | 2.02 | 2.73 | 1.52 | 44.2 | 0.79 |
| 32X-7, 26–28 | 298.66 | 22.4 | 2.09 | 2.79 | 1.56 | 44.0 | 0.79 |
| 33X-1, 78–80 | 299.78 | 25.4 | 1.98 | 2.78 | 1.45 | 48.0 | 0.92 |
| 33X-2, 95–97 | 301.45 | 24.3 | 1.99 | 2.73 | 1.47 | 46.1 | 0.86 |
| 33X-3, 104–106 | 303.04 | 24.9 | 2.00 | 2.76 | 1.46 | 47.1 | 0.89 |
| 33X-4, 7–9 | 303.57 | 24.3 | 2.00 | 2.74 | 1.47 | 46.2 | 0.86 |
| 33X-5, 96–98 | 305.96 | 24.2 | 2.01 | 2.79 | 1.49 | 46.4 | 0.87 |
| 33X-6, 45–47 | 306.95 | 22.2 | 2.07 | 2.76 | 1.56 | 43.5 | 0.77 |
| 35X-1, 85–87 | 319.05 | 31.1 | 1.83 | 2.72 | 1.24 | 54.6 | 1.20 |
| 35X-1, 118–120 | 319.38 | 27.5 | 1.93 | 2.72 | 1.36 | 50.1 | 1.00 |
| 41X-1, 110–112 | 377.10 | 25.8 | 1.98 | 2.80 | 1.44 | 48.7 | 0.95 |
| 41X-2, 94–96 | 378.44 | 21.7 | 2.09 | 2.78 | 1.59 | 42.9 | 0.75 |
| 41X-3, 111–113 | 380.11 | 23.8 | 2.02 | 2.73 | 1.49 | 45.4 | 0.83 |
| 41X-4, 71–73 | 381.21 | 22.3 | 2.05 | 2.76 | 1.56 | 43.6 | 0.77 |
| 42X-1, 40–42 | 386.10 | 24.5 | 2.00 | 2.71 | 1.46 | 46.2 | 0.86 |
| 42X-2, 131–133 | 388.51 | 20.6 | 2.12 | 2.72 | 1.61 | 40.8 | 0.69 |
| 43X-1, 47–49 | 395.77 | 20.1 | 2.12 | 2.72 | 1.63 | 40.0 | 0.67 |
| 43X-2, 63–65 | 396.77 | 20.0 | 2.13 | 2.70 | 1.63 | 39.7 | 0.66 |
| 43X-3, 41–43 | 398.05 | 19.2 | 2.16 | 2.73 | 1.67 | 38.8 | 0.63 |
| 43X-4, 39–41 | 399.53 | 20.0 | 2.20 | 2.76 | 1.65 | 40.2 | 0.67 |
| 43X-5, 76–78 | 401.40 | 15.6 | 2.28 | 2.73 | 1.83 | 33.0 | 0.49 |
| 43X-6, 35–37 | 402.49 | 15.6 | 2.28 | 2.73 | 1.83 | 32.9 | 0.49 |

Table 11 (continued).

| Core, section, interval (cm) | Depth (mbsf) | Water content (%) | Wet-bulk density (g/cm$^3$) | Grain density (g/cm$^3$) | Dry-bulk density (g/cm$^3$) | Porosity (%) | Void ratio |
|---|---|---|---|---|---|---|---|
| 43X-7, 37–39 | 404.01 | 16.3 | 2.24 | 2.75 | 1.80 | 34.4 | 0.52 |
| 44X-1, 39–41 | 405.39 | 16.3 | 2.20 | 2.97 | 1.90 | 36.1 | 0.57 |
| 44X-1, 95–97 | 405.95 | 24.2 | 2.11 | 2.79 | 1.49 | 46.4 | 0.87 |
| 44X-2, 61–63 | 407.11 | 24.3 | 2.06 | 2.72 | 1.47 | 46.0 | 0.85 |
| 44X-3, 15–17 | 408.15 | 25.1 | 2.00 | 2.73 | 1.44 | 47.2 | 0.89 |
| 45X-1, 30–32 | 414.90 | 22.8 | 2.04 | 2.72 | 1.53 | 43.9 | 0.78 |
| 45X-2, 95–97 | 416.29 | 20.8 | 2.15 | 2.73 | 1.61 | 41.2 | 0.70 |
| 45X-3, 50–52 | 417.34 | 22.2 | 2.09 | 2.76 | 1.56 | 43.5 | 0.77 |
| 45X-4, 106–108 | 419.40 | 24.0 | 2.01 | 2.70 | 1.48 | 45.4 | 0.83 |
| 45X-6, 106–108 | 421.09 | 22.1 | 2.09 | 2.75 | 1.56 | 43.2 | 0.76 |
| 45X-7, 32–34 | 421.75 | 22.3 | 2.07 | 2.72 | 1.54 | 43.2 | 0.76 |
| 46X-1, 20–22 | 424.40 | 21.8 | 2.06 | 2.70 | 1.56 | 42.3 | 0.73 |

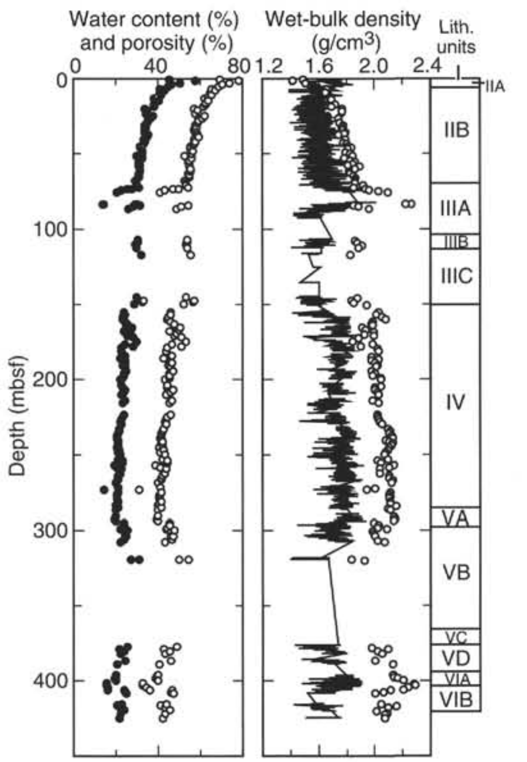


Figure 31. Water content (solid circles) and porosity (open circles), and wet-bulk density as determined for discrete samples and by the GRAPE (line) in Hole 936A.

are also relatively low, ranging from 3 to 5. An abrupt increase in PEF values from 3 at 160 mbsf to 3.2 at 290 mbsf, was observed in lithostratigraphic Unit IV. This change indicates that Unit III is enriched in mica and/or illite, compared to the apparently higher kaolinite and/or montmorillonite content in Unit IV (Fig. 38). Within Unit IV, Th/K ratios average 5.5 and vary between 4 and 7. These small-scale variations suggest changing proportions of kaolinite, illite, and montmorillonite within the mass-flow deposit. Near the top of Subunit VA (297–302 mbsf), two pronounced PEF peaks of up to about 4.5 correlate with peaks of the Th/K ratio. These peaks appear to correspond to clay-rich zones and may suggest an enrichment in relatively unstable chlorite.

Low Th/K ratios may correspond to an enrichment in illite and micas with respect to kaolinite and montmorillonite (see Fig. 25 of "Site 933" chapter, this volume). A preliminary comparison with shipboard XRD analyses shows that the relative concentrations of mica + illite vs. kaolinite of samples do not correlate well with the gamma-ray data (Fig. 38; "Lithostratigraphy" section, this chapter). Shipboard samples were preferentially taken in silt beds and are unlikely to be representative of the larger volume measured by the gamma-ray tool. Detailed analyses of the clay mineral composition in conjunction with mineralogic inversion of the geochemical logs are needed to quantify the temporal variation of clay mineral influx to the fan.

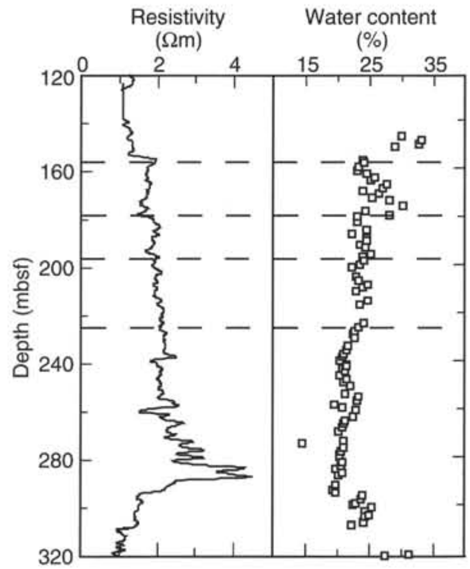


Figure 32. Resistivity from the borehole IMPH log and water content between 120 and 320 mbsf in lithologic Unit IV, illustrating suggested breaks in debris-flow deposits in the upper part of Unit IV (dashed horizontal lines).

## Formation MicroScanner

Preliminary analysis of the FMS data indicates that beds up to 1 to 2 m thick having apparent grading occur within the lower portion of Unit III. The data also show irregular bed boundaries and clastlike features within Unit IV.

Orthogonal FMS caliper measurements show that the borehole was markedly elliptical within Unit III and nearly circular within Unit IV (Fig. 39). In Unit III, the short axis of the ellipse is approximately the same size as the bit diameter; the long axis is about 15% larger. Similar to that observed at Sites 931, 933 and 935, the orientation of the long axis is approximately parallel to the bathymetric contours at the site, which suggests a relationship between the topographic gradient and the orientation of the maximum horizontal stress.

**Table 12. Undrained shear strength at Site 936.**

| Core, section, interval (cm) | Depth (mbsf) | Peak undrained shear strength (kPa) | Residual undrained shear strength (kPa) | Unconfined compressive strength* (kPa) |
|---|---|---|---|---|
| 155-936A- | | | | |
| 1H-1, 23 | 0.23 | 7.2 | 4.7 | |
| 1H-1, 83 | 0.83 | 7.8 | 5.9 | |
| 1H-2, 77 | 2.27 | 6.2 | 4.5 | |
| 1H-3, 73 | 3.73 | 9.0 | 6.7 | |
| 1H-4, 77 | 5.27 | 7.9 | 6.2 | |
| 1H-5, 21 | 6.21 | 5.1 | 3.9 | |
| 2H-1, 72 | 7.22 | 7.3 | 5.6 | |
| 2H-2, 67 | 8.67 | 7.9 | 5.6 | |
| 2H-3, 69 | 10.19 | 9.5 | 7.3 | |
| 2H-4, 69 | 11.69 | 12.3 | 9.0 | |
| 2H-5, 64 | 13.14 | 9.5 | 6.7 | |
| 2H-6, 42 | 14.42 | 10.7 | 7.9 | |
| 2H-7, 49 | 15.99 | 11.2 | 9.0 | |
| 3H-1, 75 | 16.75 | 15.2 | 11.2 | |
| 3H-2, 78 | 18.28 | 11.2 | 7.9 | |
| 3H-3, 58 | 19.58 | 14.0 | 9.5 | |
| 3H-4, 44 | 20.94 | 16.8 | 11.2 | |
| 3H-5, 82 | 22.82 | 12.3 | 6.7 | |
| 3H-6, 92 | 24.42 | 14.0 | 11.8 | |
| 3H-7, 72 | 25.72 | 14.0 | 11.2 | |
| 4H-1, 71 | 26.21 | 21.3 | 15.7 | |
| 4H-2, 88 | 27.88 | 15.7 | 12.3 | |
| 4H-3, 68 | 29.18 | 21.9 | 15.2 | |
| 4H-4, 62 | 30.62 | 23.0 | 15.7 | |
| 4H-5, 61 | 32.11 | 21.3 | 12.9 | |
| 4H-6, 62 | 33.62 | 20.2 | 11.8 | |
| 4H-7, 81 | 35.31 | 15.7 | 11.8 | |
| 5H-1, 81 | 35.81 | 25.8 | 18.5 | |
| 5H-2, 65 | 37.15 | 30.3 | 21.3 | |
| 5H-3, 65 | 38.65 | 30.9 | 19.1 | |
| 5H-4, 66 | 40.16 | 37.0 | 24.7 | |
| 5H-5, 98 | 41.98 | 32.6 | 21.9 | |
| 5H-6, 74 | 43.24 | 30.3 | 19.6 | |
| 5H-7, 44 | 44.44 | 29.2 | 19.1 | |
| 6H-1, 63 | 45.13 | 29.2 | 19.6 | |
| 6H-2, 19 | 46.19 | 27.5 | 19.1 | |
| 6H-3, 83 | 48.33 | 43.2 | 29.2 | |
| 6H-4, 40 | 49.40 | 29.2 | 19.1 | |
| 6H-5, 43 | 50.93 | 19.6 | 12.9 | |
| 7H-1, 113 | 55.13 | 36.2 | 21.2 | |
| 7H-2, 70 | 56.20 | 32.2 | 20.3 | |
| 7H-3, 31 | 57.31 | 26.6 | 17.6 | |
| 7H-4, 27 | 58.23 | 24.6 | 16.1 | |
| 7H-5, 7 | 59.53 | 29.1 | 17.3 | |
| 7H-6, 41 | 61.37 | 24.6 | 15.5 | |
| 7H-7, 30 | 62.76 | 35.4 | 21.1 | |
| 8H-1, 47 | 63.97 | 31.7 | 19.7 | |
| 8H-2, 49 | 65.49 | 26.6 | 15.7 | |
| 8H-3, 94 | 67.44 | 38.2 | 21.3 | |
| 8H-4, 107 | 69.07 | 35.6 | 14.9 | |
| 8H-5, 88 | 70.38 | 33.7 | 21.9 | |
| 8H-6, 81 | 71.81 | 37.6 | 16.9 | |
| 8H-7, 25 | 72.75 | 47.0 | 20.5 | |
| 9H-1, 99 | 73.99 | 39.0 | 25.6 | |
| 9H-2, 58 | 75.08 | 34.5 | 22.7 | |
| 10H-1, 104 | 83.54 | 35.4 | 19.6 | |
| 13X-1, 60 | 106.90 | 36.2 | 21.6 | |
| 13X-2, 61 | 108.41 | 43.8 | 20.1 | |
| 13X-3, 58 | 109.88 | 51.5 | 22.6 | |
| 13X-4, 94 | 111.74 | 60.3 | 23.1 | |
| 14X-1, 78 | 116.68 | 26.6 | 15.7 | |
| 17X-1, 34 | 145.14 | 38.5 | 20.8 | 68.6 |
| 17X-2, 66 | 146.96 | 41.3 | 20.9 | 93.2 |
| 17X-3, 46 | 148.26 | 81.5 | 35.3 | 171.6 |
| 17X-4, 51 | 149.81 | 68.6 | 36.4 | 171.6 |
| 18X-1, 43 | 154.93 | 69.6 | 39.0 | 171.6 |
| 18X-2, 43 | 156.43 | 93.1 | 51.6 | 127.6 |
| 18X-3, 43 | 157.93 | 90.0 | 45.4 | 215.8 |
| 18X-4, 42 | 159.42 | 103.9 | 58.0 | 211.0 |
| 18X-5, 43 | 160.93 | 96.7 | 47.7 | 235.4 |
| 18X-6, 43 | 162.43 | 133.7 | 66.7 | 274.6 |
| 18X-7, 10 | 163.60 | 75.1 | 43.3 | 225.6 |
| 19X-1, 101 | 165.11 | 80.4 | 46.1 | 186.4 |
| 19X-2, 101 | 166.61 | 96.4 | 55.4 | 215.8 |
| 19X-3, 78 | 167.88 | 95.5 | 55.7 | 235.4 |
| 19X-4, 68 | 169.28 | 91.1 | 50.9 | 181.4 |
| 19X-5, 38 | 170.48 | 115.8 | 62.9 | 245.2 |
| 19X-6, 10 | 171.70 | 84.9 | 49.1 | 230.6 |
| 20X-1, 42 | 174.22 | 66.3 | 34.9 | 186.4 |
| 20X-2, 87 | 176.17 | 57.5 | 32.7 | 176.6 |
| 20X-3, 100 | 177.80 | 48.6 | 22.4 | 225.6 |
| 20X-4, 46 | 178.76 | 114.0 | 58.3 | 260.0 |
| 20X-5, 74 | 180.54 | 87.5 | 48.7 | 235.4 |
| 21X-1, 75 | 184.15 | 101.7 | 45.7 | 264.8 |
| 21X-2, 77 | 185.67 | 81.3 | 50.0 | 206.0 |
| 21X-3, 79 | 187.19 | 108.7 | 58.4 | 250.2 |
| 21X-4, 85 | 188.75 | 97.2 | 53.9 | 279.6 |
| 21X-5, 82 | 190.22 | 141.4 | 80.3 | 353.2 |
| 21X-6, 15 | 191.05 | 101.7 | 52.3 | 294.4 |
| 22X-1, 75 | 193.85 | 83.1 | 48.8 | 220.8 |
| 22X-2, 79 | 195.39 | 115.8 | 70.8 | 264.8 |
| 22X-3, 87 | 196.97 | 118.5 | 70.5 | 269.8 |
| 22X-4, 77 | 198.37 | 108.7 | 65.8 | 269.8 |
| 22X-5, 24 | 199.34 | 94.6 | 53.8 | 304.2 |
| 23X-1, 86 | 203.66 | 74.3 | 42.9 | 215.8 |
| 23X-2, 87 | 205.17 | 69.8 | 44.7 | 186.4 |
| 23X-3, 80 | 206.60 | 75.1 | 42.1 | 240.4 |
| 23X-4, 74 | 208.04 | 79.6 | 46.8 | 186.4 |
| 23X-5, 61 | 209.41 | 113.2 | 61.2 | 274.6 |
| 24X-1, 84 | 213.34 | 83.1 | 45.5 | 220.8 |
| 24X-2, 123 | 215.23 | 77.8 | 45.6 | 225.6 |
| 25X-1, 92 | 223.02 | 66.3 | 40.1 | 201.2 |
| 25X-2, 85 | 224.45 | 78.7 | 43.7 | 245.2 |
| 25X-3, 90 | 226.00 | 99.0 | 54.6 | 274.6 |
| 25X-4, 99 | 227.59 | 76.0 | 38.6 | 196.2 |
| 25X-5, 86 | 228.96 | 86.6 | 47.5 | 269.8 |
| 26X-1, 78 | 232.48 | 138.8 | 67.7 | 255.0 |
| 26X-2, 80 | 234.00 | 157.4 | 86.6 | 264.8 |
| 26X-3, 88 | 235.58 | 175.0 | 94.6 | 348.2 |
| 26X-4, 85 | 237.05 | 184.8 | 96.9 | 363.0 |
| 26X-5, 80 | 238.50 | 177.7 | 91.2 | 358.0 |
| 26X-6, 105 | 240.25 | 136.1 | 79.2 | 314.0 |
| 26X-7, 3 | 240.83 | 164.4 | 87.6 | 392.4 |
| 27X-1, 45 | 241.85 | | | 421.8 |
| 27X-2, 25 | 243.15 | 133.5 | 75.3 | 318.8 |
| 27X-3, 25 | 244.65 | 198.0 | 95.9 | 431.6 |
| 27X-4, 24 | 246.14 | 131.7 | 72.3 | 363.0 |
| 27X-5, 25 | 247.65 | 131.7 | 75.4 | 367.8 |
| 27X-6, 25 | 249.15 | 128.2 | 71.0 | 338.4 |
| 28X-1, 131 | 252.41 | 75.1 | 43.6 | 181.4 |
| 28X-2, 77 | 253.37 | 84.9 | 36.4 | 230.6 |
| 28X-3, 97 | 255.07 | 128.2 | 68.7 | 250.2 |
| 28X-4, 95 | 256.55 | 79.6 | 41.5 | 255.0 |
| 28X-4, 117 | 256.77 | 147.6 | 81.6 | 264.8 |
| 28X-5, 67 | 257.77 | 168.0 | 91.7 | 338.4 |
| 28X-6, 33 | 258.93 | 183.0 | 81.6 | 372.8 |
| 29X-1, 110 | 261.80 | 135.3 | 82.1 | 294.4 |
| 29X-2, 110 | 263.30 | 158.2 | 90.3 | 363.0 |
| 29X-3, 110 | 264.80 | 161.8 | 84.4 | 333.6 |
| 29X-4, 110 | 266.30 | 191.8 | 98.8 | 412.0 |
| 29X-5, 121 | 267.91 | 231.6 | 115.4 | 392.4 |
| 30X-1, 127 | 271.67 | 147.6 | 81.9 | 260.0 |
| 30X-2, 105 | 272.95 | 137.0 | 71.7 | 240.4 |
| 30X-3, 102 | 274.42 | 132.6 | 76.6 | 284.4 |
| 30X-4, 115 | 276.05 | 139.7 | 83.1 | 264.8 |
| 30X-5, 79 | 277.19 | 193.6 | 96.8 | 289.4 |
| 30X-6, 55 | 278.45 | 148.5 | 81.6 | 284.4 |
| 31X-1, 97 | 280.87 | 98.1 | 56.3 | 235.4 |
| 31X-2, 99 | 282.39 | 143.2 | 78.1 | 255.0 |
| 31X-3, 54 | 283.44 | 162.7 | 79.0 | 338.4 |
| 31X-4, 53 | 284.93 | 176.8 | 89.2 | 358.0 |
| 31X-5, 26 | 286.16 | 149.4 | 79.0 | 309.0 |
| 32X-1, 95 | 290.35 | 194.5 | 102.6 | 421.8 |
| 32X-2, 131 | 292.21 | 195.4 | 100.2 | 407.2 |
| 32X-3, 93 | 293.33 | 205.1 | 101.0 | 431.6 |
| 32X-4, 55 | 294.45 | 132.6 | 69.3 | 240.4 |
| 32X-5, 70 | 296.10 | 114.9 | 53.6 | 225.6 |
| 32X-6, 89 | 297.79 | 168.0 | 73.8 | 328.6 |
| 32X-7, 27 | 298.67 | 140.6 | 71.1 | 431.6 |
| 33X-1, 79 | 299.79 | 69.0 | 26.6 | 166.8 |
| 33X-2, 95 | 301.45 | 94.6 | 51.3 | 201.2 |
| 33X-3, 104 | 303.04 | 70.7 | 42.8 | 235.4 |
| 33X-4, 8 | 303.58 | 126.4 | 68.2 | 318.8 |
| 33X-5, 96 | 305.96 | 161.8 | 79.1 | 353.2 |
| 33X-6, 45 | 306.95 | 256.4 | 127.6 | >440 |
| 35X-1, 118 | 319.38 | | | 127.6 |
| 41X-1, 111 | 377.11 | | | 108.0 |
| 41X-2, 97 | 378.47 | | | 274.6 |
| 41X-3, 112 | 380.12 | 90.2 | 45.4 | 304.2 |
| 41X-4, 72 | 381.22 | 160.9 | 77.2 | >440 |
| 42X-1, 42 | 386.12 | 62.8 | 35.9 | 269.8 |
| 42X-2, 132 | 388.52 | 198.0 | 89.4 | >440 |
| 43X-1, 48 | 395.78 | 182.1 | 82.3 | >440 |
| 43X-2, 64 | 396.78 | >240 | | >440 |
| 43X-3, 42 | 398.06 | >240 | | >440 |
| 43X-4, 40 | 399.54 | | | 431.6 |
| 43X-5, 77 | 401.41 | | | 353.2 |
| 43X-6, 36 | 402.50 | | | >440 |
| 43X-7, 38 | 404.02 | | | 328.6 |

Table 12 (continued).

| Core, section, interval (cm) | Depth (mbsf) | Peak undrained shear strength (kPa) | Residual undrained shear strength (kPa) | Unconfined compressive strength* (kPa) |
|---|---|---|---|---|
| 44X-1, 96 | 405.96 | | | 225.6 |
| 44X-2, 62 | 407.12 | | | 323.8 |
| 44X-3, 16 | 408.16 | | | 402.2 |
| 45X-1, 31 | 414.91 | | | >440 |
| 45X-2, 96 | 416.30 | | | 294.4 |
| 45X-3, 51 | 417.35 | | | 318.8 |
| 45X-4, 107 | 419.41 | | | 196.2 |
| 46X-1, 21 | 424.41 | | | 318.8 |

Note: *Unconfined compressive strength ($q_u$) can be used to approximate undrained shear strength ($S_u$) by the relationship $q_u = 2S_u$.

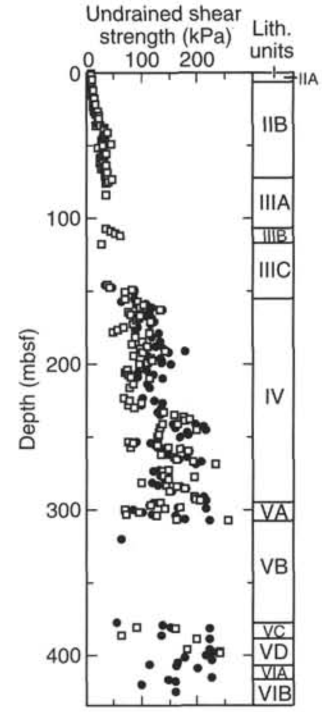


Figure 33. Undrained shear strength (open squares) and assumed undrained shear strength derived from unconfined compressive strength (solid circles) in Hole 936A.

## Borehole Temperature

In Figure 40, we illustrate the results from the two TLT runs. The downgoing logging run on the geochemical string is not displayed because the tool descended at a much faster speed into the hole than occurred during the downgoing run of the Quad-combination tool. All records show a downhole temperature increase to about 200 or 250 mbsf, then a decrease to the bottom of the logged interval (Fig. 40). Superimposed on these large-scale variations, we noted about five or six distinct short intervals of increased borehole temperature during both logging runs (~0.1°–0.2°C during first run) that are possibly related to advection of formation water. These intervals appear to have been offset about 20 m upward during the GLT run, probably the result of rising convection in the borehole. Previous deployments of the TLT commonly show that borehole temperature is cooler than formation temperatures at depth in the hole. Comparison with the ADARA and WSTP measurements shows that borehole temperatures in the interval from 0 to 100 mbsf were warmer than the "formation" values. The notable decrease in temperature below ~210 mbsf, recorded during the GLT run, may indicate introduction of relatively warmer, advective, formation fluids above ~210 to 240 mbsf into the borehole. Whether this phenomenon is associated with seawater circulation within the borehole or with advection at deeper levels is presently unclear.

# CORE-SEISMIC INTEGRATION

Hole 936A penetrated the Amazon/Brown Channel-levee systems, Unit R, the Red Channel-levee System of the Middle Levee Complex, and into the Gold Channel-levee System of the Lower Levee Complex (Manley and Flood, 1988). Five seismic-facies units are identified on the 3.5-kHz (Fig. 3) and water-gun seismic profiles (1623UTC on 22 April 1994 during Leg 155; Fig. 41). Seismic-facies Unit 1 is classified using 3.5-kHz profiles, whereas Units 2–5 are classified from the water-gun profiles (Fig. 42). Several prominent reflections are observed at the boundaries between seismic-facies units that occur at 90, 210, 350, and 450 ms.

Preliminary correlation between the seismic-facies units and the lithologic units (see "Lithostratigraphy" section, this chapter) was made by using the time-depth relationship determined at Site 931 (Fig. 37, "Site 931" chapter, this volume). Seismic-facies Unit 1 (0 to 90 ms) is characterized by moderate-amplitude, continuous, slightly divergent reflections returned from sediment of the Amazon/Brown Channel-levee System (Fig. 42). Seismic-facies Unit 1 correlates with lithologic Units I and II, which are composed of hemipelagic silty clay that grades downward into silty clay with laminae and beds of silt and fine sand. A high-amplitude reflection at 12 ms on the 3.5-kHz profile corresponds with the interface between Subunits IIA and IIB at 7 mbsf, and marks the first occurrence of silt laminae and silt and fine sand beds within Subunit IIB.

Seismic-facies Unit 2 exhibits high-amplitude, subparallel, irregular to angular reflections (90 to 210 ms), and represents the HARP unit(s) associated with the Amazon/Brown and older channel-levee systems. This seismic-facies unit correlates to lithologic Unit III, which is composed of thin- to medium-bedded silt and fine sand turbidites (Subunit IIIB) overlain by thick beds of sand and pebbly sand, and some thin-bedded turbidites (Subunits IIIA and IIIC).

A good correlation exists between the chaotic to hummocky reflections of seismic-facies Unit 3 (Unit R) and the observed mass-transport deposits of lithologic Unit IV, which are composed of muddy debris flows and possibly slumps. High-amplitude, discontinuous subparallel reflections from 350 to 450 ms characterize seismic-facies Unit 4. These reflections correlate with the lower 10 m of lithologic Unit IV, all of Subunit VA, and most of Subunit VB (where recovery was only 4%), which are composed of thin- to medium-bedded silt and fine sand turbidites and thick-bedded coarse sand and pebbly sand. Seismic-facies Unit 4 encompasses the distal edge of the Red Channel-levee System (Middle Levee Complex), although the reflection pattern here is distinctly different from that of other channel-levee systems sampled. The lower-amplitude, continuous divergent reflections characteristic of seismic-facies Unit 5 originate from the overbank silt and fine sand turbidite deposits of lithologic Unit VI and Subunit VC, and the muddy debris-flow deposits of Subunit VD within the Gold Channel-levee System of the Lower Levee Complex (Fig. 42).

## Synthetic Seismogram

Velocity and density profiles were determined between 67 and 320 mbsf using the LSS and downhole logging data. A synthetic seismogram (Fig. 43) was produced using the two-way traveltime between the seafloor and the first log data (67 mbsf) based on an

Table 13. Electrical resistivity at Site 936.

| Core, section, interval (cm) | Depth (mbsf) | Longitudinal resistivity (Ωm) | Transverse resistivity (Ωm) |
|---|---|---|---|
| 155-936A- | | | |
| 1H-1, 23 | 0.23 | 0.250 | 0.244 |
| 1H-1, 83 | 0.83 | 0.207 | 0.197 |
| 1H-2, 75 | 2.25 | 0.231 | 0.218 |
| 1H-3, 73 | 3.73 | 0.230 | 0.240 |
| 1H-4, 77 | 5.27 | 0.286 | 0.273 |
| 1H-5, 21 | 6.21 | 0.289 | 0.274 |
| 2H-1, 71 | 7.21 | 0.290 | 0.277 |
| 2H-2, 67 | 8.67 | 0.302 | 0.301 |
| 2H-3, 69 | 10.19 | 0.291 | 0.288 |
| 2H-4, 69 | 11.69 | 0.303 | 0.288 |
| 2H-5, 64 | 13.14 | 0.299 | 0.289 |
| 2H-6, 42 | 14.42 | 0.272 | 0.261 |
| 2H-7, 49 | 15.99 | 0.302 | 0.296 |
| 3H-1, 76 | 16.76 | 0.318 | 0.339 |
| 3H-2, 78 | 18.28 | 0.334 | 0.318 |
| 3H-3, 58 | 19.58 | 0.321 | 0.338 |
| 3H-4, 44 | 20.94 | 0.326 | 0.323 |
| 3H-5, 82 | 22.82 | 0.332 | 0.332 |
| 3H-6, 93 | 24.43 | 0.324 | 0.330 |
| 3H-7, 73 | 25.73 | 0.336 | 0.337 |
| 4H-1, 71 | 26.21 | 0.348 | 0.361 |
| 4H-2, 88 | 27.88 | 0.346 | 0.329 |
| 4H-3, 68 | 29.18 | 0.344 | 0.344 |
| 4H-4, 62 | 30.62 | 0.349 | 0.348 |
| 4H-5, 61 | 32.11 | 0.330 | 0.339 |
| 4H-6, 62 | 33.62 | 0.320 | 0.342 |
| 4H-7, 81 | 35.31 | 0.334 | 0.342 |
| 5H-1, 69 | 35.69 | 0.338 | 0.335 |
| 5H-2, 65 | 37.15 | 0.337 | 0.317 |
| 5H-3, 65 | 38.65 | 0.337 | 0.316 |
| 5H-4, 66 | 40.16 | 0.350 | 0.341 |
| 5H-5, 98 | 41.98 | 0.342 | 0.331 |
| 5H-6, 74 | 43.24 | 0.341 | 0.338 |
| 5H-7, 44 | 44.44 | 0.358 | 0.349 |
| 6H-1, 65 | 45.15 | 0.374 | 0.363 |
| 6H-2, 19 | 46.19 | 0.380 | 0.369 |
| 6H-3, 83 | 48.33 | 0.357 | 0.340 |
| 6H-4, 40 | 49.40 | 0.350 | 0.351 |
| 6H-5, 43 | 50.93 | 0.356 | 0.350 |
| 6H-6, 65 | 52.65 | 0.336 | 0.332 |
| 6H-7, 66 | 54.16 | 0.345 | 0.365 |
| 7H-1, 108 | 55.08 | 0.411 | 0.367 |
| 7H-2, 70 | 56.20 | 0.371 | 0.361 |
| 7H-3, 31 | 57.31 | 0.347 | 0.341 |
| 7H-4, 27 | 58.23 | 0.373 | 0.389 |
| 7H-5, 7 | 59.53 | 0.367 | 0.385 |
| 7H-6, 41 | 61.37 | 0.333 | 0.328 |
| 7H-7, 30 | 62.76 | 0.416 | 0.311 |
| 8H-1, 47 | 63.97 | 0.352 | 0.340 |
| 8H-2, 49 | 65.49 | 0.360 | 0.361 |
| 8H-3, 94 | 67.44 | 0.380 | 0.342 |
| 8H-4, 107 | 69.07 | 0.350 | 0.326 |
| 8H-5, 88 | 70.38 | 0.388 | 0.387 |
| 8H-6, 81 | 71.81 | 0.360 | 0.354 |
| 8H-7, 25 | 72.75 | 0.386 | 0.356 |
| 9H-1, 99 | 73.99 | 0.392 | 0.399 |
| 9H-2, 58 | 75.08 | 0.451 | 0.454 |
| 10H-1, 104 | 83.54 | 0.370 | 0.341 |
| 13X-1, 60 | 106.90 | 0.361 | 0.329 |
| 13X-2, 61 | 108.41 | 0.375 | 0.347 |
| 13X-3, 58 | 109.88 | 0.416 | 0.364 |
| 13X-4, 94 | 111.74 | 0.403 | 0.353 |
| 14X-1, 78 | 116.68 | 0.345 | 0.348 |
| 17X-1, 34 | 145.14 | 0.410 | 0.360 |
| 17X-2, 66 | 146.96 | 0.374 | 0.354 |
| 17X-3, 46 | 148.26 | 0.420 | 0.371 |
| 17X-4, 51 | 149.81 | 0.483 | 0.405 |
| 18X-1, 43 | 154.93 | 0.477 | 0.437 |
| 18X-2, 43 | 156.43 | 0.465 | 0.493 |
| 18X-3, 43 | 157.93 | 0.460 | 0.491 |
| 18X-4, 42 | 159.42 | 0.463 | 0.447 |
| 18X-5, 43 | 160.93 | 0.426 | 0.425 |
| 18X-6, 43 | 162.43 | 0.462 | 0.429 |
| 18X-7, 10 | 163.60 | 0.435 | 0.420 |
| 19X-1, 101 | 165.11 | 0.420 | 0.397 |
| 19X-2, 101 | 166.61 | 0.414 | 0.394 |
| 19X-3, 78 | 167.88 | 0.442 | 0.425 |
| 19X-4, 67 | 169.27 | 0.445 | 0.442 |
| 19X-5, 38 | 170.48 | 0.453 | 0.434 |
| 19X-6, 10 | 171.70 | 0.442 | 0.443 |
| 20X-1, 42 | 174.22 | 0.461 | 0.444 |
| 20X-2, 87 | 176.17 | 0.448 | 0.458 |
| 20X-3, 100 | 177.80 | 0.429 | 0.447 |
| 20X-4, 46 | 178.76 | 0.452 | 0.472 |
| 20X-5, 72 | 180.52 | 0.458 | 0.474 |
| 21X-1, 76 | 184.16 | 0.459 | 0.498 |
| 21X-2, 77 | 185.67 | 0.469 | 0.455 |
| 21X-3, 79 | 187.19 | 0.469 | 0.454 |
| 21X-4, 85 | 188.75 | 0.456 | 0.463 |
| 21X-5, 82 | 190.22 | 0.443 | 0.451 |
| 21X-6, 15 | 191.05 | 0.449 | 0.446 |
| 22X-1, 76 | 193.86 | 0.465 | 0.487 |
| 22X-2, 78 | 195.38 | 0.497 | 0.492 |
| 22X-3, 79 | 196.89 | 0.465 | 0.471 |
| 22X-4, 77 | 198.37 | 0.461 | 0.473 |
| 22X-5, 24 | 199.34 | 0.512 | 0.497 |
| 23X-1, 85 | 203.65 | 0.472 | 0.484 |
| 23X-2, 86 | 205.16 | 0.461 | 0.472 |
| 23X-3, 80 | 206.60 | 0.486 | 0.490 |
| 23X-4, 74 | 208.04 | 0.492 | 0.493 |
| 23X-5, 61 | 209.41 | 0.489 | 0.491 |
| 24X-1, 83 | 213.33 | 0.478 | 0.495 |
| 24X-2, 123 | 215.23 | 0.486 | 0.503 |
| 25X-1, 90 | 223.00 | 0.488 | 0.489 |
| 25X-2, 85 | 224.45 | 0.453 | 0.460 |
| 25X-3, 90 | 226.00 | 0.481 | 0.508 |
| 25X-4, 99 | 227.59 | 0.497 | 0.493 |
| 25X-5, 86 | 228.96 | 0.515 | 0.528 |
| 26X-1, 78 | 232.48 | 0.544 | 0.520 |
| 26X-2, 80 | 234.00 | 0.538 | 0.533 |
| 26X-3, 88 | 235.58 | 0.560 | 0.537 |
| 26X-4, 85 | 237.05 | 0.550 | 0.537 |
| 26X-5, 80 | 238.50 | 0.594 | 0.537 |
| 26X-6, 105 | 240.25 | 0.556 | 0.521 |
| 26X-7, 13 | 240.83 | 0.721 | 0.566 |
| 27X-1, 25 | 241.65 | 0.702 | 0.568 |
| 27X-2, 25 | 243.15 | 0.601 | 0.620 |
| 27X-3, 25 | 244.65 | 0.598 | 0.556 |
| 27X-4, 24 | 246.14 | 0.558 | 0.585 |
| 27X-5, 25 | 247.65 | 0.734 | 0.608 |
| 27X-6, 25 | 249.15 | 0.442 | 0.485 |
| 28X-1, 131 | 252.41 | 0.478 | 0.493 |
| 28X-2, 77 | 253.37 | 0.504 | 0.461 |
| 28X-3, 97 | 255.07 | 0.542 | 0.497 |
| 28X-4, 95 | 256.55 | 0.561 | 0.537 |
| 28X-4, 117 | 256.77 | 0.558 | 0.527 |
| 28X-5, 67 | 257.77 | 0.520 | 0.503 |
| 28X-6, 33 | 258.93 | 0.500 | 0.470 |
| 29X-1, 110 | 261.80 | 0.479 | 0.480 |
| 29X-2, 110 | 263.30 | 0.507 | 0.483 |
| 29X-3, 110 | 264.80 | 0.618 | 0.615 |
| 29X-4, 110 | 266.30 | 0.524 | 0.567 |
| 29X-5, 110 | 267.80 | 0.623 | 0.559 |
| 30X-1, 127 | 271.67 | 0.530 | 0.490 |
| 30X-2, 105 | 272.95 | 0.542 | 0.529 |
| 30X-3, 102 | 274.42 | 0.527 | 0.499 |
| 30X-4, 115 | 276.05 | 0.522 | 0.535 |
| 30X-5, 79 | 277.19 | 0.567 | 0.529 |
| 30X-6, 55 | 278.45 | 0.554 | 0.523 |
| 31X-1, 97 | 280.87 | 0.595 | 0.511 |
| 31X-2, 99 | 282.39 | 0.572 | 0.580 |
| 31X-3, 54 | 283.44 | 0.598 | 0.627 |
| 31X-4, 53 | 284.93 | 0.613 | 0.581 |
| 31X-5, 26 | 286.16 | 0.565 | 0.565 |
| 32X-1, 95 | 290.35 | 0.522 | 0.510 |
| 32X-2, 131 | 292.21 | 0.567 | 0.539 |
| 32X-3, 93 | 293.33 | 0.605 | 0.542 |
| 32X-4, 55 | 294.45 | 0.439 | 0.446 |
| 32X-5, 70 | 296.10 | 0.446 | 0.442 |
| 32X-6, 89 | 297.79 | 0.478 | 0.455 |
| 32X-7, 27 | 298.67 | 0.501 | 0.475 |
| 33X-1, 79 | 299.79 | 0.433 | 0.441 |
| 33X-2, 95 | 301.45 | 0.477 | 0.456 |
| 33X-3, 104 | 303.04 | 0.434 | 0.455 |
| 33X-4, 8 | 303.58 | 0.484 | 0.481 |
| 33X-5, 96 | 305.96 | 0.491 | 0.467 |
| 33X-6, 45 | 306.95 | 0.543 | 0.523 |
| 35X-1, 118 | 319.38 | 0.448 | 0.439 |
| 41X-1, 111 | 377.11 | 0.497 | 0.492 |
| 41X-2, 93 | 378.43 | 0.520 | 0.515 |
| 41X-3, 111 | 380.11 | 0.542 | 0.524 |
| 41X-4, 72 | 381.22 | 0.537 | 0.571 |
| 42X-1, 40 | 386.10 | 0.629 | 0.557 |
| 42X-2, 131 | 388.51 | 0.532 | 0.548 |
| 43X-1, 48 | 395.78 | 0.602 | 0.619 |
| 43X-2, 64 | 396.78 | 0.623 | 0.581 |
| 43X-3, 42 | 398.06 | 0.629 | 0.615 |
| 43X-4, 40 | 399.54 | 0.572 | 0.575 |
| 43X-5, 77 | 401.41 | 0.684 | 0.649 |
| 43X-6, 36 | 402.50 | 0.637 | 0.679 |
| 43X-7, 38 | 404.02 | 0.705 | 0.602 |
| 44X-1, 96 | 405.96 | 0.529 | 0.609 |
| 44X-2, 62 | 407.12 | 0.499 | 0.516 |
| 44X-3, 16 | 408.16 | 0.520 | 0.529 |
| 45X-1, 31 | 414.91 | 0.689 | 0.671 |
| 45X-2, 96 | 416.30 | 0.694 | 0.677 |
| 45X-3, 51 | 417.35 | 0.768 | 0.825 |
| 45X-4, 107 | 419.41 | 0.720 | 0.844 |
| 46X-1, 21 | 424.41 | 0.617 | 0.725 |

average constant velocity of 1540 m/s. Prominent reflections occur at both the top and bottom of seismic-facies Units 2 and 3. The synthetic seismogram shows these prominent reflections at the correct locations. Reversed polarity reflections occur at the base of seismic-facies Unit 3 (Unit R; 5.15 s two-way traveltime) indicating a velocity inversion.

## IN-SITU TEMPERATURE MEASUREMENTS

Temperature gradients and heat flow were determined using two downhole measurements and the bottom-water (mud-line) temperature. An ADARA measurement attempted during Core 936A-6H (54.0 mbsf) was unsuccessful; the coring shoe moved while in the sediment, causing friction-induced temperature increases. Another ADARA measurement was made during Core 936A-8H (73.0 mbsf) using instrument number 12. The mud-line temperature of 2.42°C measured from this instrument was used as the reference bottom-seawater temperature at this site. A successful measurement resulted in an extrapolated equilibrium temperature of 4.5°C at 73 mbsf. One WSTP measurement was made before Core 936A-16X (135.2 mbsf) using probe thermistor number 202. Unfortunately, the tool moved in the sediment and created two friction-induced temperature increases. However, we fit the curves of the two subsequent equilibrating temperature measurements and obtained similar extrapolated temperatures. Therefore, it appears that despite the movement of the WSTP tool, the time intervals were of sufficient length to derive satisfactory data. The measurement provided data yielding an extrapolated equilibrium temperature of 6.2°C at 135.2 mbsf that correlates well with mud-line and ADARA temperatures. We applied a correction of +144 Ω to the raw resistance values recorded by the WSTP data logger to correct for the difference in mud-line temperature recorded by the WSTP tool to that of the ADARA tool.

Equilibrium temperatures, extrapolated from synthetic curves constructed to fit transient temperature data, are plotted as a function of depth (mbsf) in Figure 44. Using the ADARA mud-line temperature and the sub-bottom temperatures from the ADARA and WSTP measurements downhole, the geothermal temperature gradient can be approximated by a linear mean of 28°C/km. We calculated heat flow by adopting the constant geothermal temperature gradient of 27.99°C/km and a thermal conductivity, K, of 1.2 ± 0.15 W/(m·K), which is an average of regression estimates at 100 mbsf. The calculated heat flow is 33.59 mW/m$^2$.

## SYNTHESIS AND SIGNIFICANCE

### Stratigraphic Significance

#### *Surficial Foraminifer Nannofossil Clay (Unit I)*

Unit I (0–0.96 mbsf) is an intensely bioturbated, Holocene, foraminifer-nannofossil clay (Fig. 45), with about 42% carbonate at the top of the unit decreasing to 6% near the base. One rust-colored diagenetic crust is present at 0.46 mbsf.

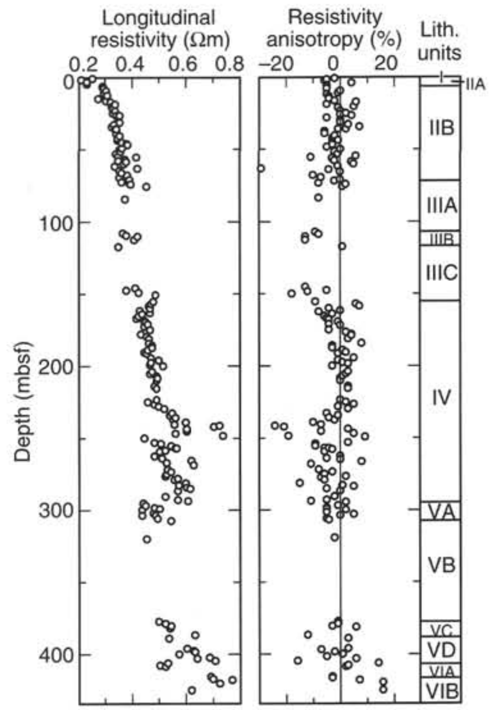


Figure 34. Longitudinal resistivity and resistivity anisotropy in Hole 936A.

#### *Amazon-Brown Levee (Unit II)*

Unit II (0.96–72.10 mbsf) consists of mud with interbedded laminae and beds of silt and very fine sand. Carbonate content is uniformly low (1.2%–2.3%). The unit is seismically correlated with the levee flanks of the Amazon-Brown Channel-levee System. Subunit IIA (0.96–6.97 mbsf) comprises intensely bioturbated mud. Subunit IIB (6.97–72.10 mbsf) consists of mud with thin beds of silt and fine sand. Although the unit shows an overall fining-upward trend, several intervals with abundant laminae and thin beds of silt and sand alternate with 1- to 3-m-thick intervals of moderately bioturbated mud with few silt laminae. Silt beds in Unit II have a higher mica content than silt beds deeper in the hole.

#### *HARPs (Unit III)*

The interval of high-amplitude reflection packets (HARPs) in the seismic-reflection profile correlates with lithologic Unit III (72.10–154.50 mbsf), which was an interval of poor core recovery (33.6%). The entire interval was logged. Detailed examination of the seismic profiles suggests that this interval includes, from top to base, the HARP at the base of the Brown Channel-levee System, the distal part of the Aqua levee and its underlying HARP, and the distal part of the Orange levee.

**Table 14. Logged intervals and tools used in Hole 936A.**

| | | Open hole | | In pipe | | |
|---|---|---|---|---|---|---|
| String | Run | (mbsf) | (mbrf) | (mbsf) | (mbrf) | Tools |
| Quad | Down | 84–305 | 3670–3891 | 0–84 | 3586–3670 | NGT/LSS/CNT-G/HLDT/DITE/TLT |
| | Up 1 | 333–94 | 3919–3680 | | | |
| | Up 2 | 164–65 | 3750–3651 | | | |
| FMS | Up 1 | 307–83 | 3893–3669 | | | NGT/GPIT/FMS |
| | Up 2 | 302–64 | 3888–3650 | | | |
| GLT | Up 1 | 290–84 | 3670–3876 | 84–0 | 3670–3586 | NGT/CNTG/AACT/GST/TLT |
| | Up 2 | 129–65 | 3715–3651 | 65–59 | 3651–3645 | |

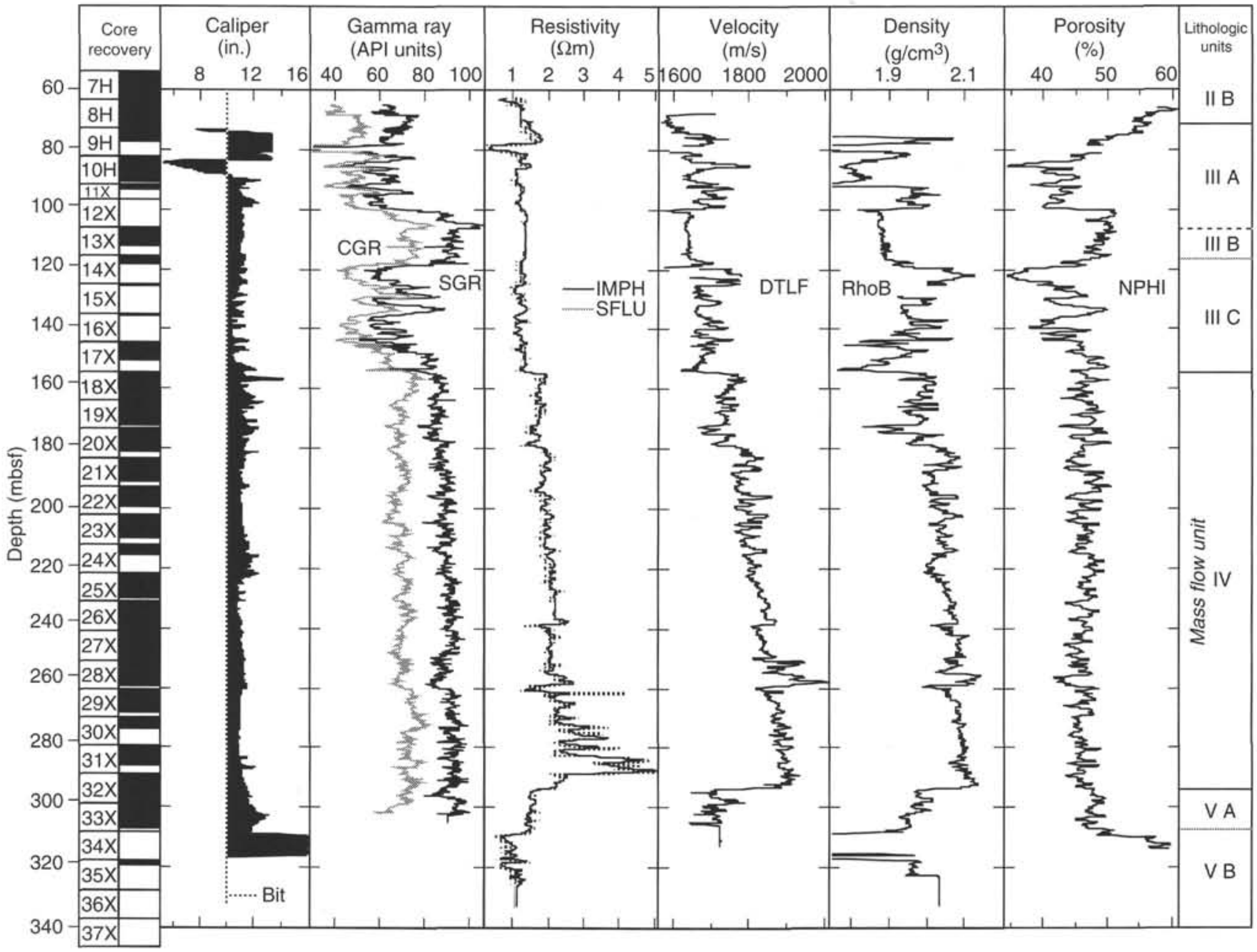


Figure 35. Summary of Hole 936A logging data from the Quad-combination tool. Left to right: core numbers and recovery (black); caliper and bit size; computed gamma ray (CGR = [Th + K]) and spectral or total gamma ray (SGR); medium induction phasor (IMPH) and spherically focused (SFLU) resistivity; long-spacing sonic velocity (DTLF); bulk density (RhoB); neutron porosity (NPHI); and lithologic units.

The Brown System HARP corresponds to lithologic Subunit IIIA (72.1–106.3 mbsf), where we recovered medium to coarse sand types, some in graded beds and others in massive beds with mud clasts. Some interbedded mud is also present. One pebble of siltstone was recovered. Log data suggest that the base of this sandy subunit is at 100 mbsf. The cores suggest that this subunit may form a thickening-upward sequence; this trend is masked in log response by the presence of abundant mud clasts near the top of the subunit.

The flank of the Aqua levee corresponds to lithologic Subunit IIIB (106.30–117.00 mbsf), which consists of color-banded mud with laminae and thin beds of silt and sand. The top of the subunit is bioturbated.

Beneath the Aqua levee, the seismic stratigraphy is more difficult to interpret in detail. The interval above the Unit R debris-flow deposit corresponds to lithologic Subunit IIIC (117.00–154.50 mbsf). Mud with silt laminae and a few 15- to 25-cm-thick fine sand beds were recovered. Log and core data suggest that this subunit can be divided into five parts.

(a) From about 117 to 119 mbsf, mud with laminae and thin beds of silt and fine sand forms the base of a fining-upward sequence that continues upward into Subunit IIIB.
(b) A 5-m-thick sand unit is recognized on log data from 119 to 124 mbsf.
(c) From 124 to 126 mbsf, log data suggest that sand units alternate with mud units.
(d) The log data show four sand intervals, with thin interbedded mud or abundant mud clasts between 126 and 147 mbsf. These intervals (a–d) from 119 to 147 mbsf probably correspond to the Aqua and earlier (?Purple, ?Blue) HARPs. These reflections are returned either from sand associated with avulsion or from sandy turbidites deposited by currents that flowed downfan, bypassing the active channel-levee system. From geochemical log data, these sand units appear to form a coarsening-upward sequence, but this could be an artifact of the distribution of mud clasts.
(e) The base of the unit consists of mud with laminae and thin beds of silt and very fine sand. The mud is moderately bioturbated and contains a CN15b nannofossil assemblage and common foraminifers including *P. obliquiloculata*. On the basis of seismic correlation and biostratigraphy at Site 930, this lower interval probably corresponds to the distal levee of the Orange Channel-levee System.

### *Unit R Debris-flow Deposit (Unit IV)*

The seismic Unit R, which has been interpreted as a debris-flow deposit, overlies the Red Channel-levee System and corresponds to

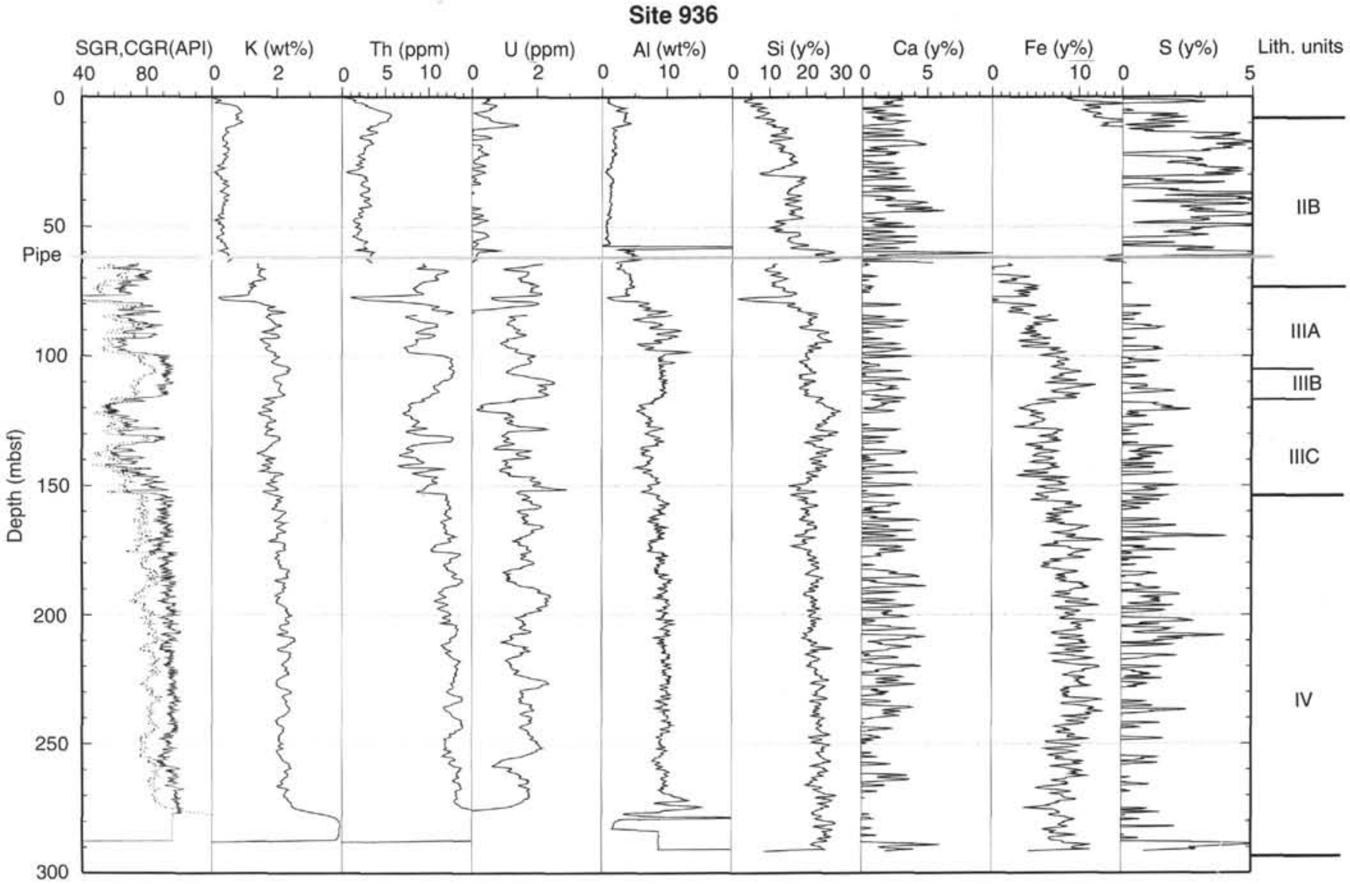


Figure 36. Summary of logging data from the geochemical logging tool. Log response is highly attenuated where the tool was in the drill pipe. Right column indicates lithostratigraphic units.

lithologic Unit IV (154.50–294.16 mbsf). This lithologic unit is similar to Unit IV at Site 935. The top 15 m of Unit IV contains mud clasts of varying color and consistency, wood, shell fragments, and fine pebbles (0.5 cm). One clast contains Miocene nannofossils. Between 190 and 260 mbsf, natural gamma logs show six cycles each with a gradual downward decrease in counts, followed by an abrupt increase at the top of the next cycle, thus resembling sedimentological fining-upward cycles. In the upper part of the unit, there are at least three 10- to 15-m-thick intervals that show a gradual upward decrease in water content (ranging from 22% at the top to 30% at the base) and resistivity (lab and log data), interpreted as resulting either from surface drainage of successive debris flows or from cyclic variation in grain size (as suggested by the natural gamma log). Below 225 mbsf, sediment strength is much greater, water content is more uniform at 19%–23%, and resistivity anisotropy shows a large scatter. This part of the unit consists principally of uniform dark mud, but also contains rare deformed sand beds, mud clasts of various shades of gray, and rare rock granules. An anomalously low concentration of pore-water chloride (547 mM) was found at 267 mbsf, and sulfate was present in two pore-water samples in this unit. Similar anomalous chloride and sulfate are found in mass-transport deposits at Sites 933 and 935.

### *Red Levee System (Subunits VA and VB)*

The Red Channel-levee System (Middle Levee Complex) is correlated with lithologic Unit V (294.16–405.69 mbsf). The buried Red Channel axis is located about 12 km west of the site. The seismic-reflection profiles suggest that the Red Channel-levee System overlies or laterally passes into a zone of higher amplitude reflections immediately west of the Gold Channel-levee System of the Lower Levee Complex. Subunit VA (294.16–307.35 mbsf) consists of mud with laminae and thin beds of silt and fine sand, with some thicker sand beds up to 25 cm thick. Log data suggest that the subunit forms a thinning-upward sequence. This subunit is interpreted as the distal flank of the Red levee. Log data also show that this subunit has low and downward decreasing resistivity, which may be related to undercompaction immediately beneath the mass-transport unit, as was observed at Sites 931, 933, and 935.

Subunit VB (307.35–377.40 mbsf) corresponds to an interval of poor core recovery (4.5%) of fine- and medium-grained sand and a few pebbles that corresponds to the high-amplitude reflections in the seismic reflection data. This part of the hole was partly washed out and only the top could be logged: these data suggest a predominance of sand.

### *Levee, Highstand Hemipelagic, and Debris-flow Deposits Between the Red and Gold Levees (Subunits VC and VD)*

Immediately above the Gold Channel-levee System are a series of lithologic units that cannot be resolved on seismic reflection profiles. Most of Subunit VC (from 377.40 to at least 383 mbsf) consists of mud with laminae and thin beds of silt and fine sand, interpreted as distal levee deposits. Foraminifers comprise rare *G. ruber* and *G. tumida*. In the top of the next core (Core 936A-42X) is a 65-cm-thick color-banded mud, with 11% carbonate. This mud contains a microfossil assemblage of calcareous nannofossils (Zone CN15a, 85–260 ka), abyssal benthic foraminifers, and planktonic foraminifers that in-

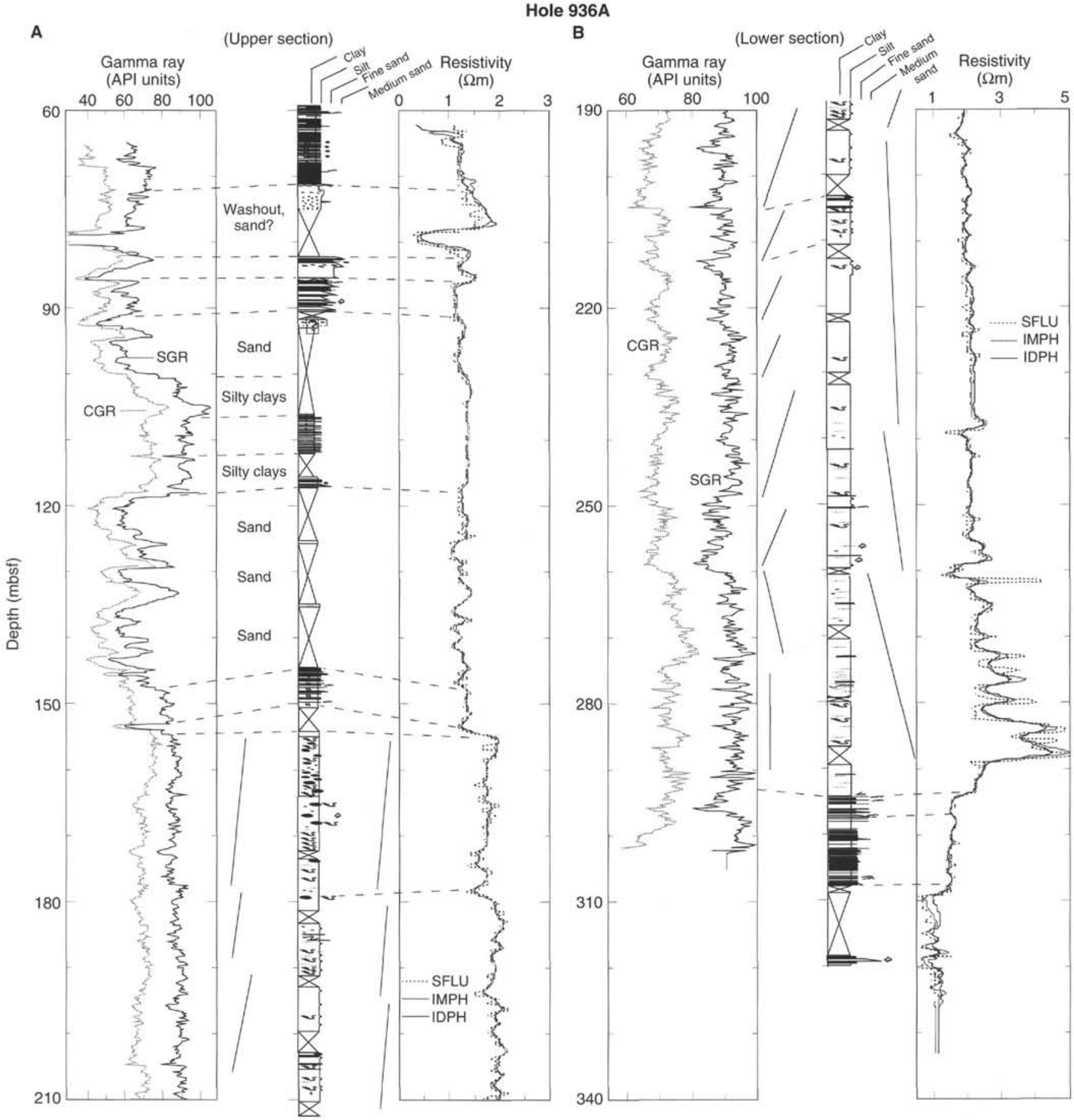


Figure 37. Comparison of gamma-ray and resistivity logs with core observations. **A.** From 60 to 210 mbsf. **B.** From 190 to 340 mbsf. Asymmetric trends (mostly upward decreasing gamma-ray and upward increasing resistivity) are indicated by slanted bars. Inferred lithology is indicated for intervals of poor recovery.

dicate warm but not fully interglacial conditions (*G. tumida* and *P. obliquiloculata* present, *G. menardii* and *G. tumida flexuosa* absent). This calcareous mud rests with abrupt contact on a sand bed that is at the top of a 1-m-thick sequence of disrupted mud with silt laminae and sand beds. The mud contains abundant nannofossils similar to those in the overlying calcareous mud. Whether some of the sand was injected during drilling disturbance is unclear, but thinner sand and silt beds are graded and therefore presumably in situ. It is unclear whether the sharp contact at the base of the calcareous mud and the disturbance of the underlying mud with silt and sand is solely a result of drilling disturbance, or whether both lithologies are blocks in the top of the underlying debris-flow deposit.

Subunit VD (387.52–405.69 mbsf) is a mud with common clasts, interpreted as a debris-flow deposit. It contains some carbonate-rich

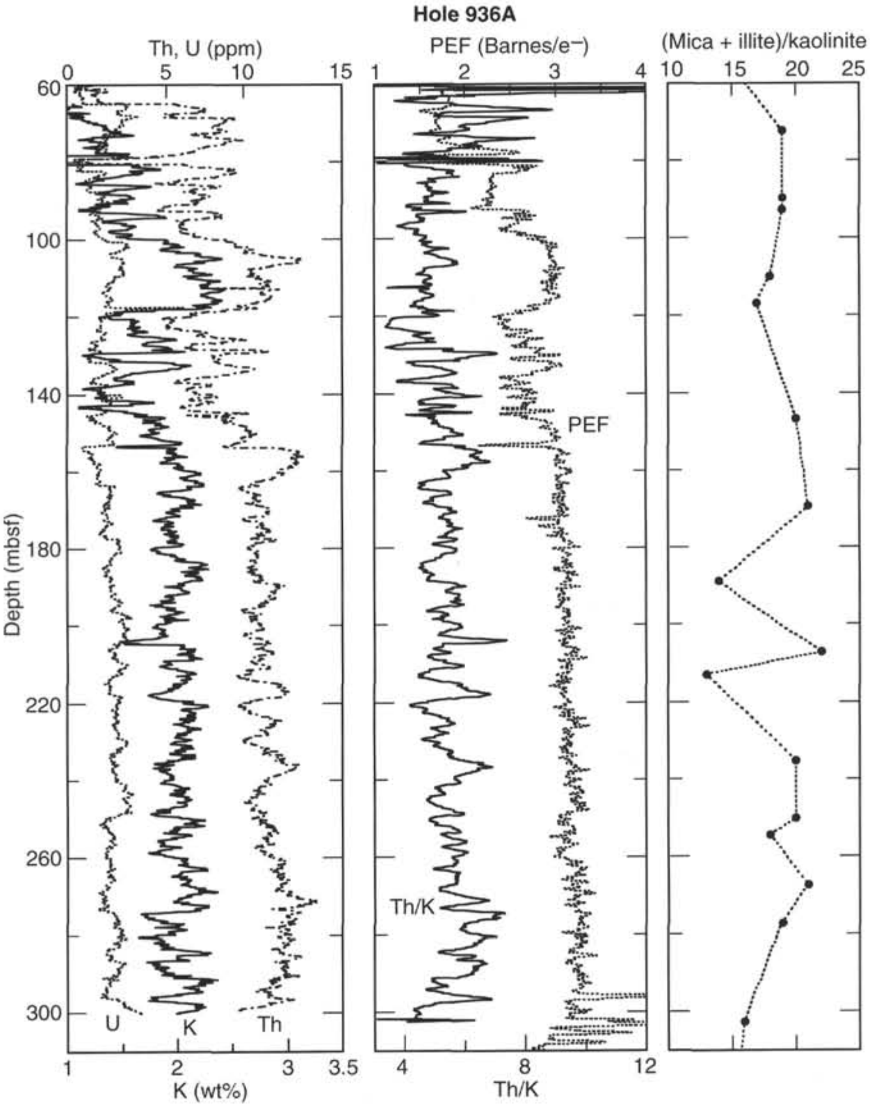


Figure 38. Comparison of gamma-ray logs (K, Th, U, Th/K) with the photoelectric effect (PEF) and calculated (mica + illite)/kaolinite ratios, based on X-ray diffraction analyses. Samples for X-ray analysis were taken in silt beds. Large ratios of illite/kaolinite should correspond to small Th/K ratios. The relatively poor correlation may result from the point nature of the analyses vs. the bulk measurements represented by the logs.

clasts (22%–32% carbonate) with microfossils similar to those in the underlying Subunit VIA (discussed below).

### *Highstand Calcareous Clay (Subunit VIA)*

Subunit VIA (405.69–415.35) comprises moderately bioturbated carbonate-bearing clay. A single carbonate determination from the lower part of the subunit contained 7% carbonate, but smear slides suggest that the upper part of the subunit has higher carbonate content. The total sulfur content is also rather high (0.7% to 0.11%), similar to that in the Holocene Unit I.

Nannofossils appear to be from Zone CN14b and include a high proportion of *Gephyrocapsa*. Foraminifers include high proportions of *G. tumida flexuosa* and *G. hexagonus,* indicating warm interglacial conditions. As in the Holocene section, pollen is rare.

### *Gold Levee (Subunit VIB)*

Subunit VIA passes gradually downcore into Subunit VIB (415.35–433.8), which comprises mud with laminae and thin beds of silt and rare fine sand. Foraminifer abundance decreases down through the subunit. This sequence is similar to that found on levees immediately below the Holocene hemipelagic deposits of Unit I.

## Implications

Microfossil assemblages are similar to those at Site 935 and increase our confidence that a simple stratigraphic sequence is present at both sites. The base of the Holocene is at about 1 mbsf. The 40-ka *P. obliquiloculata* datum cannot be identified with confidence because of barren intervals in the core between 112 and 149 mbsf, and its first downcore re-appearance at 149 mbsf is associated with a CN15b nannofossil assemblage, placing its age between 40 ka and 85 ka. As at Site 935, bioturbated sediment (Subunit VIA) at the top of the Lower Levee Complex has a full-interglacial microfossil assemblage with CN14b Zone nannofossils. A younger interglacial is represented by the calcareous mud in Core 936A-42X (base of Subunit VC), with a cooler foraminiferal assemblage than Subunit VIA and a CN15a nannofossil assemblage.

Many of the sedimentological features of this site confirm observations made at earlier sites, in particular Site 935. HARP sequences are confirmed as complex alternations of medium- and coarse-grained sand types with mud-rich intervals. Most of the HARP sand types show no prominent asymmetry in bed thickness or grain size, although the Brown HARP appears to form a coarsening-upward sequence with a sharp basal contact.

The Unit IV mass-transport deposit has a remarkably similar stratigraphy to the correlative deposit at Site 935, 25 km distant. The overall sequence from muddy polymictic debris-flow deposits down to very stiff, rather featureless mud might represent a single (possibly complex) event, or the same multiple events.

## REFERENCES*

Bray, E.E., and Evans, E.D., 1961. Distribution of *n*-paraffins as a clue to recognition of source beds. *Geochim. Cosmochim. Acta,* 22:2–15.

Damuth, J.E., 1977. Late Quaternary sedimentation in the western equatorial Atlantic. *Geol. Soc. Am. Bull.,* 88:695–710.

Flood, R.D., Manley, P.L., Kowsmann, R.O., Appi, C.J., and Pirmez, C., 1991. Seismic facies and late Quaternary growth of Amazon submarine fan. *In* Weimer, P., and Link, M.H. (Eds.), *Seismic Facies and Sedimentary Processes of Submarine Fans and Turbidite Systems:* New York (Springer-Verlag), 415–433.

Manley, P.L., and Flood, R.D., 1988. Cyclic sediment deposition within Amazon deep-sea fan. *AAPG Bull.,* 72:912–925.

Tissot, B.P., and Welte, D.H., 1984. *Petroleum Formation and Occurrence* (2nd ed.): Heidelberg (Springer-Verlag).

*Abbreviations for names of organizations and publications in ODP reference lists follow the style given in *Chemical Abstracts Service Source Index* (published by American Chemical Society).

**Ms 155IR-112**

**NOTE: For all sites drilled, core-description forms ("barrel sheets") and core photographs can be found in Section 4, beginning on page 703. Forms containing smear-slide data can be found in Section 5, beginning on page 1199. GRAPE, index property, magnetic susceptibility, and natural gamma data are presented on CD-ROM (back pocket).**

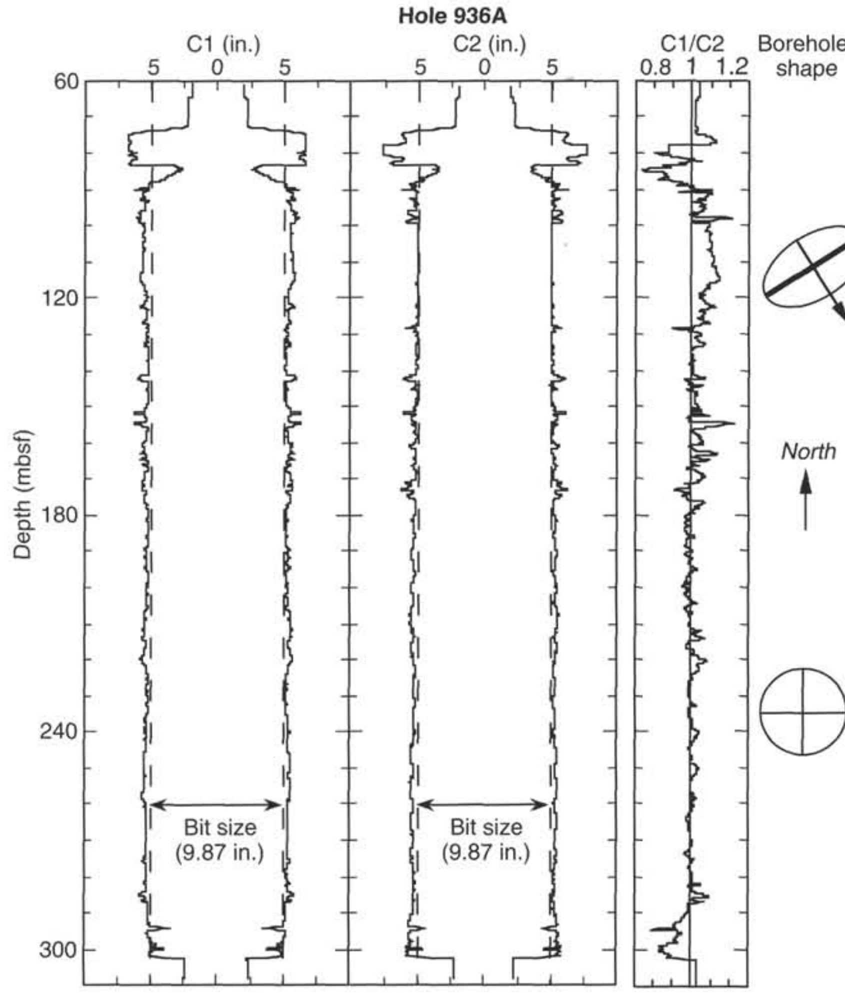


Figure 39. Borehole caliper measurements from the FMS tool (C1, C2), and borehole ellipticity indicated by the ratio C1/C2. Column to the right summarizes borehole shape and orientation, based on the azimuth of C1. Arrow shows direction of Pad 1.

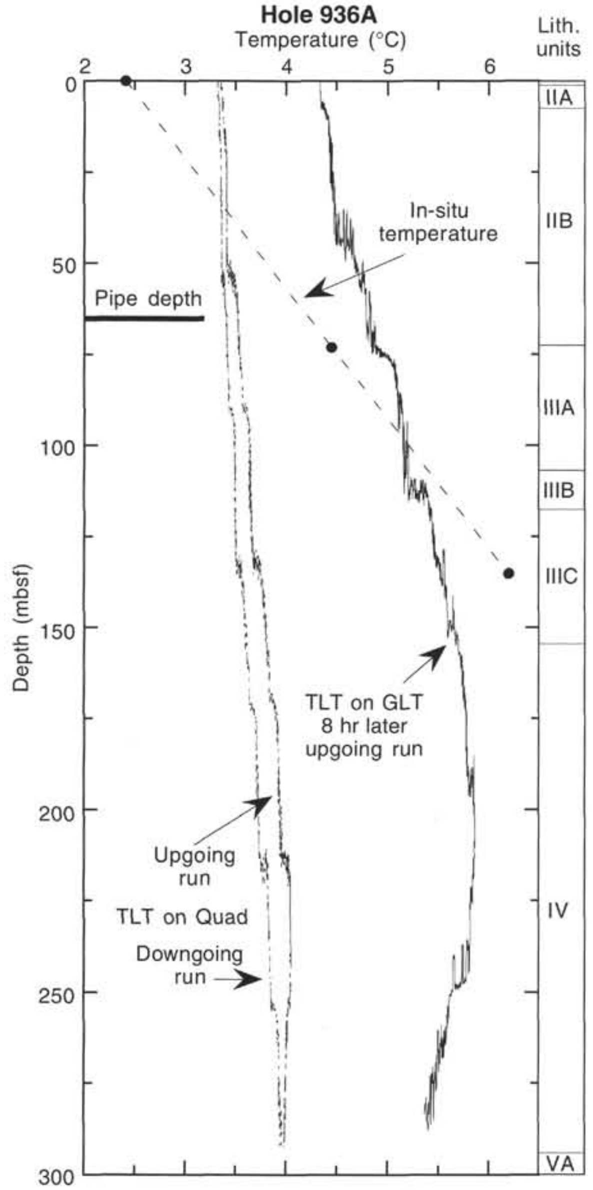


Figure 40. Borehole temperature measurements from the TLT (slow response thermistor) and in-situ temperature from ADARA and WSTP.

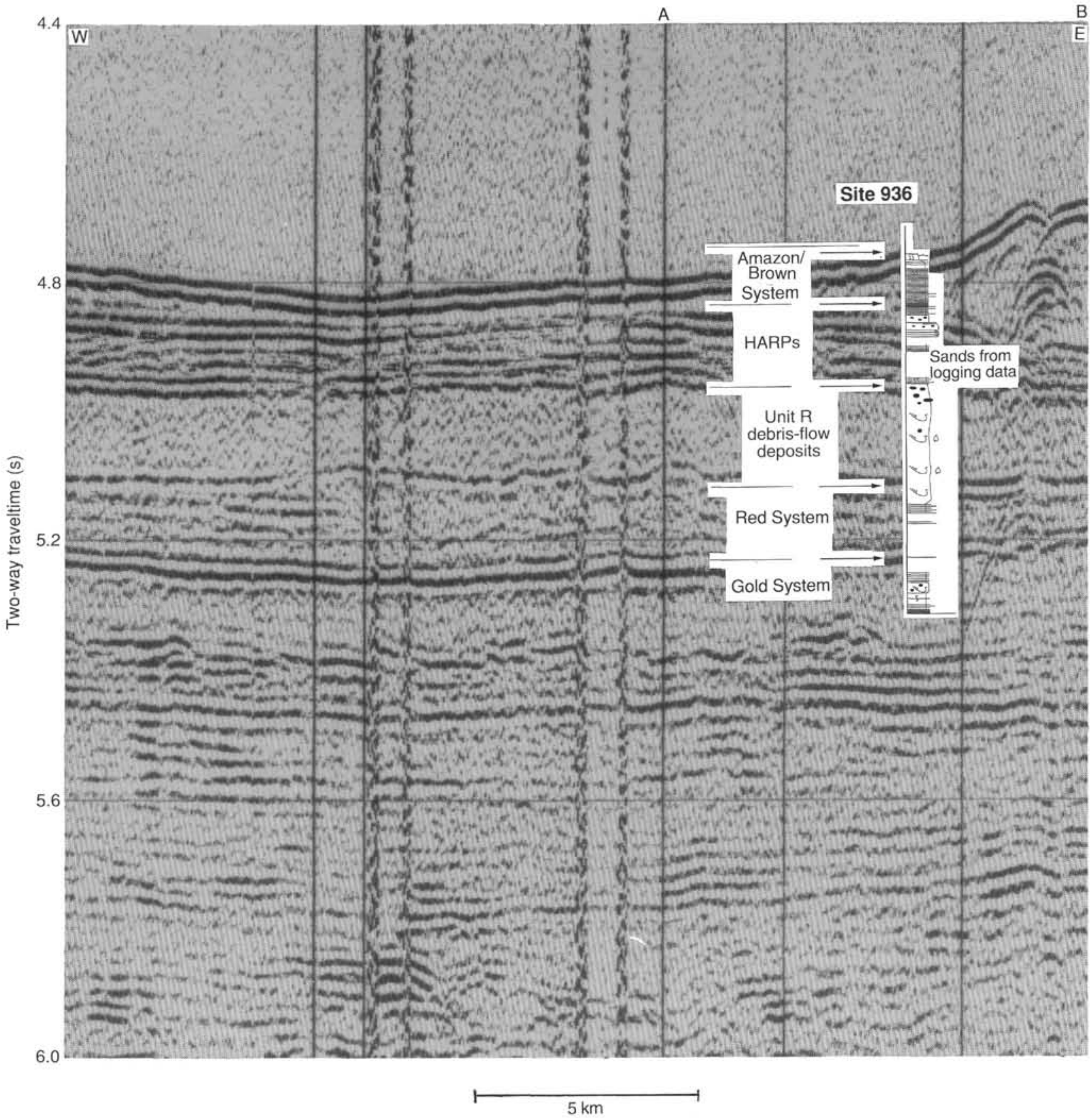


Figure 41. Seismic-reflection profile showing Site 936 with the corresponding lithostratigraphic section. Location shown in Fig. 1.

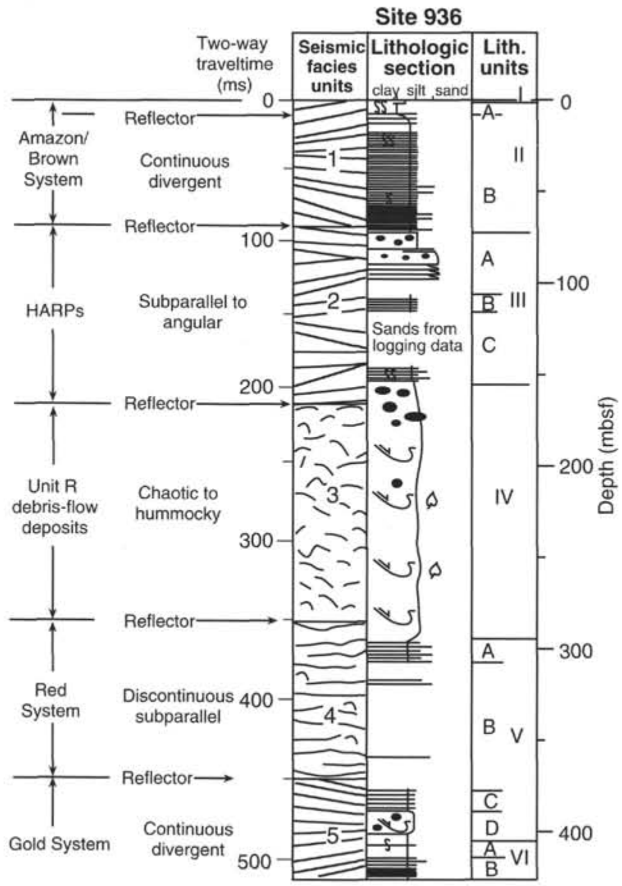


Figure 42. Correlation of lithostratigraphic observations with seismic-facies units and prominent reflections (arrows) at Site 936.

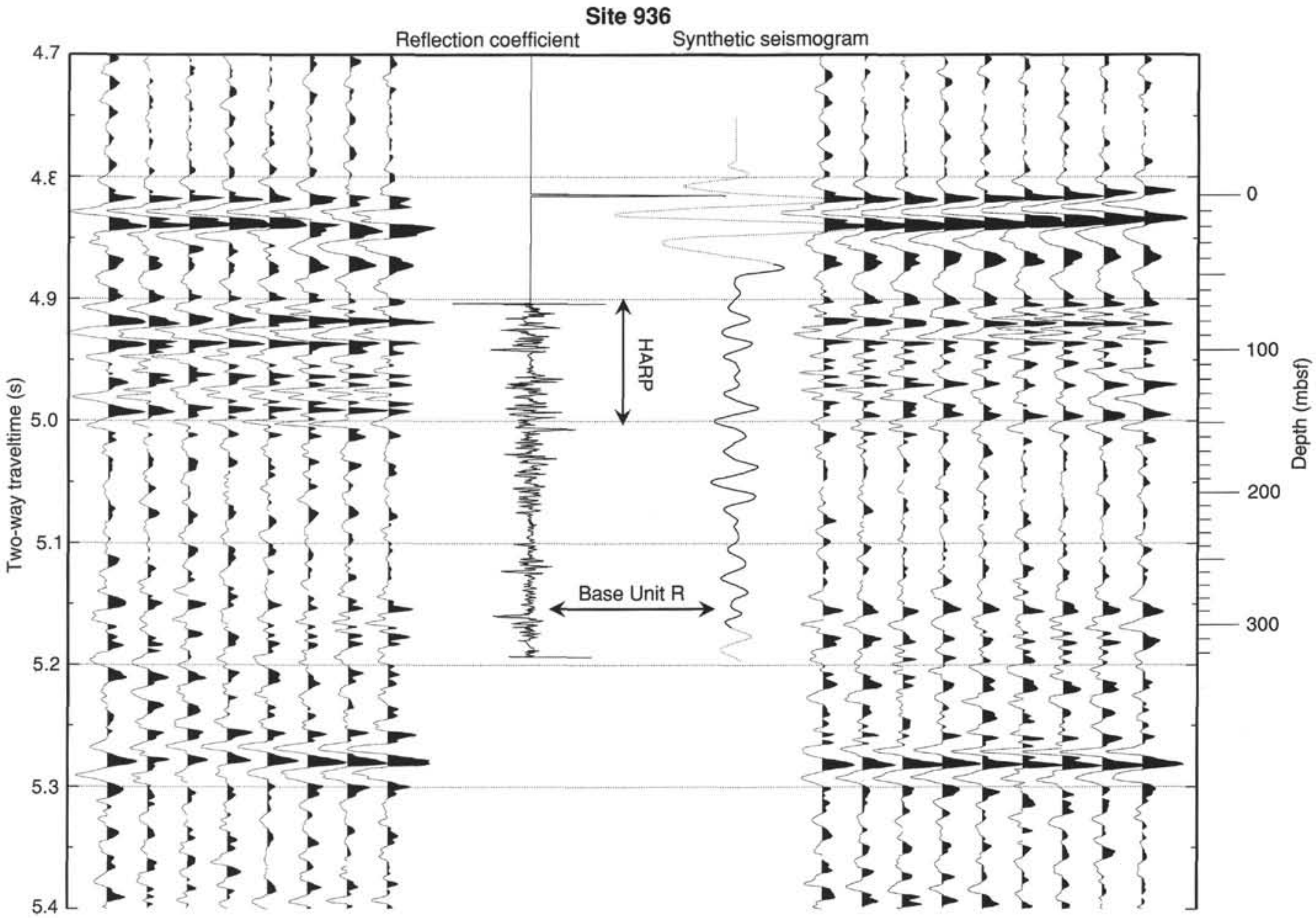


Figure 43. Synthetic seismogram for Site 936. Solid line portion of the synthetic seismogram was determined from the log data.

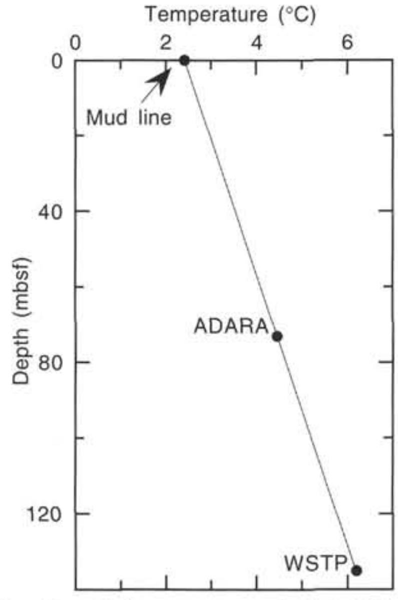


Figure 44. Estimated equilibrium temperatures in Hole 936A. A linear curve fit through the data suggests that reliable equilibrium temperatures were acquired that indicate a geothermal gradient of 27.99°C/km.

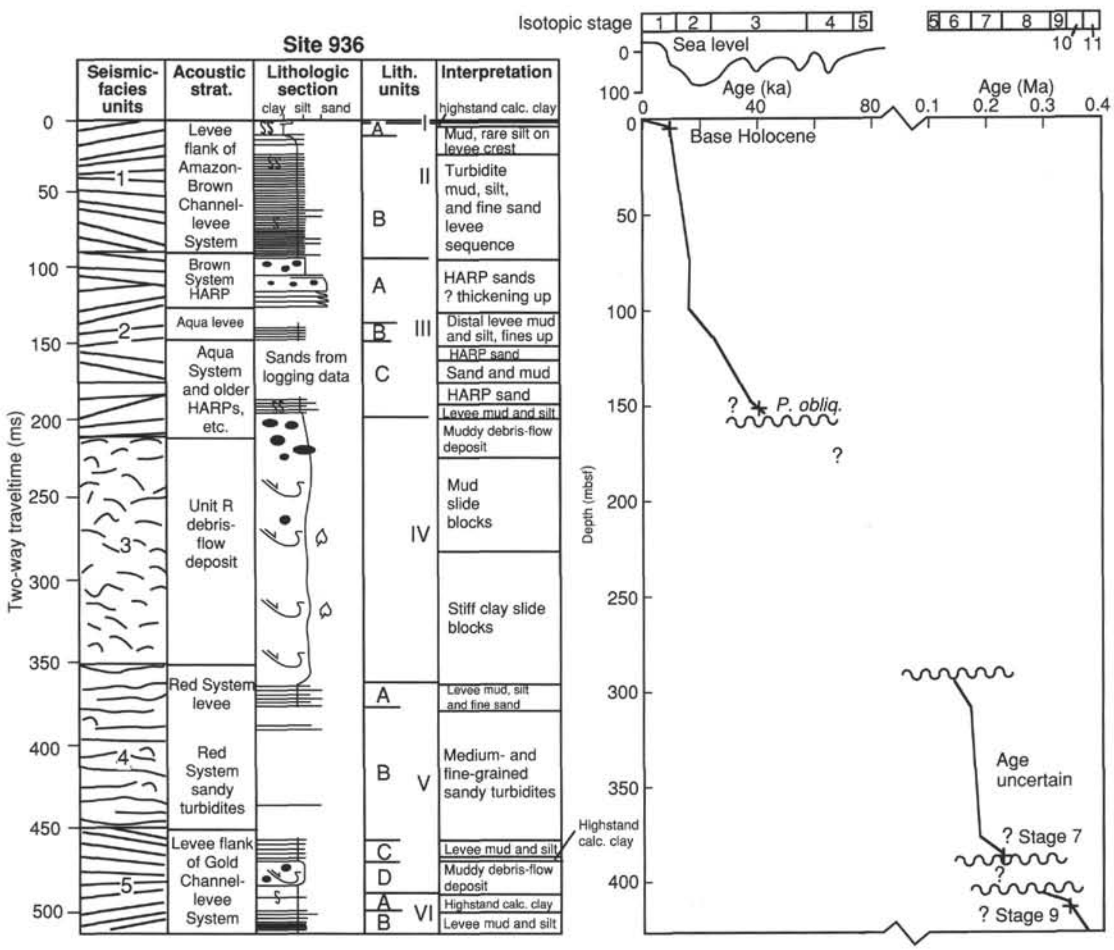


Figure 45. Summary of Site 936 showing (left to right) seismic-facies units, acoustic stratigraphy, schematic lithologic column, lithologic units, log stratigraphic units, interpreted sediment facies, chronological picks, and interpreted age-depth curve (+ = datums; variations in slope between these points are interpreted, based on dated intervals of similar facies at other sites).

# SHORE-BASED LOG PROCESSING

# HOLE 936A

**Bottom felt:** 3586 mbrf
**Penetration:** 433.8 mbsf
**Total core recovered:** 274.42 m (63%)

## Logging Runs

**Logging string 1:** DIT/LSS/HLDT/CNT/NGT
**Logging string 2:** FMS/GPIT/NGT (two passes)
**Logging string 3:** ACT/GST/NGT
Wireline heave compensator was used to counter ship heave.

## Bottom-hole Assembly/Drill Pipe

The following bottom-hole assembly and drill-pipe depths are as they appear on the logs after differential depth shift (see **Depth shift** section below) and depth shift to the seafloor. As such, there may be a discrepancy with the original depths given by the drillers on board. Possible reasons for depth discrepancies are ship heave, use of wireline heave compensator, and drill-string and/or wireline stretch.

DIT/LSS/HLDT/CNTG/NGT (main): Bottom-hole assembly at 127 mbsf.
DIT/LSS/HLDT/CNTG/NGT (repeat): Bottom-hole assembly at 63 mbsf.
ACT/GST/NGT: Bottom-hole assembly at 81 mbsf.
FMS/GPIT/NGT (pass 1): Bottom-hole assembly at 85 mbsf.
FMS/GPIT/NGT (pass 2): Recorded open hole.
DIT/LSS/HLDT/CNTG/NGT (main): Did not reach drill pipe.
DIT/LSS/HLDT/CNTG/NGT (repeat): Did not reach drill pipe.
ACT/GST/NGT: Drill pipe at 11.5 mbsf.
FMS/GPIT/NGT (pass 1): Did not reach drill pipe.
FMS/GPIT/NGT (pass 2): Recorded open hole.

## Processing

**Depth shift:** All original logs have been interactively depth shifted with reference to NGT from ACT/GST/NGT run, and to the seafloor (–3586 m). A list of the amount of differential depth shifts applied at this hole is available upon request.

**Gamma-ray processing:** NGT data have been processed to correct for borehole size and type of drilling fluid.

**Acoustic data processing:** No processing necessary due to the good quality of the logs.

**Geochemical processing:** For detailed explanation of the processing, please refer to the "Explanatory Notes" chapter, this volume, or to the "geochem.doc" file on the enclosed CD-ROM (back pocket). The elemental yields recorded by the GST tool represent the relative contribution of only some of the rock-forming elements (Fe, Ca, Cl, Si, S, H, Gd, and Ti—the last two computed during geochemical processing) to the total spectrum.

Because other rock-forming elements are present in the formation (Al, K, etc.), caution is recommended in using the yields to infer lithologic changes. Instead, ratios (see "acronyms.doc" on CD-ROM) are more appropriate to determine changes in the macroscopic properties of the formation. A list of oxide factors used in geochemical processing includes the following:

$SiO_2$ = 2.139
$CaCO_3$ = 2.497
FeO* = 1.358
$TiO_2$ = 1.668
$K_2O$ = 1.205
$Al_2O_3$ = 1.889
FeO* computed using an oxide factor that assumes a 50:50 combination of $Fe_2O_3$ and FeO factors.

## Quality Control

During the processing, quality control of the data is mainly performed by cross-correlation of all logging data. Large (>12 in.) and/or irregular borehole adversely affects most recordings, particularly those that require eccentralization and a good contact with the borehole wall (CNTG, HLDT).

Hole diameter was recorded by the hydraulic caliper on the HLDT tool (CALI), and by the caliper on the FMS string (C1 and C2). During the repeat pass, the HLDT caliper started closing at 92 mbsf; therefore, the density data have not been corrected for borehole size in the interval from 92 to 63 mbsf.

Data recorded through pipe and bottom-hole assembly (such as the NGT recorded in the upper part of the hole) should be used only qualitatively because of the attenuation on the incoming signal.

The resistivity, gamma-ray, density, caliper, neutron, and acoustic data from the DIT/SDT/HLDT/CNT/NGT main and repeat passes have been merged as follows:

Resistivity: merged at 124 mbsf.
Gamma ray: merged t 130 mbsf and 60 mbsf (ACT/GST/NGT)
Density: merged at 130 mbsf.
Caliper: merged at 130 mbsf.
Neutron: merged at 130 mbsf.
Acoustic: merged at 130 mbsf.

FACT = quality control curve in geochemical processing. Accuracy of the estimates is inversely proportional to the magnitude of the curve.

**Note:** Details of standard shore-based processing procedures are found in the "Explanatory Notes" chapter, this volume. For further information about the logs, please contact:

Cristina Broglia
Phone: 914-365-8343
Fax: 914-365-3182
Email: chris@ldeo.columbia.edu

Elizabeth Pratson
Phone: 914-365-8313
Fax: 914-365-3182
Email: beth@ldeo.columbia.edu

936A Geochemical Logging Data

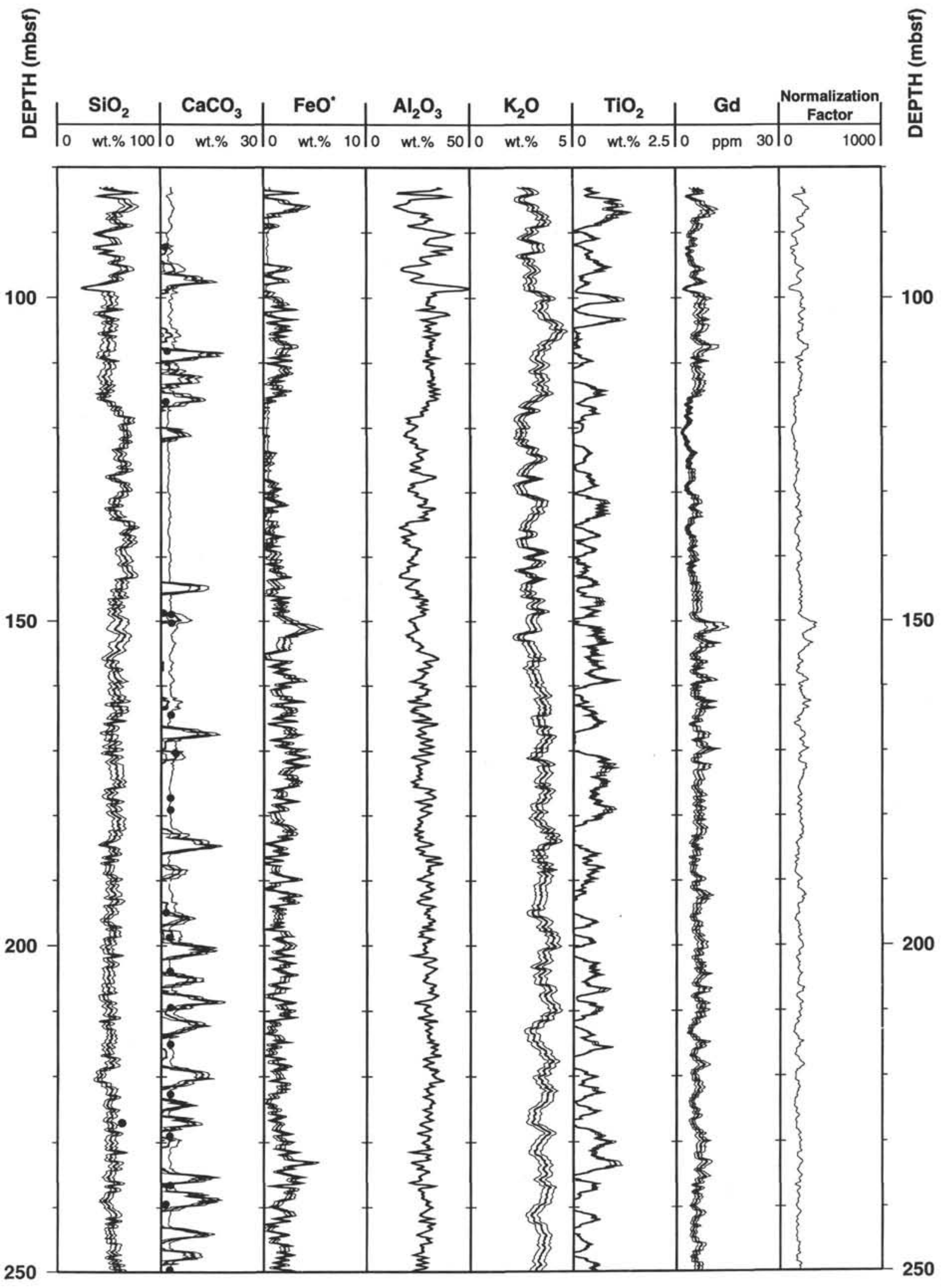

936A Geochemical Logging Data (cont.)

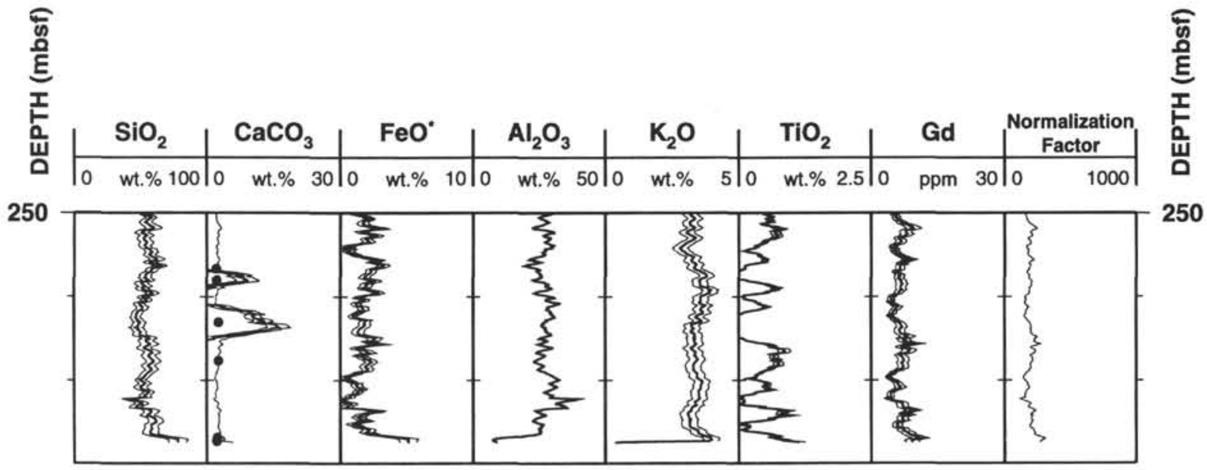

936A Natural Gamma Ray-Density-Porosity Logging Data

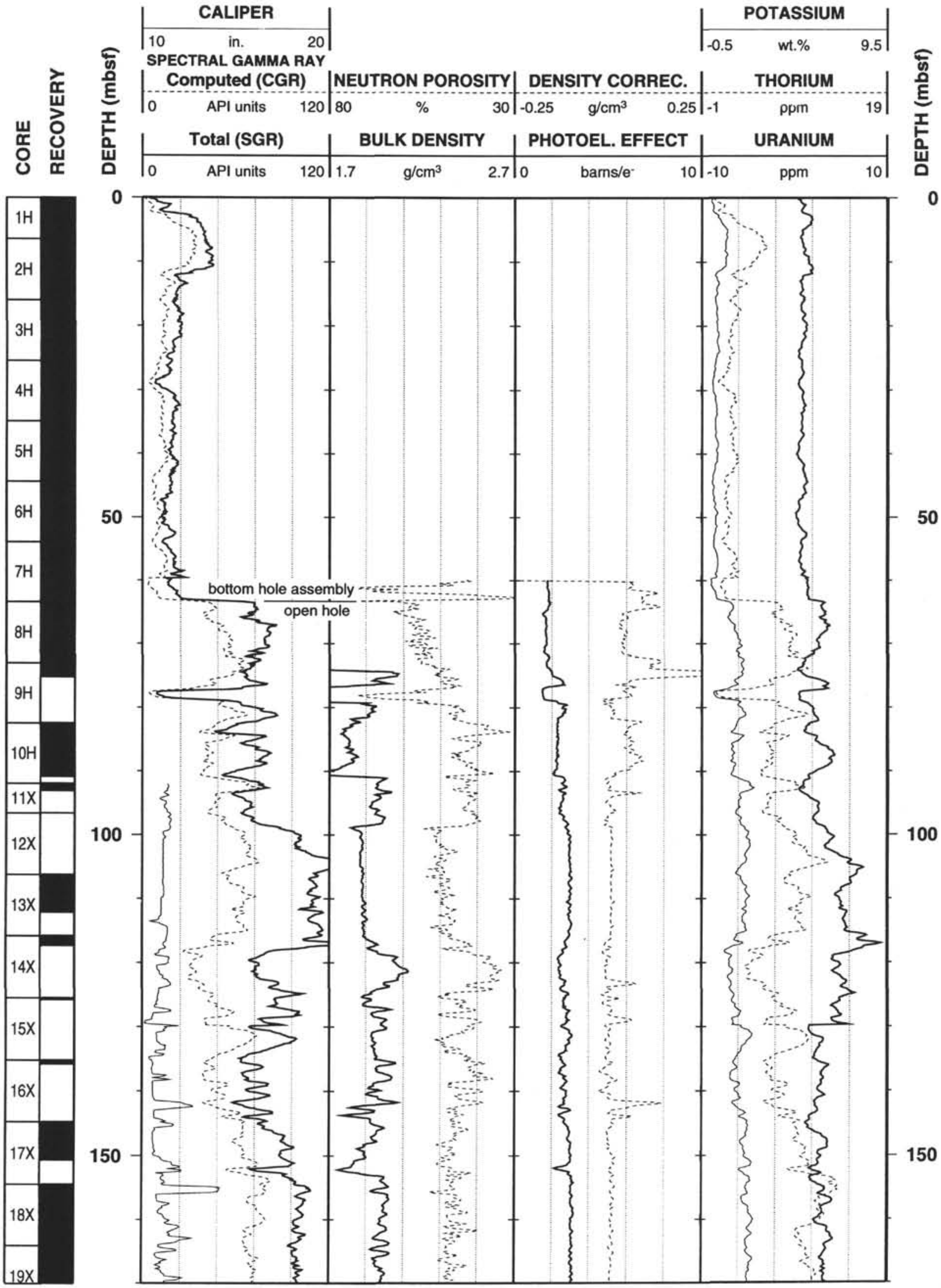

936A Natural Gamma Ray-Density-Porosity Logging Data (cont.)

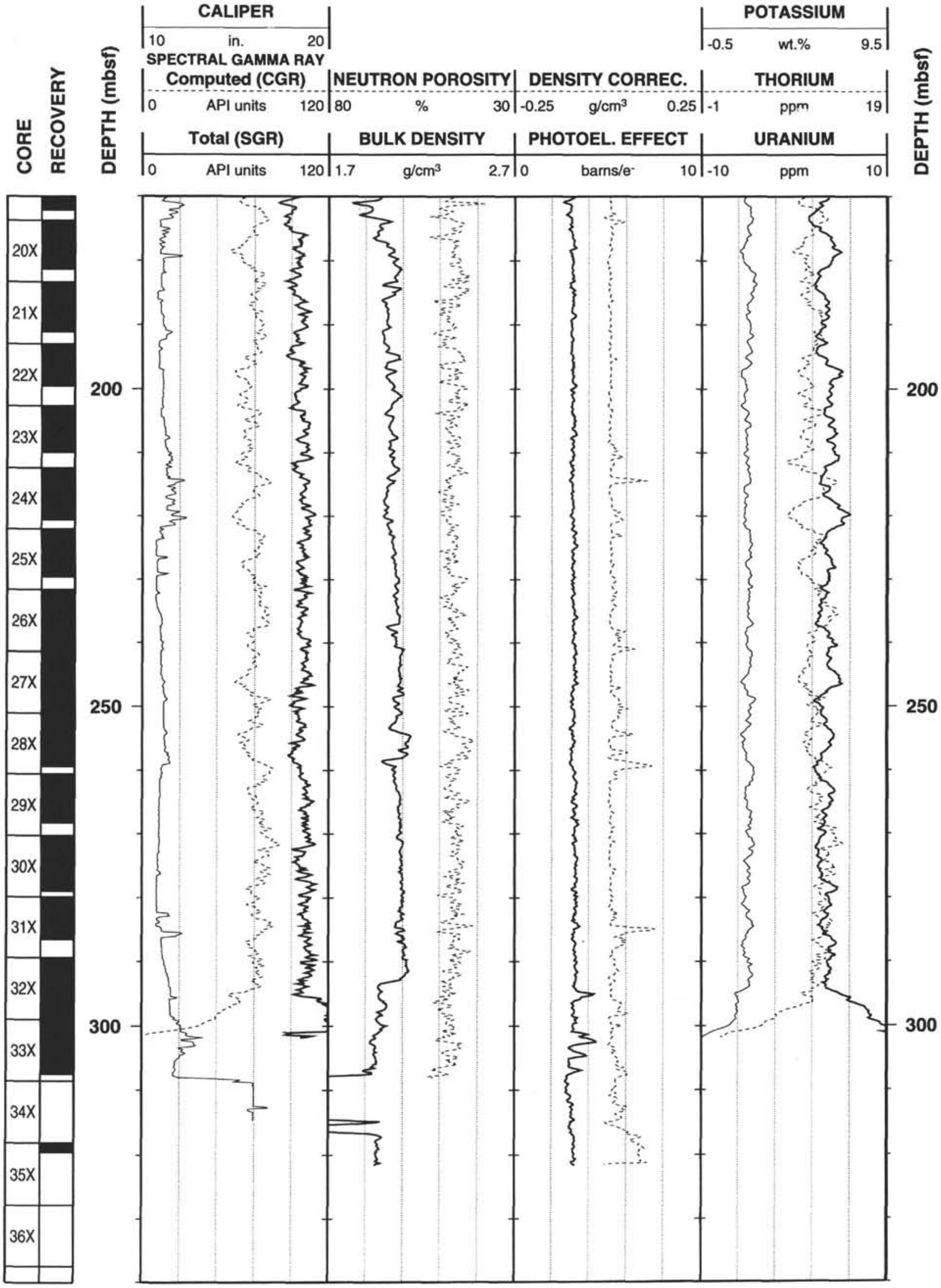

936A Natural Gamma Ray-Resistivity-Velocity Logging Data

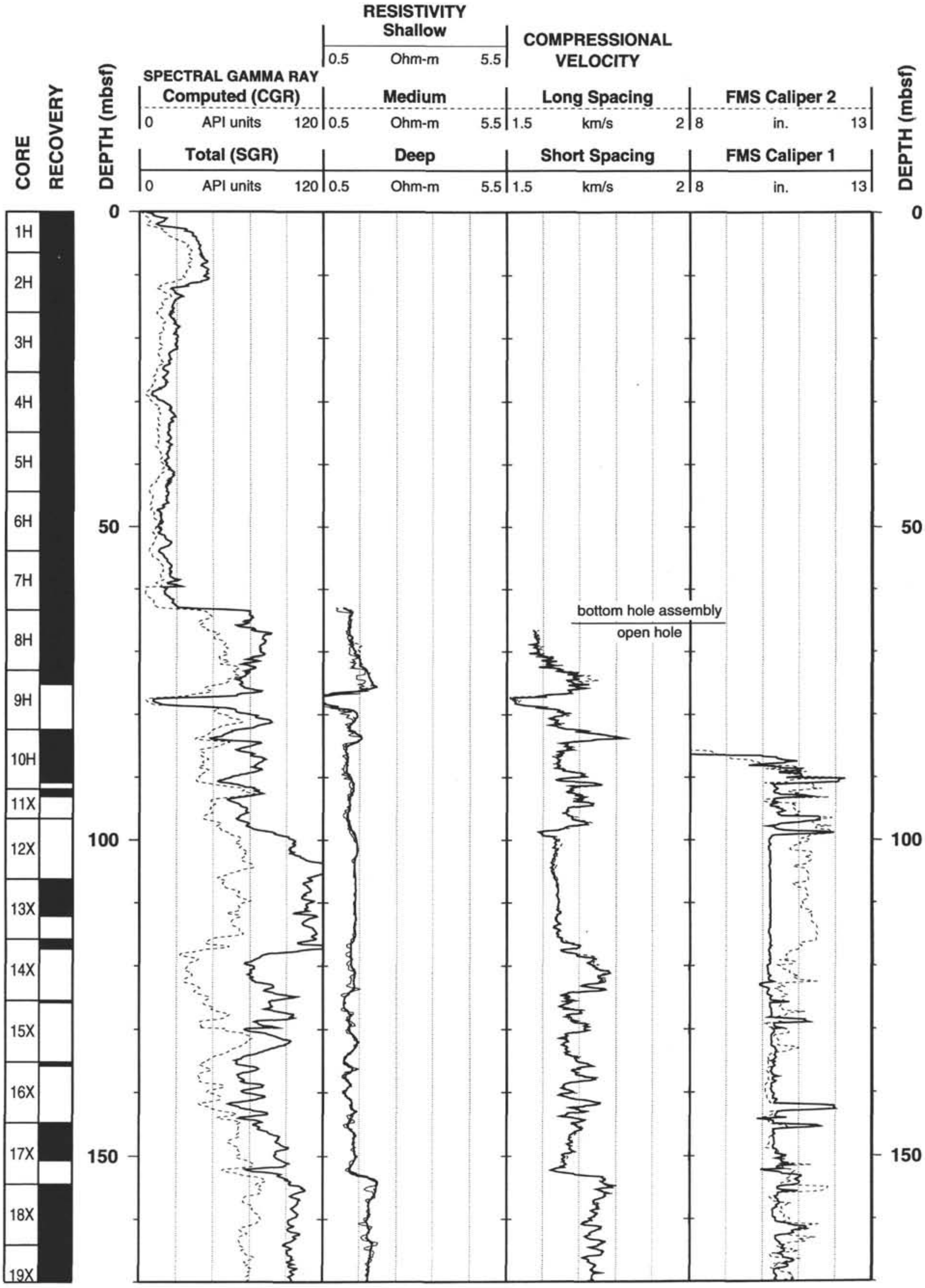

936A Natural Gamma Ray-Resistivity-Velocity Logging Data (cont.)

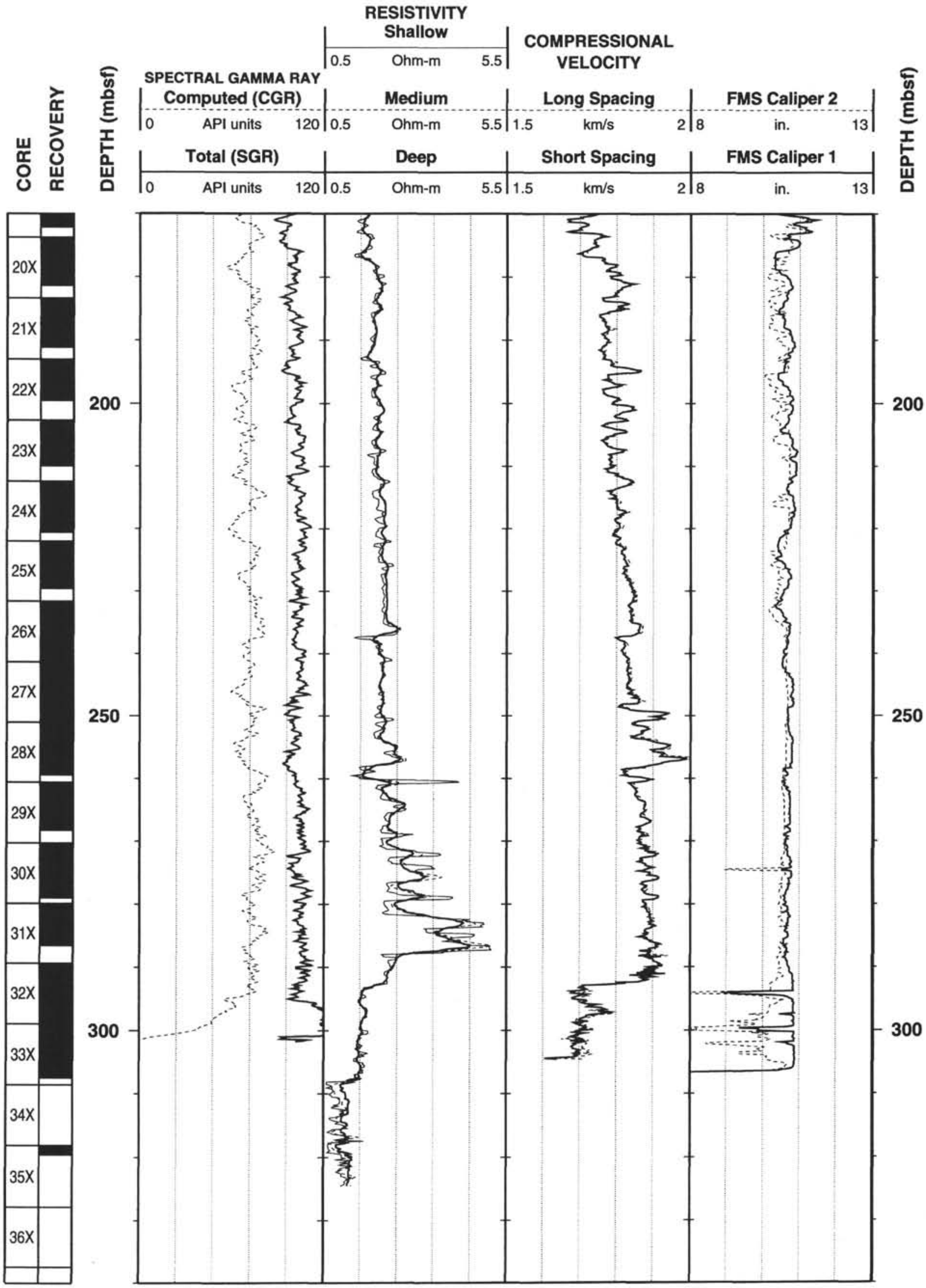

936A Natural Gamma Ray Logging Data

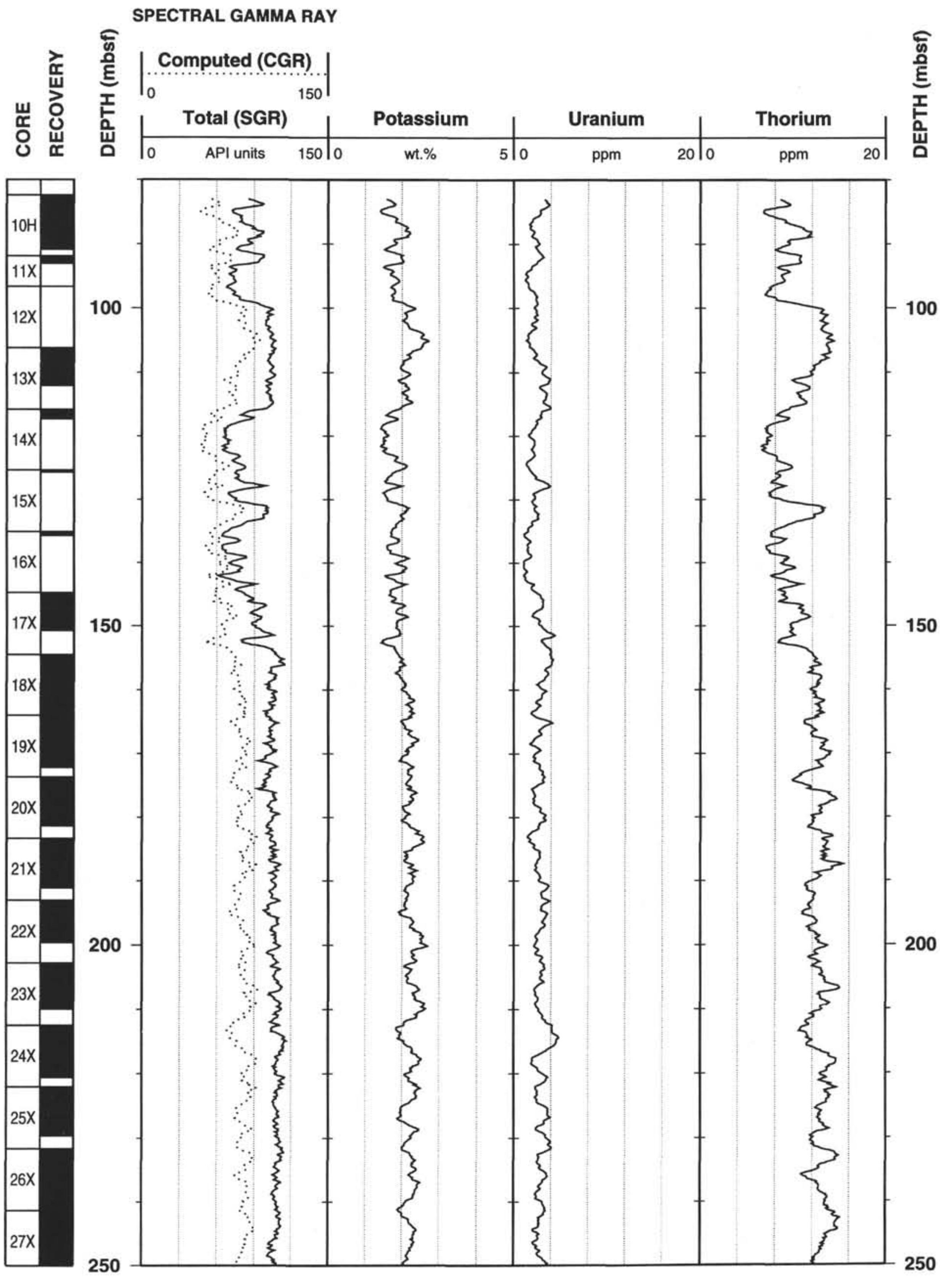

936A Natural Gamma Ray Logging Data (cont.)